Master Thesis, Department of Geosciences

Imaging reservoir quality of Alka discovery, Norwegian Barents Sea

Petrophysical, rock physical and AVO modeling approach

Omer Saeed

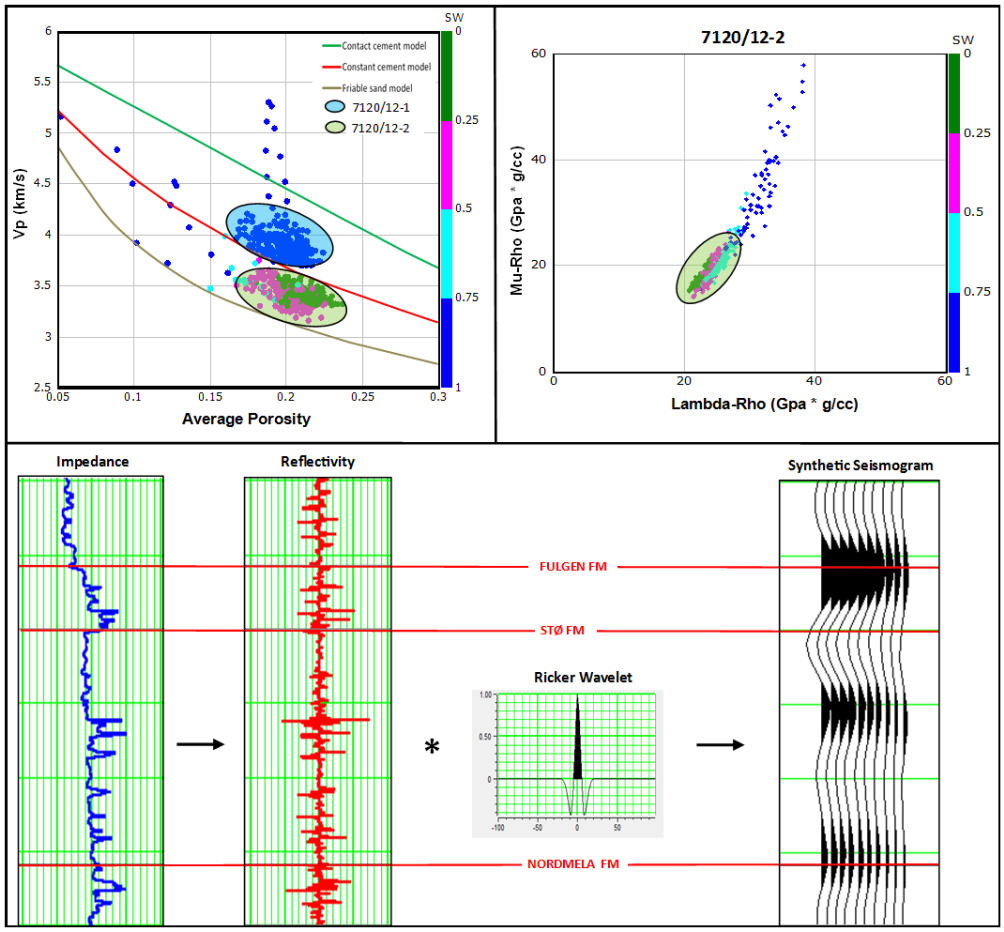

UNIVERSITY OF OSLO
FACULTY OF MATHEMATICS AND NATURAL SCIENCES

Imaging reservoir quality of Alka discovery, Norwegian Barents Sea

Petrophysical, rock physical and AVO modeling approach

Omer Saeed

Master Thesis in Geosciences

Discipline: Petroleum Geology and Petroleum Geophysics

Department of Geosciences

Faculty of Mathematics and Natural Sciences

University of Oslo

30.05.2013

Preface

This thesis is part of the ‘‘BarRock’’ (Barents Sea Rock Properties) project and is submitted to the Department of Geosciences, University of Oslo (UiO), in candidacy of the M.Sc. Degree in Petroleum Geology and Petroleum Geophysics.

This research has been performed at the Department of Geosciences, University of Oslo, during the period of January 2013-May 2013 under the supervision of Nazmul Haque Mondol, Associate Professor, Department of Geosciences, University of Oslo, Oslo, Norway.

Acknowledgements

First and foremost, I would like to thank God, the Almighty, Who gave me the power to believe in myself and pursue my dreams. I could never have done this without the faith I have in Him.

I would like to express my deep gratitude to my supervisor, Nazmul Haque Mondol for his professional guidance, valuable inputs and consistent encouragement throughout the research work. Furthermore, I would also like to extend my thanks to the IT staff especially Michael Heeremans at the Department of Geosciences for his technical support.

I am particularly grateful to the people working in the 'BarRock' project especially Irfan Baig, Mohammad Koochak Zadeh and Sirikarn Narongsirikul for their useful and constructive feedback during my research work.

I would also like to thank my study group mates Shahzeb Haider and Fahad Ashraf for their valuable inputs and discussion during the research work. I would also like to thank Arif Butt, Azeem Hussain and Ahmad Salman for their constructive feedback during the research work. I would also thanks to all the friends with whom I had a great time and learnt a lot during my study at the University of Oslo.

Finally, I wish to thank my parents and family members for their support and encouragement throughout my study at the university.

Omer Saeed

Abstract

The main focus of this study is to image reservoir quality of the 'Alka discovery located in the southern part of the Hammerfest Basin, Norwegian Barents Sea. A total of five exploration wells (7120/12-1, 7120/12-2, 7120/12-3, 7120/12-4 and 7120/12-5) drilled in the study area of which four of them (7120/12-1, 7120/12-2, 7120/12-3, 7120/12-5) are located in the Hammerfest Basin, while the other one (7120/12-4) is located in the Finnmark Platform. The main reservoir unit is the Stø Formation of Middle Jurassic sandstones while U. Jurassic Hekkingen Formation acts as the main source rock for hydrocarbons. Four other potential reservoirs (Nordmela, Tubåen, Fruholmen and Snadd) are also present in the study area of Middle-Upper Triassic to Middle Jurassic age.

An integrated approach is used to investigate the reservoir quality of the five reservoirs of Kapp Toscana Group though the main emphasis is given to the Middle Jurassic Stø Formation; the prime reservoir in the Norwegian Barents Sea. Petrophysical analyses, rock physical diagnostics and AVO modeling are utilized to investigate the reservoir quality using data from the five exploration wells.

The Stø Formation shows good reservoir quality because of high net-to-gross ratio and less amount of shale present in the formation. However, the quality of the reservoir varies with depth and location of the wells. The thin interbedded shales present within the Stø Formation reduce the quality of the reservoir sandstone at certain places. Petrophysical analyses indicate that the existence of gas saturated zones in the Stø Formation are present in the wells 7120/12-2 and 7120/12-3. The reservoir intervals consist of clean, fine to medium grained and well sorted sandstones. Nordmela, Tubåen and Fruholmen Formations have moderate reservoir quality due to a higher amount of shale content and intermediate value of net-to-gross ratio. The Snadd Formation has poor reservoir quality as depicted by low net-to-gross ratio, high percentage of shale and poor sorting.

A series of rock physics diagnostics have been employed to study the porosity, clay content, cementation and fluid saturation of the five reservoir horizons of Kapp Toscana Group. The crossplot of porosity versus Vp shows that the Stø Formation in the wells 7120/12-5 and 7120/12-1 is more cemented as compared to the other two wells 7120/12-2 and 7120/12-3. In the wells 7120/12-2 and 7120/12-3 the gas saturated zones can be identified by low Vp in the porosity versus Vp cross plot. Although the cross plot of AI versus Vp/Vs is an excellent indicator to discriminate fluid types but the gas saturated zones identified earlier fall on the water saturated line in AI versus Vp/Vs cross plot. However, the cross plot of Lamda-Rho and Mu-Rho clearly shows that these gas saturated zones have lower values of Lambda-Rho (incompressibility) and Mu-Rho (rigidity).

AVO modeling indicates that change in rock properties are more pronounced by introducing 10% gas saturation than at higher percentages of gas. The top of the Stø Formation exhibits the Class IV gas sand and the zero offset reflection coefficient increases with increase in gas saturation.

The outcomes of the study is to enhanced understanding of quality of the reservoir rocks by integrating cross disciplinary techniques including petrophysical analyses, rock physics diagnostics and AVO modeling which may not be that developed at the time when the Alka discovery was discovered. As the study area has experienced several phases of uplift and erosion which may have consequence on reservoir quality, maturity of source rock and reservoir pressure, thus compaction study and exhumation estimation are necessary to understand better the associated uncertainties and to reduce the risk for further exploration and development in the study area.

Nomenclature

AI: Acoustic Impedance

AVO: Amplitude Versus Offset

BTH: Bottom Hole Temperature

HI: Hydrogen Index

I_{GR}: Gamma Ray Index

K: Bulk Modulus

MD: Measured Depth

N/G: Net-to-gross ratio

RKB: Relative to Kelly Bushing

RPT: Rock Physics Template

S_w: Water saturation

TOC: Total Organic Content

TVD: Total Vertical Depth

Vp: P-wave velocity

Vs: S-wave velocity

V_{sh}: Volume of shale

$\emptyset_{avg}$: Average porosity

$\lambda\,\rho$: Lambda-Rho

v: Poisson's ratio

μ: Shear modulus

$\mu\rho$: Mu-Rho

ρ: Density

Table of Contents

Chapter 6: AVO Modeling

Chapter 7: Summary and Conclusions

List of Figures

Chapter 1: Introduction

Chapter 2: Geology of the Alka discovery

Chapter 3: Research methodology and theoretical background

Chapter 4: Petrophysical analyses of reservoir rocks

Chapter 5: Rock Physics Diagnostics of reservoir rocks

Chapter 6: AVO Modeling

List of Tables

Chapter 1: Introduction

Chapter 2: Geology of the Alka discovery

Chapter 3: Research methodology and theoretical background

Chapter 4: Petrophysical analysis of reservoir rocks

Chapter 6: AVO Modeling

Chapter 1

Introduction

1.1 General introduction

The Greater Barents Sea is formed due to two main collision events followed by the continental separation (Dore, 1995). The whole Barents Sea Area is subdivided into two major provinces; Eastern and Western Barents Sea separated by north–south trending monoclinal structure (Fig. 1.1). The Eastern Barents Sea contains both South and North Barents Basins and also includes the Uralides, Timan–Pechora and Novaya Zemlya. The Western Barents Sea is tectonically more complex compared to the Eastern Barents Sea and contains mosaic of platforms, basins and structural highs (Worsley, 2008).

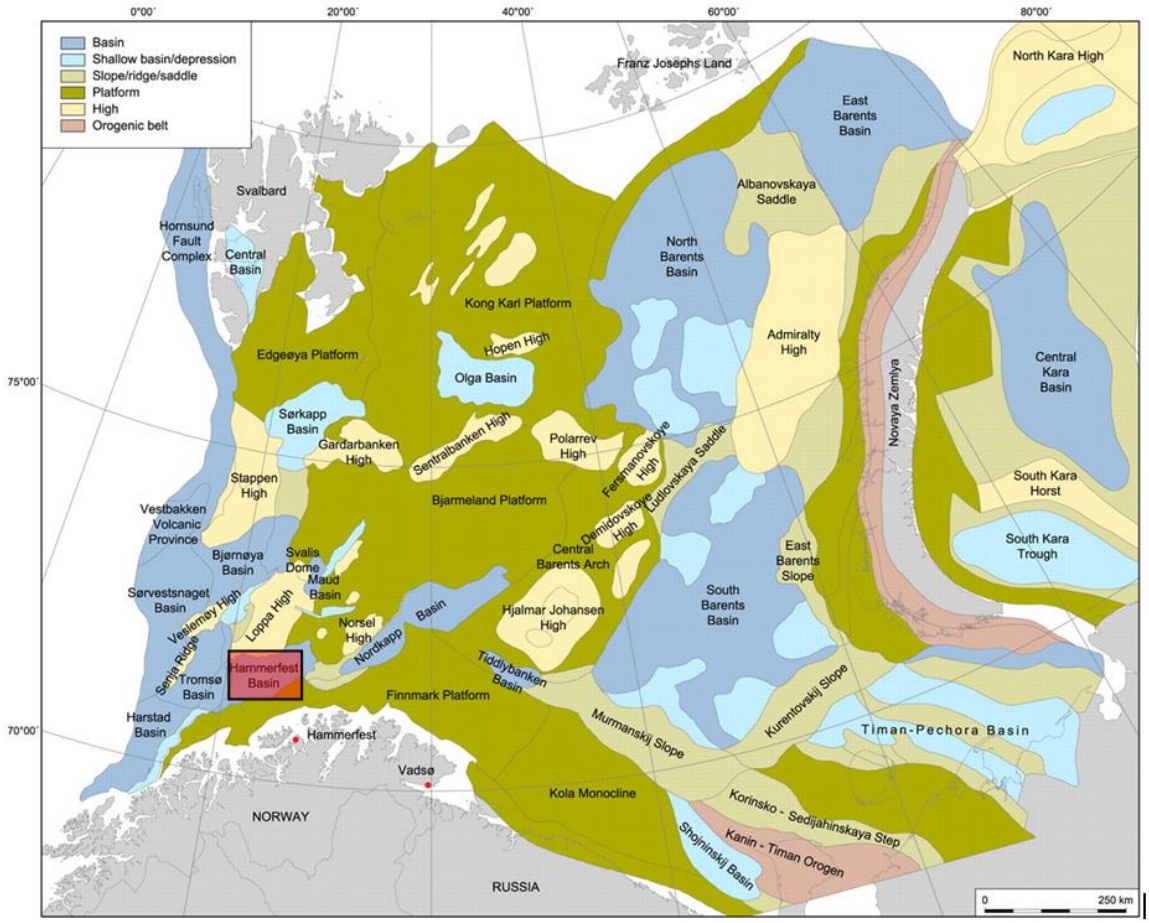

Figure 1.1: Structural elements of the greater Barents Sea. Shaded rectangle shows location of the Hammerfest Basin (Modified after Henriksen et al., 2011).

The study area the 'Alka discovery' is situated in the Hammerfest Basin, SW Barents Sea (Fig. 1.1). The SW Barents Sea formed due to the continental separation resulted in a series of Post-Caledonian rift phases until the Cenozoic (Faleide et al., 2008). Some of the world's deepest sedimentary basins are formed in the SW Barents Sea due to several stages of regional tectonics in the North Atlantic-Arctic regions. Thick sedimentary cover of Cenozoic and Mesozoic rocks has been encountered in most of the wells drilled in the Hammerfest Basin (Faleide et al., 1993).

The Hammerfest Basin is a 150 km long and 70 km wide sedimentary basin. It is an asymmetric and elongated basin striking ENE-WSW bounded in the north by the Loppa High, to the south by the Finnmark platform, to the west by the Trømso Basin and to the east and north-east by the Nordkapp Bsain and Bjarmeland Platform (Fig. 1.1) (Ostanin et al., 2012).

The basin became wide and deep towards west along the Ringvassgly-Loppa Fault Complex. The Hammerfest Basin has maximum subsidence along the northern and southern margins. The central part of the basin is dominated by E-W trending fault system formed by flexural extension related to the doming (Sund et al., 1986).

The Hammerfest Basin is an active area for exploration of hydrocarbon and for scientific research due to its complex geological evolution. The major discoveries in the Hammerfest basin were made in 1980s including Askeladden, Albatross and Snøhvit (Fig. 1.2) (Dore, 1995). Until now, 96 exploration wells have been drilled in the Western Barents Sea where most of the wells are located in the Hammerfest Basin. Most of the reserves are found to be gas with the exception of the Goliat. The lack of oil discoveries are assumed to be a result of several phases of uplift and erosion due to regional tectonics and glaciations and deglaciation caused tilting and leakage of traps and exhumation of reservoirs (Ostanin et al., 2012).

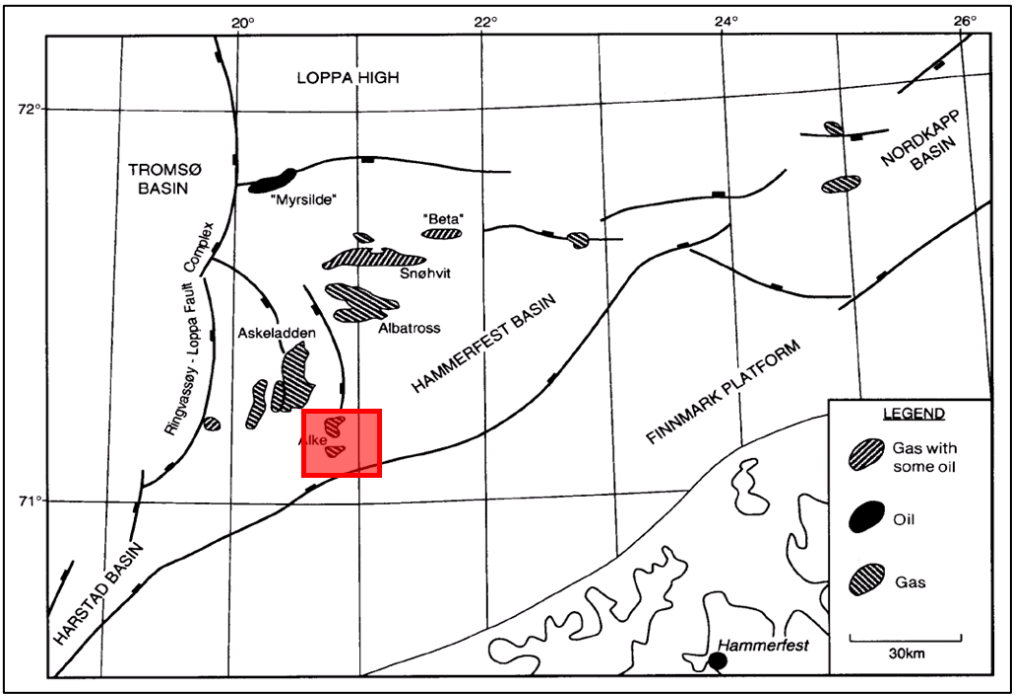

Figure 1.2: Location of major discoveries in the Hammerfest Basin, SW Barents Sea (Modified after Dore, 1995).

1.2 Background and motivation

Hydrocarbon resources are limited and as the consumption of oil and gas is increasing continuously, the need of today is to explore new areas and challenges like arctic and also to enhance the recovery of hydrocarbons from existing fields. New techniques of exploration are being employed and advanced softwares have been introduced to focus challenges of new exploration areas and to improve production from the existing fields. Most of the North Sea has been explored and the oil production has declined sharply nowadays from the existing fields so the focus of hydrocarbon exploration has shifted towards the Barents Sea. The Norwegian Barents Sea has a potential to bear oil that is proved by the two recent discoveries of Skrugard and Havis. The recent oil discoveries also provide a path for future exploration in the SW Barents Sea. The main motivation here is to use the background knowledge of petrophysics, sedimentology, and reservoir geology and to employ the latest techniques of rock physics and AVO modeling for imaging reservoir quality across the different reservoir horizons in and around the Alka Discovery.

1.3 Research Objectives

The main aim of the research is to utilize well log data from five exploration wells drilled in the southern part of the Hammerfest Basin and the Finnmark Platform to image reservoir quality by integrating petrophysical, rock physical and AVO modeling techniques. The research focuses are highlighted below:

- To analyze petrophysical properties such as shale volume, net-to-gross ratio, porosity and saturation of different reservoir horizons.
- To investigate the reservoir rocks of Kapp Toscana group using standard rock physics templates with main emphasis to Stø Formation.
- AVO modeling to investigate the change in reservoir properties response to change in fluid saturation.

1.4 Study area and database

The Alka discovery is located in the southern part of the Hammerfest Basin, SW Barents Sea. In 1981, Gas/condensate was discovered in the well 7120/12-2 in the Stø and Snadd Formation. In 1983, another gas discovery was made in the well 7120/12-3 of hydrocarbon interval occurs in the upper part of the Stø Formation.

The study area contains five exploration wells, of which four of them 7120/12-1, 7120/12-2, 7120/12-3, 7120/12-5 are located in the Hammerfest Basin and the last one 7120/12-4 is located in the Finnmark Platform (Figs. 1.3 and 1.4). The wells 7120/12-2 and 7120/12-3 are the discovery wells while the wells 7120/12-1, 7120/12-4 and 7120/12-5 are dry (Source: NPD).

Figure 1.3: Location of the study area (source: NPD Factmaps).

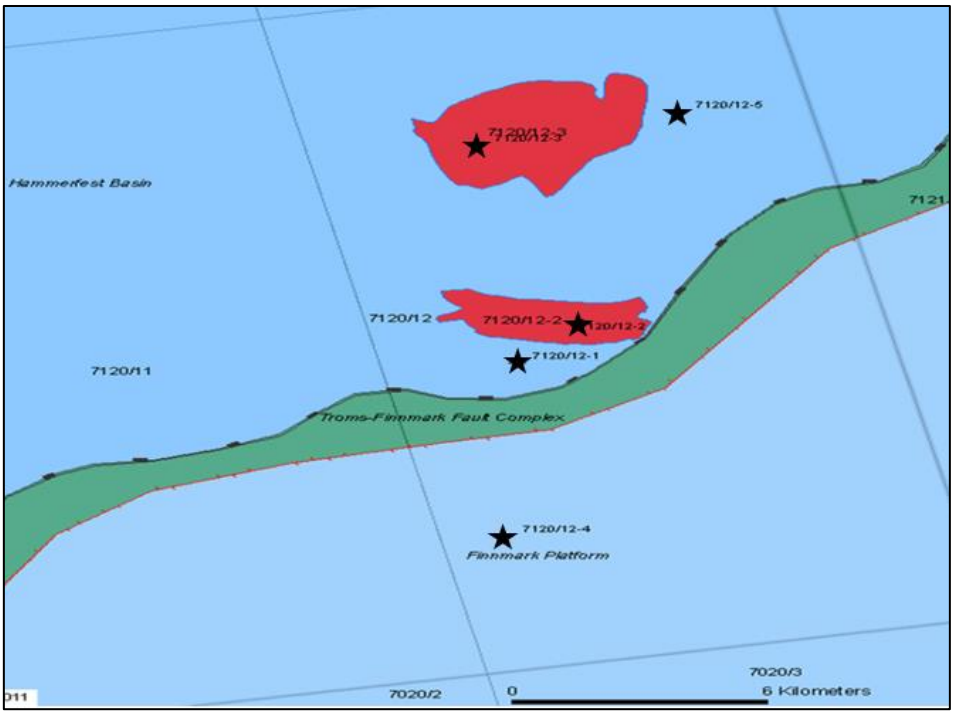

Figure 1.4: The five studied exploration wells in and around the Alka discovery (source: NPD Factmaps).

The four wells 7120/12-1, 7120/12-2, 7120/12-3 and 7120/12-4 were drilled by Norsk Hydro in the early to mid-1980s while the well 7120/12-5 was drilled by Eni Norge in 2010 (Source: NPD). The 7120/12-2 is the deepest well drilled up to 4680 m into the basement rock of Pre-Devonian age. The depth of penetration, type, content, bottom hole temperature and depth of water for the five wells in the study area are illustrated in the Table 1.1.

Table 1.1: Wells penetrated in the study area (source: NPD).

Well Name	Total depth (m) RKB	Types of well	Content	Bottom hole temp. (^{0}C)	Water depth (m)
7120/12-1	3573	Exploration	Dry	65	167
7120/12-2	4680	Exploration	Gas/ Condensate	115	164
7120/12-3	2523	Exploration	Gas	118	185
7120/12-4	2199	Exploration	Dry	51	152
7120/12-5	3630	Exploration	Dry	100	181

1.5 Chapter descriptions

The first chapter (Chapter 1) gives an introduction to the study area and a short description of motivations, research objectives, database and limitations. The chapter 2 elaborates the evolution and structural elements surrounding the Hammerfest basin along with a short description of different stratigraphic units. Discussion on the Petroleum system including source, reservoir and trap/seal rocks are also included in the chapter. The chapter 3 explains the research methodologies and theoretical background of petrophysical analyses, rock physics diagnostics and AVO modeling. The chapter 4 contains results and discusses petrophysical analyses including shale volume calculation, porosity and fluid saturation of different reservoir units. The chapter 5 emphasizes mainly on the rock physics diagnostics of

the reservoir rocks of Triassic and Jurassic reservoirs using standard rock physics templates. The chapter 6 focuses on AVO modeling to investigate the changes in rock properties as a result of saturation change of pore fluids in the reservoir rocks. Finally, in chapter 7 a general summary and conclusions of important findings of the research are shown.

1.6 Limitations and future works

Due to time limitation, the present research is mainly focused on reservoir horizons. Shear wave velocity is a very important parameter in the rock physics and AVO analysis as it is used in various calculations of modulus and cross plot interpretation. Vs is present only in one well 7120/12-5, while empirical relations have been used to determine the Vs for other wells.

The study area lies within the complex structural regime with network of fault complexes surrounding the Hammerfest Basin. So the detailed understanding of major and minor faults is important as the faults influence the properties of source, reservoir and cap rocks.

One can extend this research in many other directions such as by doing same analyses on source and cap rocks. The study area has suffered many phases of uplift and erosion, so compaction study can also be carried out to know exact exhumation. Moreover, marking the transition zone between mechanical and chemical compaction one can better estimate cementation in the reservoir rocks.

Thin section study to enhance understanding of reservoir rocks can also be done for detailed and more precise study to get confirmation of mineral content, porosity and saturation in the reservoir zones. SEM analysis can also be incorporated to study grain coatings, cement volume estimation and their effect on porosity, permeability and elastic properties of reservoir rocks.

Chapter 2

Geology of the Alka discovery

2.1 Tectonic history and geological evolution

The Norwegian Barents Sea is subdivided into three geological provinces (Faleide et al., 1993), considering the style of tectonics, crustal structures and sedimentation separated by major faults zones (Fig. 2.1).

- Oceanic Lofoten Basin and the Vestbakken Volcanic Province in the west
- South-western Barents Sea Basin Province
- Eastern region

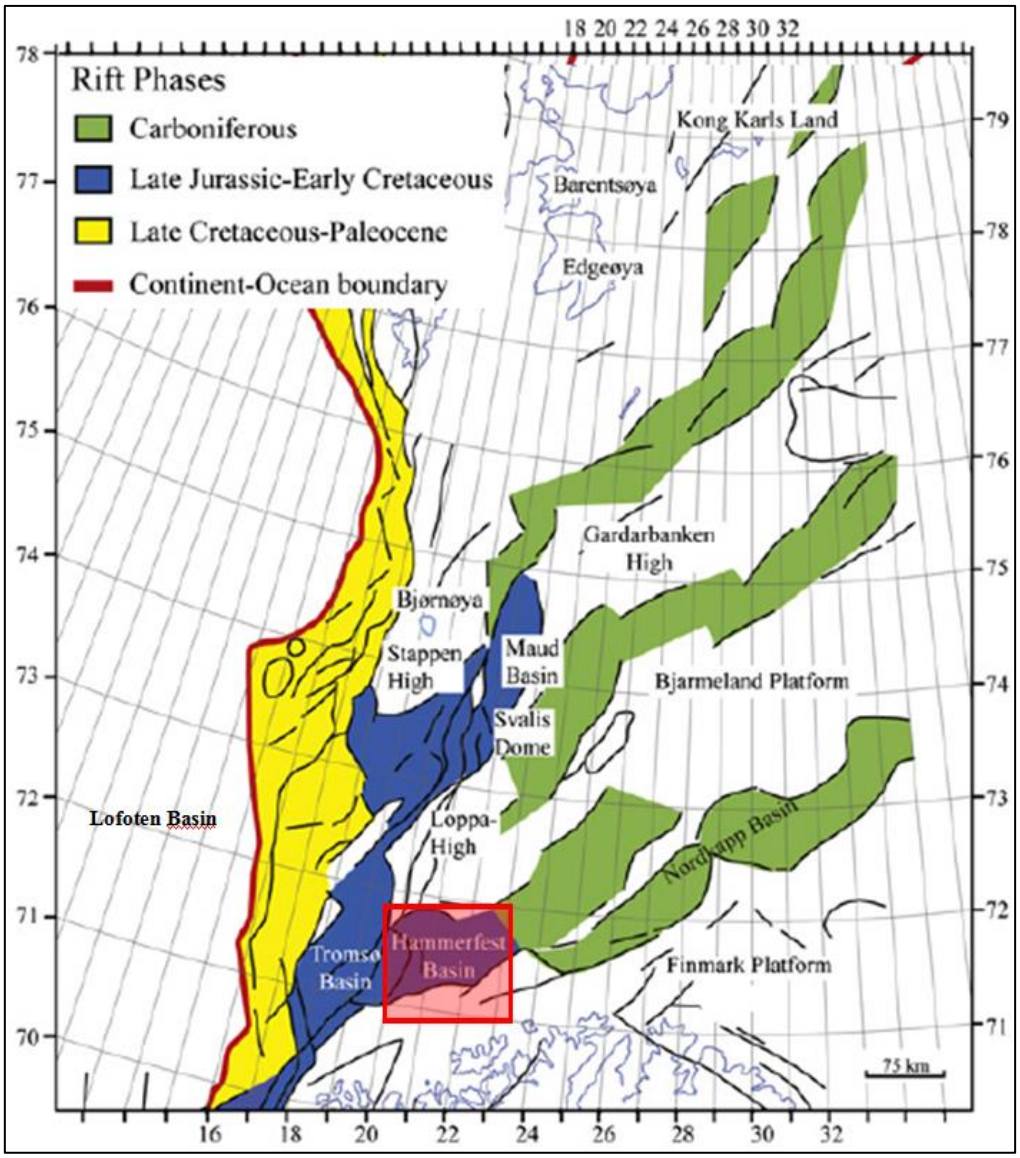

Figure 2.1: Major structural features, platforms and basins in the Norwegian Barents Sea (Modified after Glorstad-Clark et al., 2010).

Since post Caledonian orogeny, the evolution of the region has witnessed three main rifting phases: Late Devonian–Carboniferous, Middle Jurassic–Early Cretaceous and Early Tertiary (Faleide et al., 2010). In the Late Silurian to Early Devonian Caledonian orogeny, consolidated metamorphic basement was formed. In the Late Devonian, the tectonic style

changed from compressional to left lateral strike slip resulted in the formation of large scale strike slip faults (Fig. 2.2). Folding and graben structures were also formed due to transpression and transtension during that time (Faleide et al., 1984). The Middle-Late Jurassic and Early Cretaceous structural developments were dominated by regional extension with strike-slip movement along old structural lineaments forming the rift basins like Bjørnoya, Tromsø and Harstad (Fig. 2.2d) (Faleide et al., 1993). The Late Cretaceous formation was extremely complex with extension was dominating in the west of the Senja Ridge and the Veslemoy High, while at the Tromsø Basin halokinesis and continued thermal subsidence occurred (Faleide et al., 1993). The two stages opening; the Norwegian-Greenland Sea and the development of the sheared western Barents Sea continental margin are the products of Tertiary structuring. The SW Barents Sea basin province formed within the De Geer Zone in the region of rift-shear interaction, in accordance to both the North Atlantic and the Arctic Regions (Faleide et al., 1993).

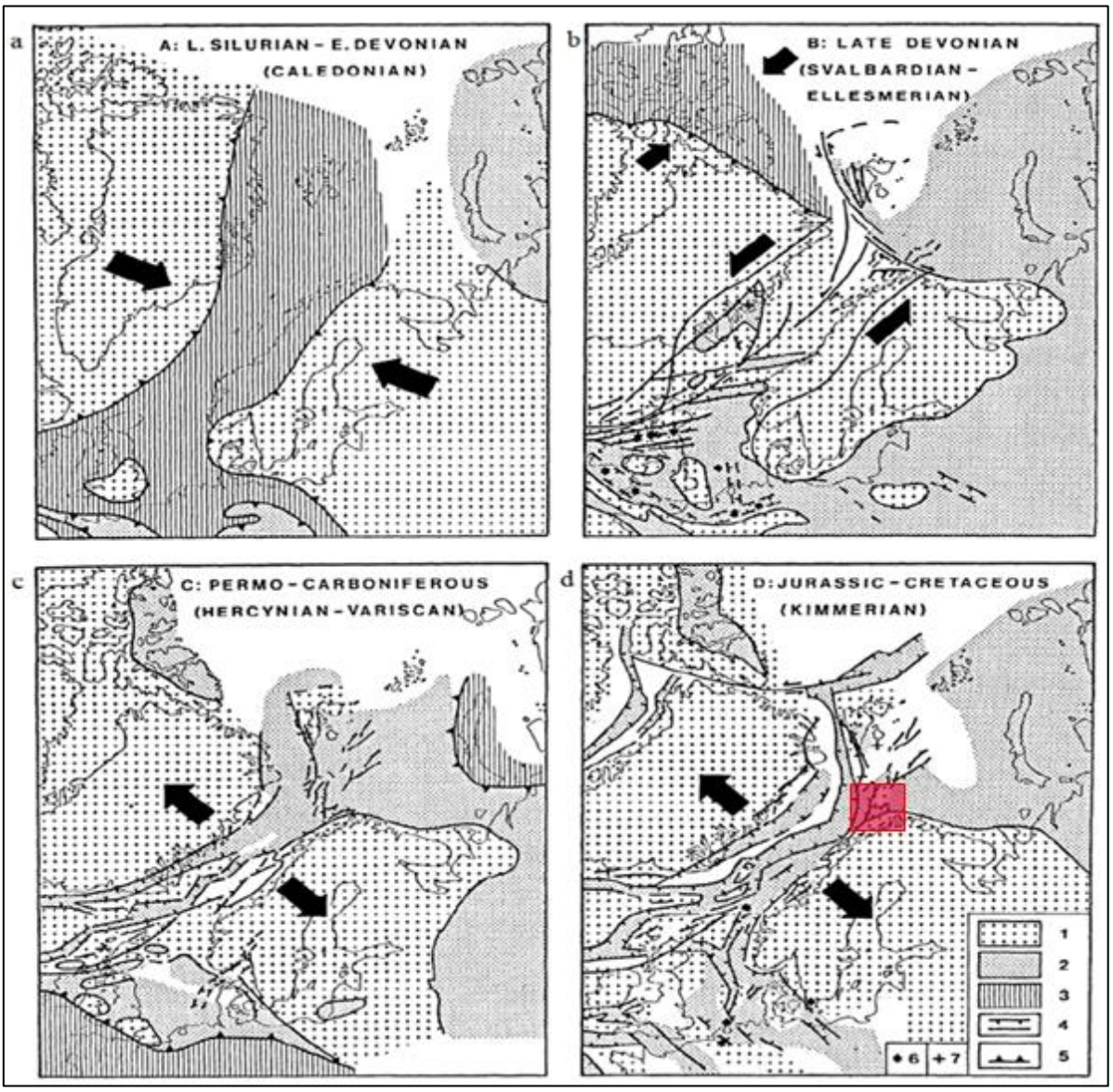

Figure 2.2: Main stages in the evolution of the western Barents Sea and surrounding areas. 1, Stable elements - continental cratons and intrabasinal highs; 2, sedimentary basins; 3, active foldbelts; 4, normal and wrench faults; 5, deformation front of active foldbelts; 6, intrusions; 7, volcanics (Modified after Faleide et al., 1984).

2.2 Structural elements

Ronnevik (1981) separated the SW Barents Sea into three areas; a stable cratonic basin lies east of 25^{o} while transitional area lies west of 20^{o}. Between 20^{o} and 25^{o}E the tectonically complex structures occur including the two major sedimentary basins a) Tromsø and b) Hammerfest. Towards the west, these basins are bordered by Senja Ridge while towards the North by the Loppa High, towards the south the Finnmark Platform separates the basins by the Troms-Finnmark Fault Complex (Fig. 2.3) (Gabrielsen, 1984). A short description of the main structural elements surrounding the study area is given below:

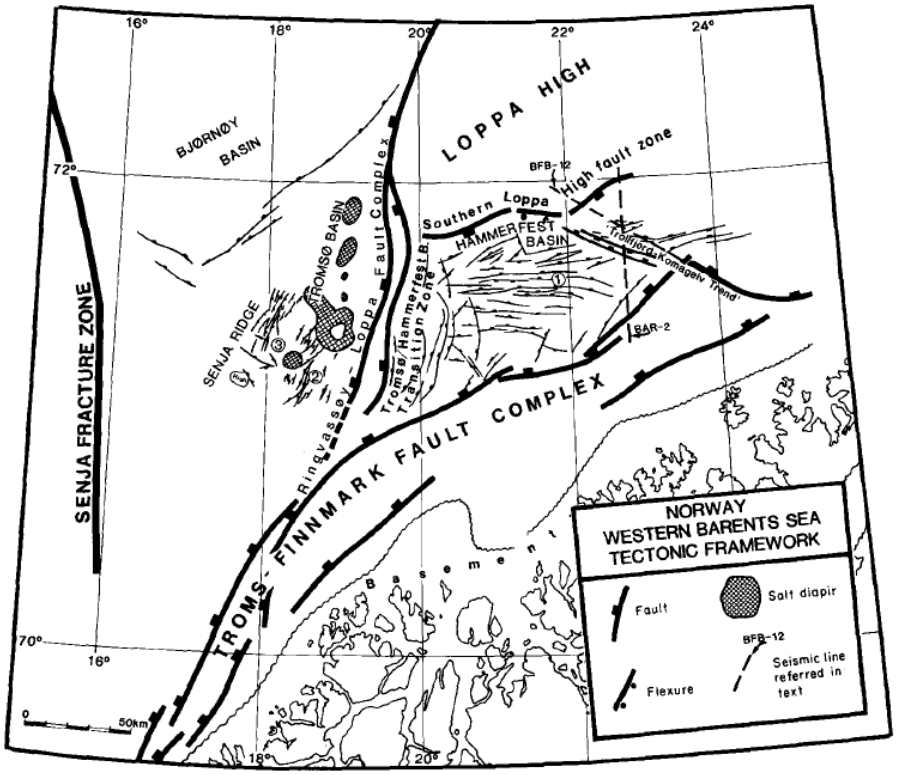

Figure 2.3: Structural elements of SW Barents Sea (Gabrielsen, 1984).

2.2.1 Troms-Finnmark Fault Complex

It runs parallel to the coastline of Tromsø and Finnmark (Fig. 2.3). The fault complex serves as the main structural division between the sedimentary rock deposited on the Troms-Finnmark Platform and the crystalline basement (Gabrielsen, 1984). The fault complex shows a structural trend of NE-SW in the southern part while it changes to more ENE-WSW at 19^{o}E. The major fault system is generally concave on basinward side and collapse structures are also observed with the roll over structure (Gabrielsen, 1984).

2.2.2 Tromsø and Hammerfest Basin Transition Zone

This zone divides the two sedimentary basins of different tectonic settings. It is the part of Ringvassøy-Loppa fault complex and is the extension of the Troms-Finnmark Fault Complex in the southern side (Fig. 2.3). The transition zone is located in the western side; the eastern side of the Tromsø Basin. The faults system typically shows detached normal fault geometry (Fig. 2.4) (Gabrielsen, 1984).

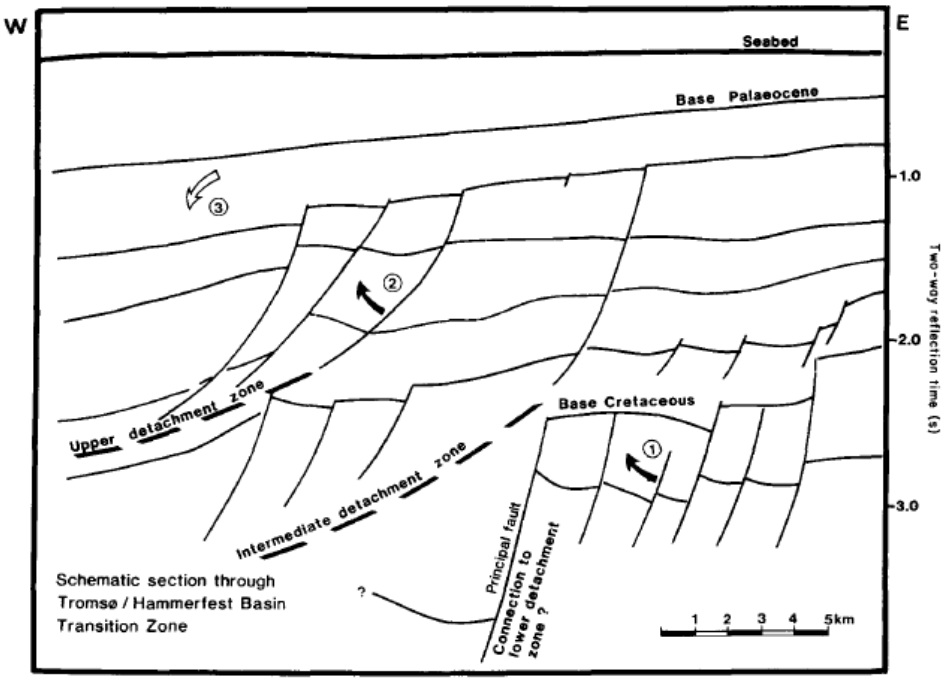

Figure 2.4: Geometry of faults in the Tromsø-Hammerfest Basin Transition Zone. The rotation in three phases of faulting is indicated by arrows (source: Gabrielsen, 1984).

2.2.3 Hammerfest Basin Fault System

The deepest part of the Hammerfest Basin is located in the Northern margin. Troms-Finnmark Fault Complex exaggerates the asymmetry of the basin (Fig. 2.3). The major faults occur in the Jurassic but also other faults exist at deeper level. It is related to the Kimmerian tectonic phase and associated with doming in the Hammerfest Basin (Øvrebø and Talleraas, 1977).

2.3 Stratigraphy

The SW Barents Sea has thick sedimentary sequence from Paleozoic to Quaternary having facies variation both laterally and vertically. The mixed carbonates, evaporites and clastics of Late Paleozoic rocks overlain by clastic sedimentary rocks of Mesozoic and Cenozoic (Fig. 2.5) (Faleide et al., 2010).

The Triassic strata composed of coarsening upward sequences related to transgressive-regressive depositional cycle's occurred throughout the Barents Sea (Mork et al., 1989). The Lower-Middle Jurassic interval is mainly composed of sandstones found throughout the Hammerfest Basin (Faleide et al., 1993).

The Late-Middle Jurassic sequence marks the beginning of rifting in the SW Barents Sea, whereas unconformity within the Upper Jurassic sequence reflects the change in sea-level. The Late Jurassic interval is dominated by shales and claystones with thin interbeds of dolomitic limestone. Siltstones or sandstones occur in minor amount depicting fairly deep and quiet marine environments (Faleide et al., 2010). The Lower Cretaceous interval composed dominantly of shales and claystones with thin interbeds of siltstone, limestone and dolomite. This strata is deposited in the marine environment and make up the main basin fill in the SW Barents Sea (Faleide et al., 2010).

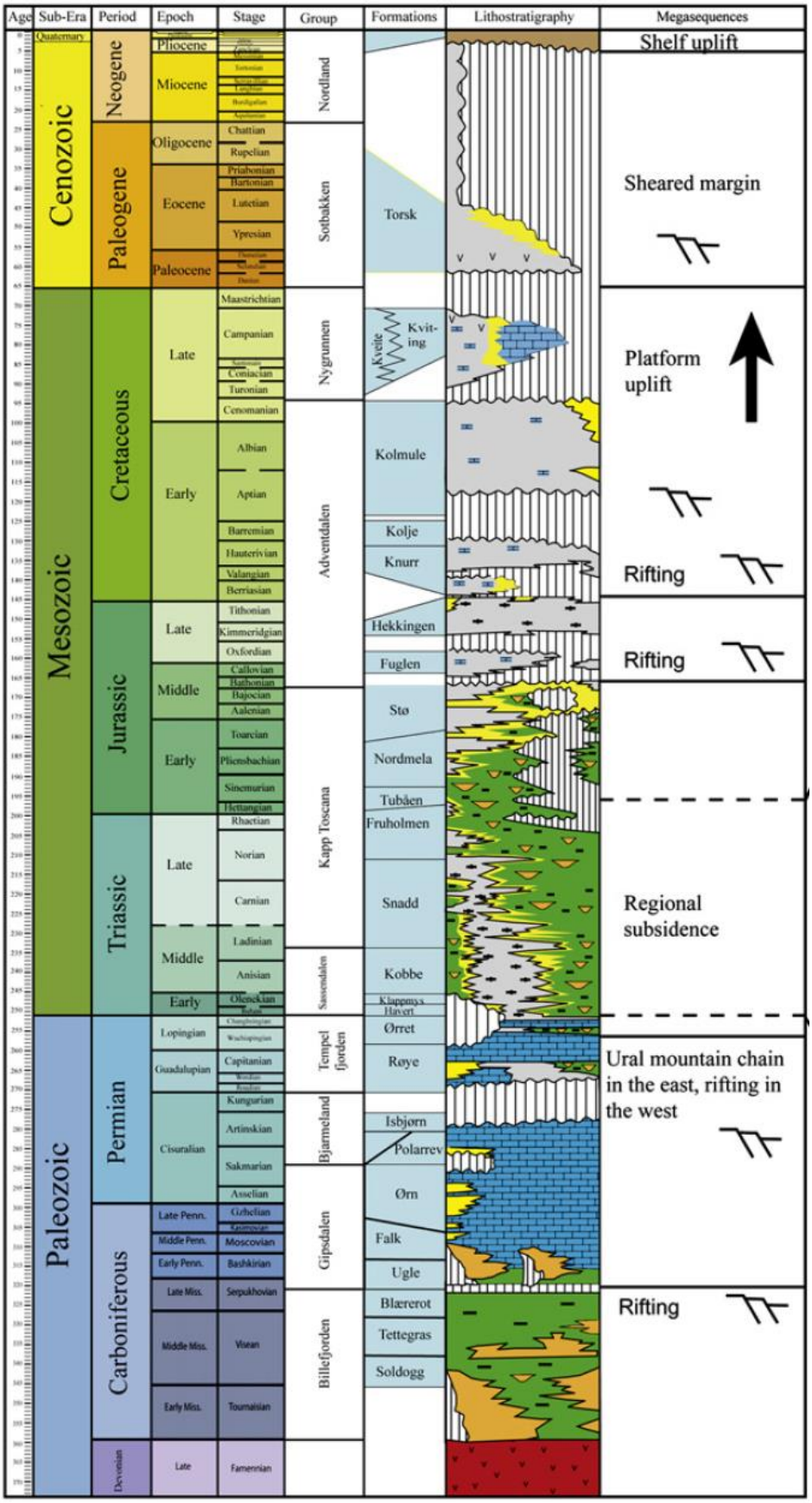

Figure 2.5: A generalized stratigraphic succession of the western Barents Sea (Modified from Glørstad-Clark et al., 2010).

The Paleogene succession unconformably overlies the Cretaceous rocks marking a depositional break at the Cretaceous-Tertiary boundary which occurs throughout the SW Barents Sea (Faleide et al., 2010). The Paleogene interval is dominantly composed of claystones with thin interbeds of siltstones, tuffs and carbonates deposited in an open to deep shelf marine environments (Faleide et al., 1993). The Neogene and Quanternary succession unconformably overlies the Paleogene and Mesozoic rocks. The glacier sediments are of Late Pliocene to Pliestocene/Holocene age having thickness of 100-200 m thick in the Hammerfest Basin which increases to 700 m in the Senja ridge and become more than 4000 m in the Lofoten Basin (Faleide et al., 1993).

The four studied wells drilled in the Hammerfest Basin have thick succession of Jurassic and Cretaceous sediments which were missing in the well drilled in the Finnmark Platform. The well tops for the groups and formations encountered in the wells are given in the Table 2.1. The deepest well 7120/12-2 in the area was drilled up to 4680 m in the basement of Pre-Devonian age.

Table 2.1: The depth of formation tops of different stratigraphic units (e.g. Groups and Formations) penetrated in the five studied wells (Source: NPD).

<table>
<tr><th rowspan="2">Age</th><th rowspan="2">Groups/ Formations</th><th colspan="4">Hammerfest Basin</th><th>Finnmark Platform</th></tr>
<tr><th>7120/12-1</th><th>7120/12-2</th><th>7120/12-3</th><th>7120/12-5</th><th>7120/12-4</th></tr>
<tr><td rowspan="2">Cenozoic</td><td>Nordland Gp</td><td>192</td><td>189</td><td>208</td><td>210</td><td>175</td></tr>
<tr><td>Sotbakken Gp</td><td>462</td><td>463</td><td>387</td><td>Missing</td><td rowspan="11">Missing</td></tr>
<tr><td rowspan="5">Cretaceous</td><td>Nygrunnen GP</td><td>725</td><td>701</td><td>738</td><td>766</td></tr>
<tr><td>Adventdalen Gp</td><td>742</td><td>745</td><td>864</td><td>826</td></tr>
<tr><td>Kolmule Fm</td><td>742</td><td>745</td><td>864</td><td>826</td></tr>
<tr><td>Kolje Fm</td><td>1272</td><td>1309</td><td>1422</td><td>1399</td></tr>
<tr><td>Knurr Fm</td><td>375</td><td>1455</td><td>1778</td><td>1828</td></tr>
<tr><td rowspan="6">Jurassic</td><td>Hekkingen Fm</td><td>1660</td><td>1700</td><td>1946</td><td>1963</td></tr>
<tr><td>Fulgen Fm</td><td>2019</td><td>1875</td><td>2142</td><td>2153</td></tr>
<tr><td>Kapp Toscana Gp</td><td>2047</td><td>1892</td><td>2158</td><td>2165</td></tr>
<tr><td>Stø Fm</td><td>2047</td><td>1892</td><td>2158</td><td>2165</td></tr>
<tr><td>Nordmela Fm</td><td>2152</td><td>1978</td><td>2220</td><td>2230</td></tr>
<tr><td>Tubaen Fm</td><td>2250</td><td>2150</td><td>2342</td><td>2365</td></tr>
<tr><td rowspan="7">Triassic</td><td>Fruholmen Fm</td><td>2337</td><td>2234</td><td>2395</td><td>2407</td></tr>
<tr><td>Snadd Fm</td><td>2535</td><td>2354</td><td rowspan="8">Not Penetrated</td><td>2582</td><td>435</td></tr>
<tr><td>Sassendalen Gp</td><td>3474</td><td>2927</td><td>3572</td><td>485</td></tr>
<tr><td>Kobbe Fm</td><td>3474</td><td>2927</td><td>3572</td><td>485</td></tr>
<tr><td>Klappmyss Fm</td><td rowspan="6">Not Penetrated</td><td>3095</td><td rowspan="6">Not Penetrated</td><td>685</td></tr>
<tr><td>Havert Fm</td><td>3552</td><td>992</td></tr>
<tr><td>Permian</td><td>Tempelfjorden Gp</td><td>3657</td><td>1366</td></tr>
<tr><td rowspan="2">Carboniferous</td><td>Gipsdalen Gp</td><td>4558</td><td>2118</td></tr>
<tr><td>Ugle Fm</td><td>4558</td><td>2118</td></tr>
<tr><td>Devonian</td><td>Basement</td><td>4664</td><td>Not penetrated</td></tr>
</table>

A brief stratigraphic description of different groups and formations encountered in the study area are given below:

2.3.1 Gipsdalen Group

- **Ugle Formation**

Ugle Formation is dominantly composed of sandstone and conglomerate with minor siltstone deposited in arid to semi-arid terrestrial environment. The age of the formation is late Serpukhovian to early Bashkirian (Larssen et al., 2002).

2.3.2 Tempelfjorden Group

- **Røye Formation**

Røye Formation is composed of limestone, mudstone, marl and claystone. The formation was deposited in deep shelf environment in the lower part which changes to moderate to deep shelf in the middle and upper parts. The age of the formation is Kungurian to Kazanian (Larssen et al., 2002).

- **Ørret Formation**

Ørret Formation is composed of sandstone, siltstone and shales with sandstone dominates the upper part of the formation. The formation was deposited in deltaic to coastal plain environment in the Hammerfest Basin which changes to deep shelf in the Finnmark Platform. The age of the formation is Kungurian to Tatarian (Larssen et al., 2002).

2.3.3 Sassendalen Group

- **Havert Formation**

Havert Formation is composed of shales with minor interbedd siltstone and sandstones deposited in marginal to open marine environment. The age of the formation is Griesbachian to Dienerian (Dalland et al., 1988).

- **Klappmyss Formation**

Klappmyss Formation is composed of shales which become interbedded with sandstone and siltstone in the upper part. The formation was deposited in marginal to open marine environment. The age of the formation is Smithian to Spathian (Dalland et al., 1988).

- **Kobbe Formation**

Kobbe Formation is composed of 20 m thick sequence of shales at the base marking the transgressive surface which become interbedded with shale, siltstone and cemented sandstone deposited in marginal marine environment. The age of the formation is Anisian (Dalland et al., 1988).

2.3.4 Kapp Toscana Group

The group is subdivided into lower Storfjorden subgroup and upper Realgrunnen subgroup.

Storfjorden subgroup

- **Snadd Formation**

Snadd Formation is composed of shales with interbedding of sandstone and siltstones. In the lower and middle part, limestone and calcareous interbeds are also present. The lower sequence was deposited in distal marine environment while the upper sequence represents progradation of deltaic environment. The age of the formation is Ladinian to early Norian (Dalland et al., 1988).

Realgrunnen Subgroup

The Realgrunnen subgroup includes succession of four formations (Stø, Nordmela, Tubåen and Fruholmen) of Late Triassic–Middle Jurassic age which are the main reservoirs in the western Barents Sea of the Norwegian sector (Henriksen et al., 2011).

- **Fruholmen Formation**

Fruholmen Formation is composed of shales at the base which gradually become interbedded into sandstones, shales and coals. The age of the formation is early Norian to Rhaetian (Dalland et al., 1988).

- **Tubaen Formation**

Tubaen Formation is dominantly composed of sandstones with minor shales and coals. The sand is deposited in marginal marine environment while shales and coals are deposited in lagoonal environment. The age of the formation is late Rhaetian to early Hettangian (Dalland et al., 1988).

- **Nordmela Formation**

Nordmela Formation is composed of interbedded siltstones, sandstones, shales and claystones deposited in tidal flat to flood plain environment. The sandstone dominates the upper part of the formation. The age of the formation is Sinemurian to late Pliensbachian (Dalland et al., 1988).

- **Stø Formation**

Stø Formation is dominantly composed of moderately to well-sorted sandstone deposited in prograding coastal environment with thin beds of shale and siltstone occur in the upper part of the formation. The thickness of the formation is greater in the southwestern part which thin towards east. The age of the formation is Late Pliensbachian to Bajocian (Dalland et al., 1988).

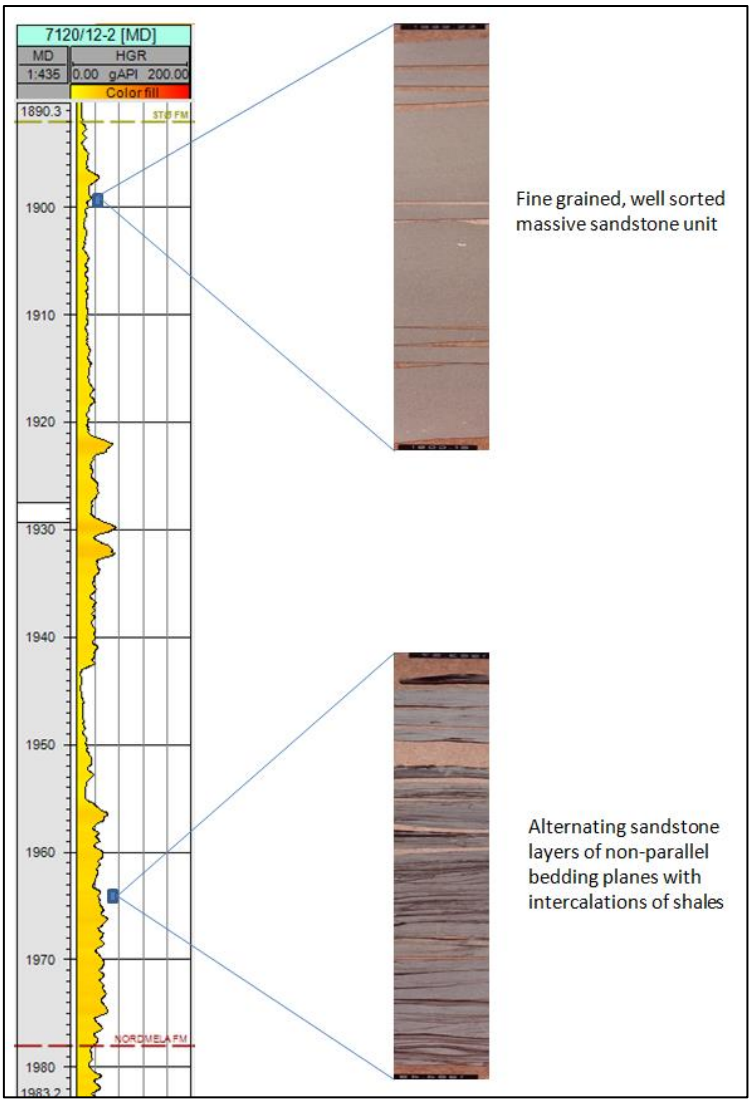

Figure 2.6: Gamma ray log response from the well 7120/12-2 displaying Stø formation with core photos representing two distinctive sandstone units (Source: NPD).

2.3.5 Adventdalen Group

- **Fuglen Formation**

Fuglen Formation is composed of pyritic mudstone with thin interbeds of limestones. The southwestern side is thickest which thins to 10 m in the central highs of the Hammerfest Basin. The age of the formation is Late Callovian to Oxfordian (Dalland et al., 1988).

- **Hekkingen Formation**

Hekkingen Formation is composed of shale and claystone with thin interbeds of limestone, dolomite, siltstone and sandstone. The formation was deposited in deep marine environment. The formation thins toward north to less than 100 m to the axis of Hammerfest Basin. The age of the formation is early Kimmeridgian to Ryazanian (Dalland et al., 1988).

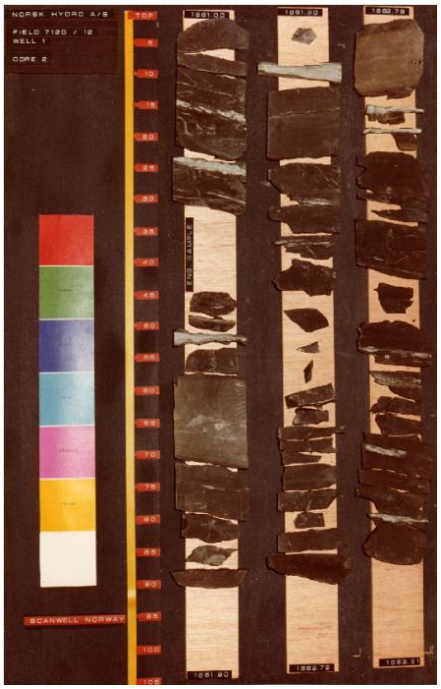

Figure 2.7: Hekkingen Formation core photo showing dark organic shales from the well 7120/12-1 (Source: NPD).

- **Knurr Formation**

Knurr Formation is composed of claystone with thin interbeds of dolomite and limestone. The sand content is higher towards the Troms-Finnmark Fault Complex. The formation was deposited in open marine environment. The age of the formation is Valanginian to early Barremian age (Dalland et al., 1988).

- **Kolje Formation**

Kolje Formation is dominantly composed of shale and claystone with few interbeds of limestone and dolomite. Thin interbeds of siltstone and sandstone are also present in the upper part. The formation was deposited in open marine environment. The age of the formation is early Barremian to early Aptian (Dalland et al., 1988).

- **Kolmule Formation**

Kolmule Formation is composed of claystone and shale with few interbeds of siltstone. Stringers of limestone and dolomite are also present. The formation was deposited in open marine environment. The age of the formation is Aptian to mid-Cenomanian (Dalland et al., 1988).

2.3.6 Nygrunnen Group

The group comprises of two formations, Kveite Formation composed of claystone deposited in deep to shallow shelf environment, while Kviting Formation composed of condensed sequences deposited in open deep shelf environment. The age of the Kveite Formation is Late Cenomanian to early Maastrichtian while of Kviting Formation is Campanian (Dalland et al., 1988).

2.3.7 Sotbakken Group

The group subdivide into only one formation (Torsk Formation) which is 263 m thick in the reference well 7120/12-1. The formation is dominantly composed of claystones with minor stringers of siltstone and limestone that occurs in the whole section. The formation was deposited in an open to deep marine shelf. The age of the formation is Late Paleocene to Oligocene (Dalland et al., 1988).

2.3.8 Nordland Group

It is composed of sand and clay which grade into sandstones and claystones with sand content increasing upward. The origin is glacial and post glacial. The thickness of the group varies from less than 100 to 250 m in the Hammerfest Basin. The age of the formation is Late Pliocene to Holocene (Dalland et al., 1988).

2.4 Petroleum System

The Petroleum system describes the relation between a pod of mature source rock and the accumulation of oil and gas. The essential elements of petroleum system are the source rock, reservoir rock, cap rock and formation of trap. The processes that form the trap are the generation-migration and accumulation of petroleum (Magoon et al., 1994). The greater Barents Sea contains three main petroleum systems including Palaeozoic, Early-Middle Triassic and Late Jurassic. The study area belongs to the mixed system (Fig. 2.8) (Henriksen et al., 2011).

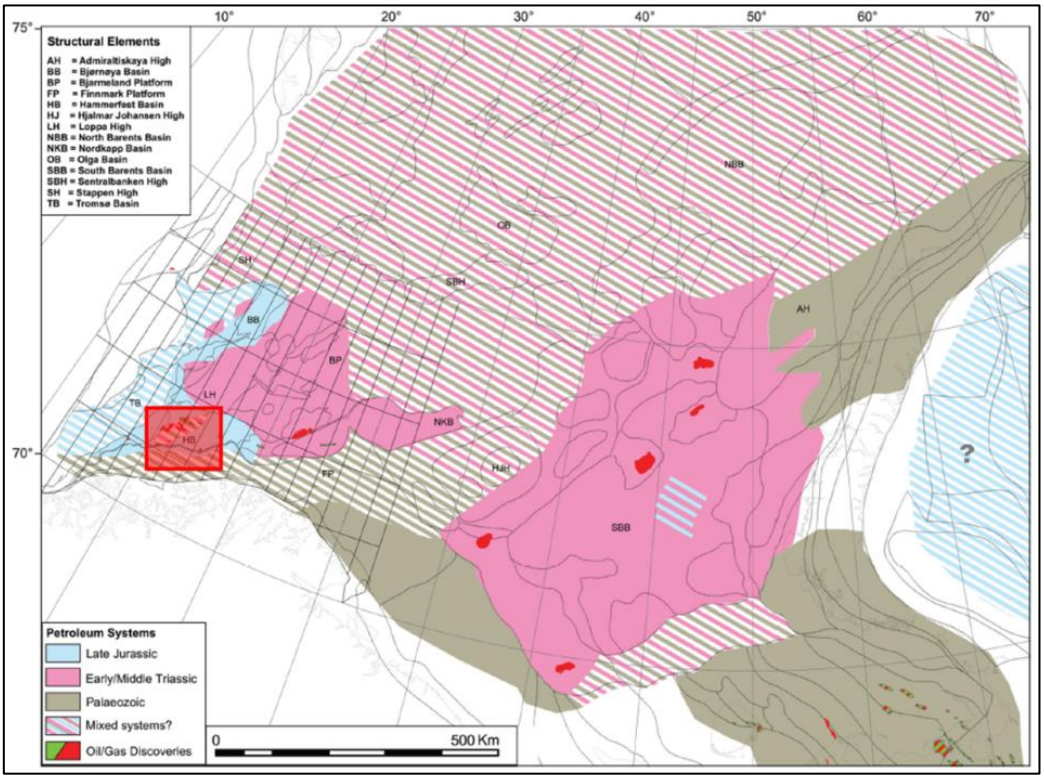

Figure 2.8: Petroleum systems of the greater Barents Sea. Shaded rectangle shows location of the Hammerfest Basin (modified after Henriksen et al., 2011).

2.4.1 Source rocks

Silurian to Cretaceous source rocks has been proven in the SW Barents area. Further westward, the source rocks of Late Permian, Triassic, Late Jurassic and Early Cretaceous are also present (Fig. 2.9) (Henriksen et al., 2011).

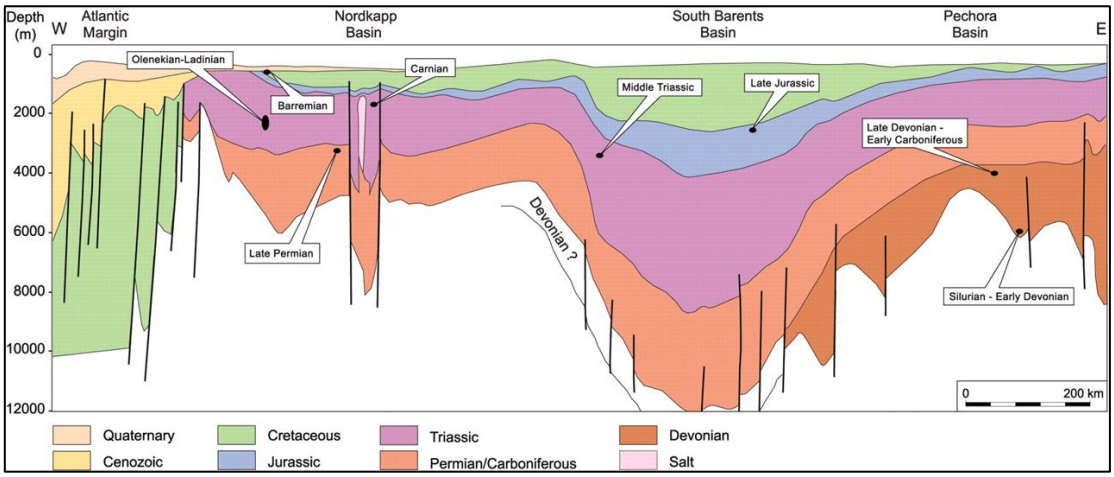

Figure 2.9: Regional geo-seismic profile showing the stratigraphic occurrence of major source rocks in the Barents Sea (Henriksen et al., 2011).

In the study area, three possible source rocks are the Hekkingen Formation of Upper Jurassic, Nordmela Formation of Lower Jurassic and Triassic shales have been identified (Stewart et al., 1995).

The Upper Jurassic Hekkingen Formation is the main source rock for the hydrocarbon discoveries in the Hammerfest Basin (Seidal, 2005). Hekkingen Formation has excellent quality and well distributed source rock. It consists of dark organic shales (Dore, 1995) and is the most potential source rock because of high TOC (0.8-27.9%) and hydrogen index (288-303 mg HC/g TOC). The formation contains mixed organic sources of Kerogen II and III (Table 2.2) (Ohm et al., 2008). The Hekkingen Formation is matured for oil to the western part of the Hammerfest Basin. Nordmela Formation and Triassic rocks are humic and gas-prone (Stewart et al., 1995).

Table 2.2: Petroleum source rocks in the greater Barents Sea (Henriksen et al., 2011)

Age	Formations	Common thickness (m)	Kerogen type	TOC (%)	Hydrogen index, HI (mg g^{-1} TOC)
Barremian	Kolje	<30	II–II/III	1-7	130
Kimmeridgian	Hekkingen	10-250	II/III	<20	300
Early Ryazanian	Bashenov	100-300	II	1->10	<600
Carnian–Norian	Snadd		III–I	<5	300-500
Ladinian	Snadd	1-15	II	6	200-590
Anisian	Kobbe	5-20	II–II/III	2-8	180-350
Olenekian	Klappmyss	<100	III/II	3.5	200-330
Late Permian	Ørret	80-350	II/III	<3.5	Low
Visean	Blærero		III	2-4	500-700
Devonian	Domanic	20-60	II	8-10	300-450

- **Stratigraphic correlation of source rocks**

In the Alka discovery, the main source rocks are Hekkingen and Fulgen Formations of Upper Jurassic age encountered in all the wells drilled in the Hammerfest Basin (Fig 2.10) but absent in the well encountered in the Finnmark Platform.

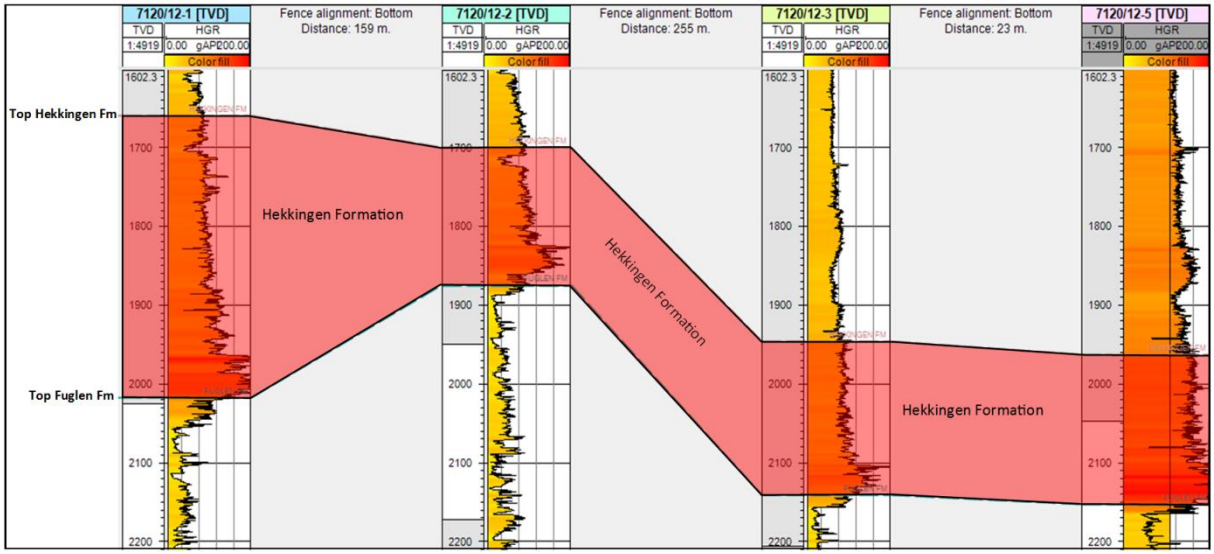

Figure 2.10: Stratigraphic correlation of the source rock unit guided by the gamma ray log response.

2.6.2 Reservoir rocks

The potential reservoir rocks in the study area are Jurassic sandstones while other potential sandstones reservoirs are of Triassic and Cretaceous age (Faleide et al., 2010). The principal reservoir rocks in the study area lie in the Stø Formation of Lower to Middle Jurassic sandstones show good porosity and permeability (Dore, 1995). According to Larsen et al. (1993), 85% of the resources occur in the Stø Formation of the Barents Sea (Fig. 2.11). Stø Formation is predominantly composed of medium to fine-grained sandstones with interbedded shales. The sandstone is clean displaying cross-bedding having marine and trace fossils representing a high-energy shallow-marine environment (Stewart et al, 1995). Stø Formation have net-to-gross ratios of above 0.8, porosity between 18-20% while permeability between 200-800 mD (Selnes et al., 2004).

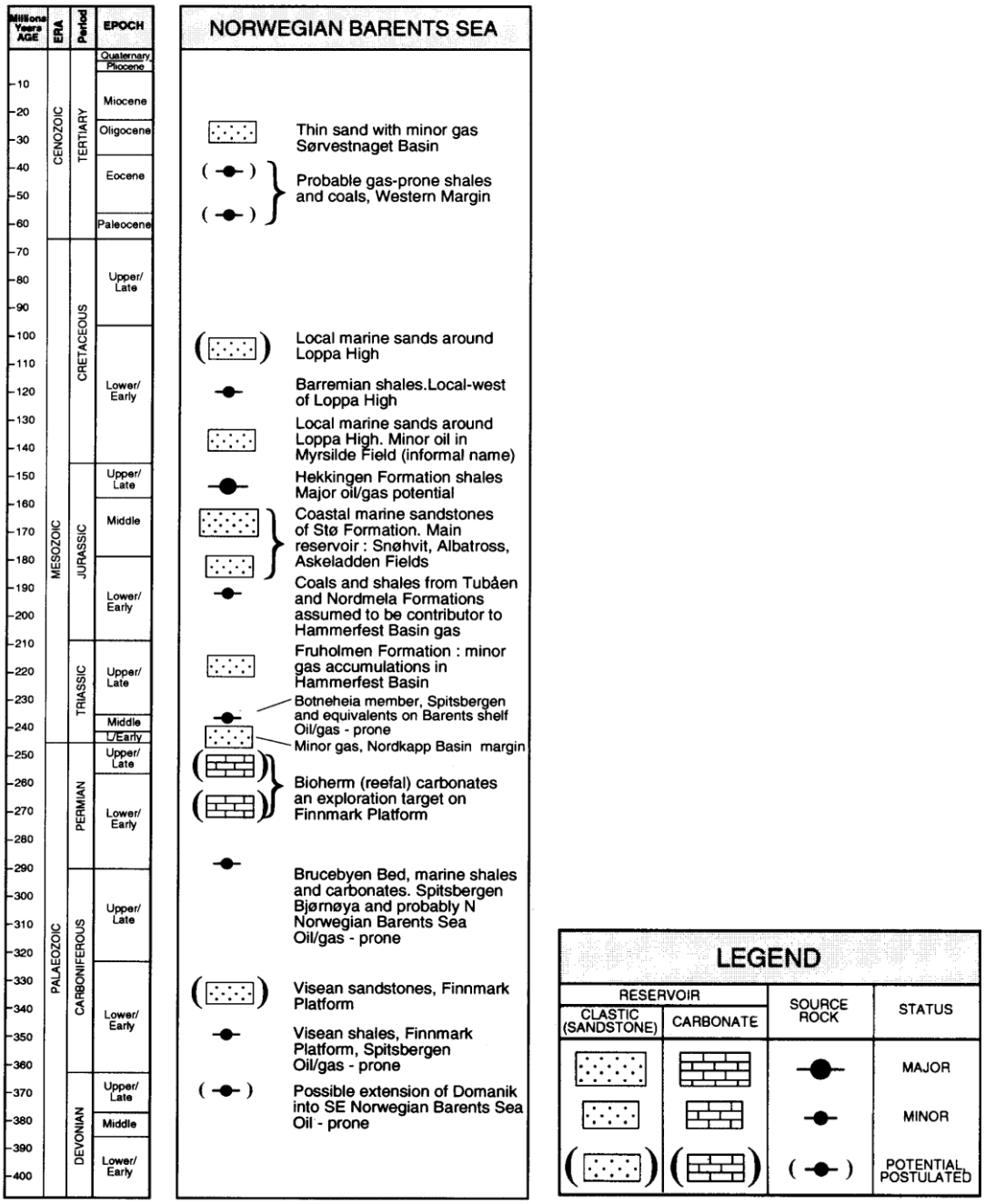

Figure 2.11: Potential reservoir and source rocks in the Barents Sea (Modified after Dore, 1995).

- **Stratigraphic correlation of reservoir units**

In the well 7120/12-2, the reservoir units occur at two stratigraphic intervals of Middle Jurassic Sandstone of Stø Formations and Middle-Upper Triassic sandstones of Snadd Formation. In the well 7120/12-3, the hydrocarbon interval occurs in the Middle Jurassic sandstones (the upper part of the Stø Formation) (Source: NPD). In the study area, Stø formation has maximum thickness of 105 m in the well 7120/12-1 which reduces to 62 m in the well 7120/12-3 (Fig.2.12). The Stø Formation is absent in the well drilled in the Finnmark platform.

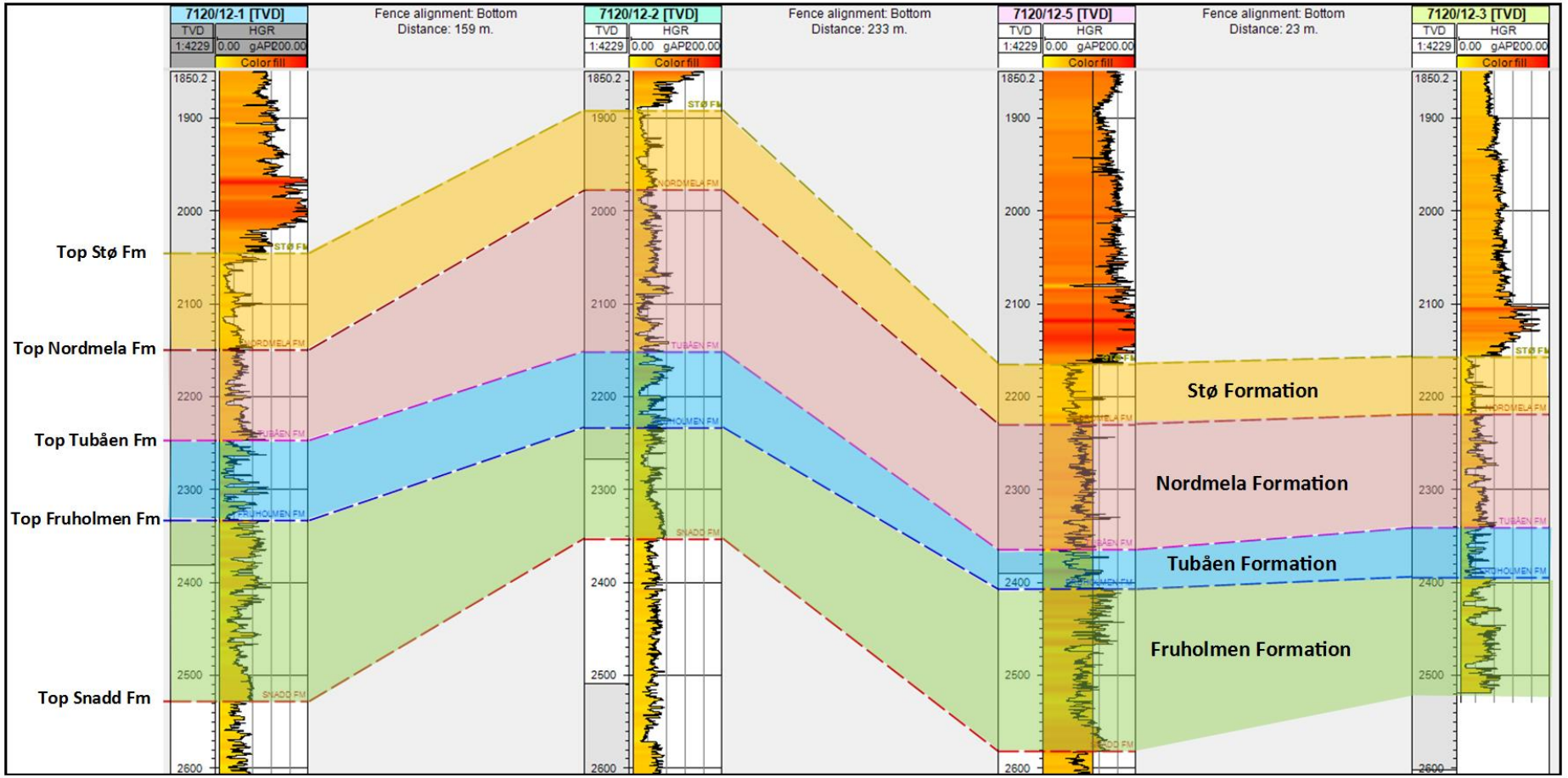

Figure 2.12: Correlation of different reservoir units based on the gamma ray log response.

2.4.3 Traps and seals

The several phases of uplift and erosion in Barents Sea has reduced the preservation potential of hydrocarbon and also affected the seal capacity especially in the inverted basinal area (Henriksen et al., 2011). The Fuglen and Hekkingen Formations of Jurassic age act as cap rocks for the most of the hydrocarbon structures penetrated in the study area (Fig. 2.13). The traps in the Jurassic reservoirs are fault-bounded positive blocks in which shales of upper Jurassic age act as seals. Triassic traps are both fault bounded and domal structure in which intra-Triassic shales act as seal to trap hydrocarbons (Dore, 1995).

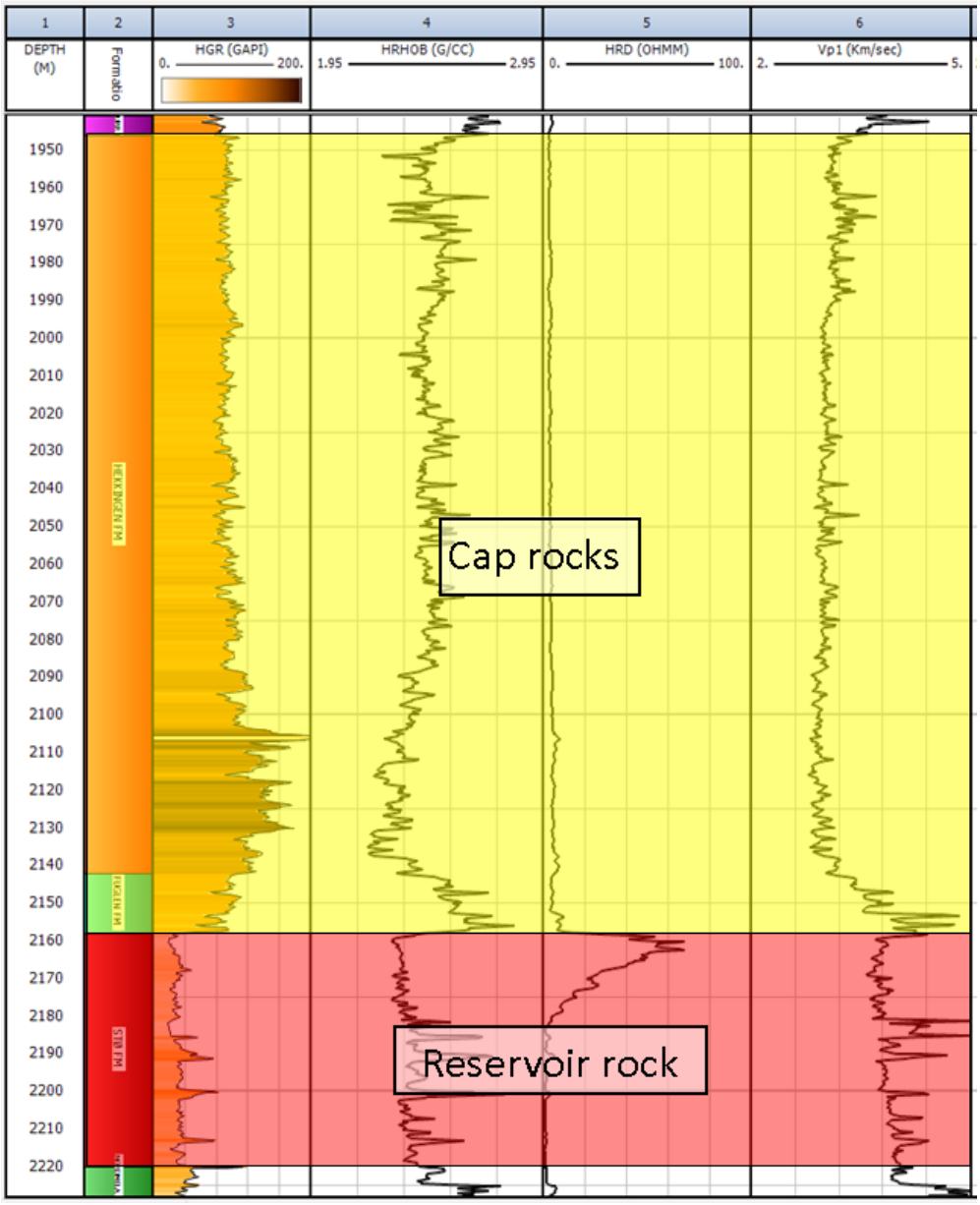

Figure 2.13: The gamma ray, density, resistivity and sonic log response of two main cap rock units (Hekkingen and Fuglen Formations) .

Chapter 3

Research methodology and theoretical background

3.1 Work flow

The research focuses on imaging reservoir quality by employing several techniques such as petrophysical analyses, rock physics diagnostics and AVO modeling of different reservoir horizons. The petrophysical analyses and rock physics diagnostics have been carried out by Interactive Petrophysics (IP) software and Microsoft Excel, while the AVO modeling is performed by the Hampson Russell software packages. As mentioned earlier the basic input to the petrophysical analyses and rock physics diagnostics are the well log data use to calculate volume of shale, net-to-gross, fluid saturation, porosity estimation. Analysis of reservoir rock properties are done by using standard rock physics templates. Finally, AVO modeling is done by employing well log and by generating synthetic seismic to investigate change in rock properties in response to change in saturation in pore fluids. A flow diagram (Fig. 3.1) describing the work flow of the thesis is given below:

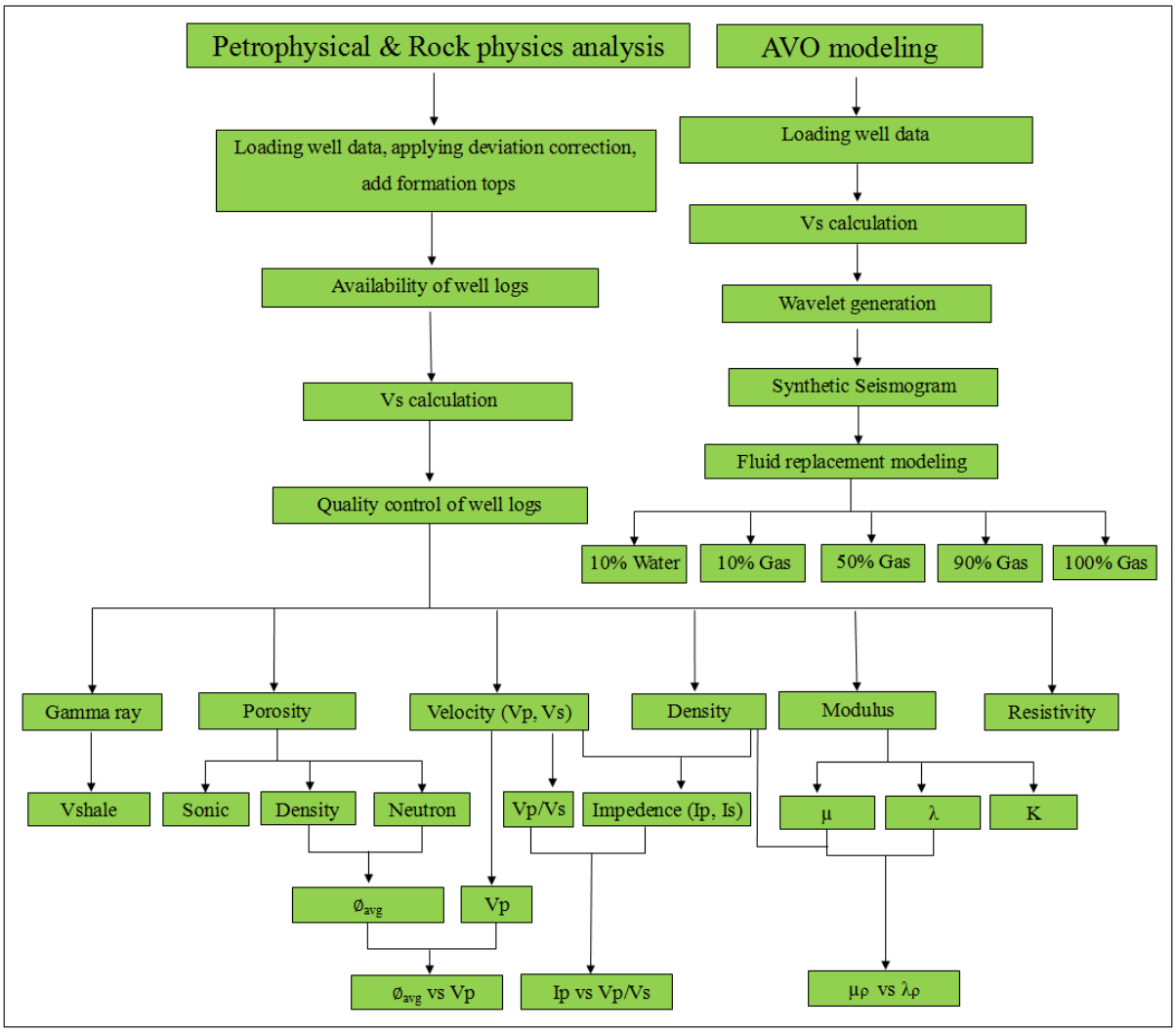

Figure 3.1: Flow chart describing the steps involved in the analysis.

3.2 Petrophysical analyses of reservoir rocks

3.2.1 Shale volume calculation

Gamma ray log is used to calculate volume of shale in porous reservoirs rocks. To calculate V_{sh}, first gamma ray index (I_{GR}) is determined by utilizing the following formula:

$$I_{GR} = \frac{GR_{log} - GR_{min}}{GR_{max} - GR_{min}} \dots\dots\dots\dots\dots\dots (3.1)$$

Where
I_{GR}= Gamma Ray Index
GR_{log}= Gamma Ray value of formation
GR_{min}= Minimum Gamma Ray (clean sand)
GR_{max}= Maximum Gamma Ray (shale)

The gamma ray log has linear as well as nonlinear empirical responses. For the linear response, first order estimation of shale volume is used where $V_{sh} = I_{GR}$. The nonlinear responses are based on geography of the area and the age of formation. Compared to the linear response, all nonlinear relationships produce a shale volume must be lower than that from the linear equation (Asquith et al., 2004).

For pre-Tertiary (consolidated) rocks, the Larionov (1969) equation has been used in the study to calculate shale volume.

$$V_{Sh} = 0.33\ (2^{2.I_{GR}} - 1) \dots\dots\dots\dots\dots\dots (3.2)$$

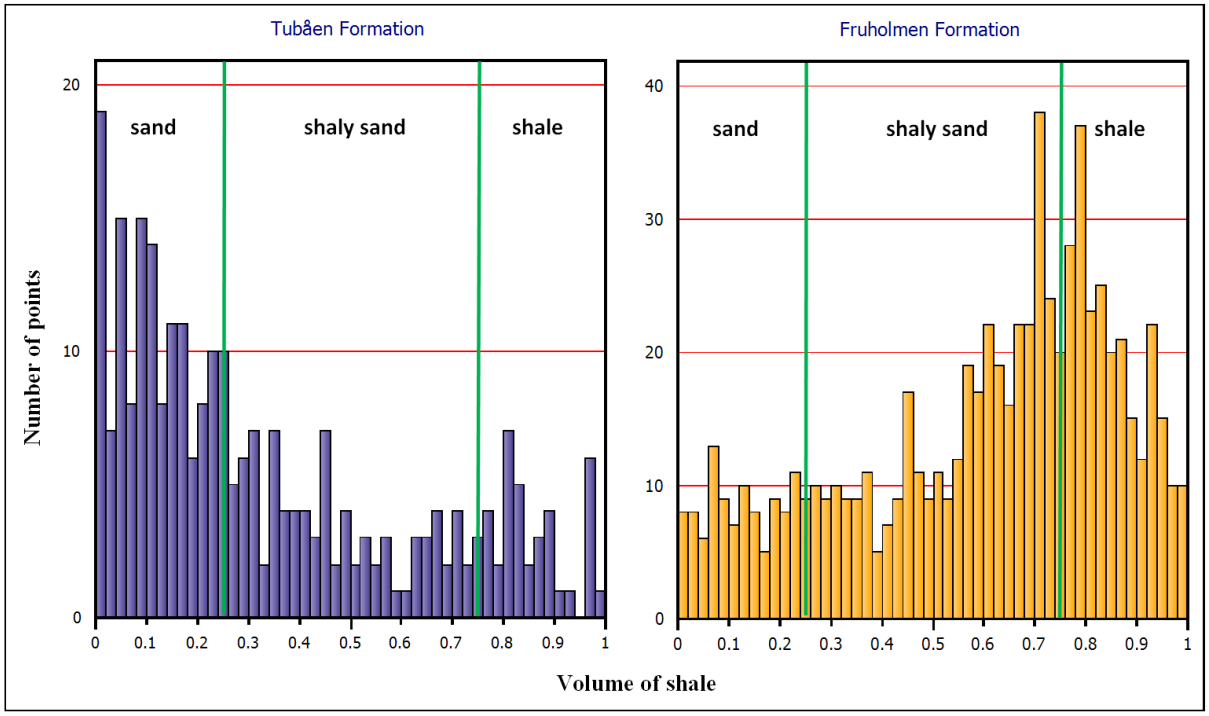

Figure 3.2: Histogram showing distributions of shale volume of Tubåen and Fruholmen Formations in the well 7120/12-3.

3.2.2 Net-to-gross estimation

Net-to-gross is the ratio between volumes of the producible reservoir rock to the total volume of the reservoir rock (Bjørlykke, 2010). At well-log scale, reservoir rocks may have high N/G but at seismic scale may have low N/G. However, N/G is useful when alternating thin beds of different lithologies and fluids are up scaled while doing rock physics analysis (Avseth et al., 2009).

The importance of net-to-gross is to find potential zones in the reservoir for hydrocarbon exploration. The net-to-gross ratio reflects the quality of the sandstone as potential reservoirs rocks. The greater value of net-to-gross ratio represents good quality of the reservoir rock (Adepelumi et al., 2011).The main reservoir rock in the study area is Stø Formation showing higher values of net-to-gross ratio as illustrated in the Table 3.1.

Table 3.1: Net-to-gross ratio of the Stø Formation in the studied wells.

Wells	Gross	Net	Net/Gross
7120/12-1	105	88.99	**0.85**
7120/12-2	86	71.83	**0.83**
7120/12-3	62	56.80	**0.92**
7120/12-4	**Absent**		
7120/12-5	65	57.33	**0.88**

3.2.3 Porosity estimation

Porosity is calculated from the density log. The density log is the measure of formations bulk density. It is the total density of a rock including solid matrix and fluid present in the pores. Density can be calculated if we know the densities of mineral (ρ_m), bulk rock (ρ_b) and fluid (ρ_f) containing oil, gas or water (Bjørlykke, 2010).

$$\emptyset_{density} = \frac{\rho_m - \rho_b}{\rho_m - \rho_f} \dots\dots\dots\dots\dots\dots (3.3)$$

Neutron logs are incorporated to estimate the porosity and the measurements are taken in neutron porosity units which are related to the formations hydrogen index, an indication of its hydrogen richness. The hydrogen in the subsurface formations exists as water, so the hydrogen index can be directly correlated with porosity. The parameter which defines the relationship between neutron log porosity and true porosity in clean formations are suitable for water filled porosity. They are also valid for oil filled formation as oil has the same hydrogen index as water. While gas bears a very low density having very low hydrogen index as compared to water, so if the gas is present the neutron porosity log will give under estimated true porosity (Rider & Kennedy, 2011).

Due to this limitation and uncertainties, the average porosity equation has been used expressed as:

$$\emptyset_{avg} = \sqrt{\frac{\emptyset^2_{density} + \emptyset^2_{neutron}}{2}} \dots\dots\dots\dots\dots\dots (3.4)$$

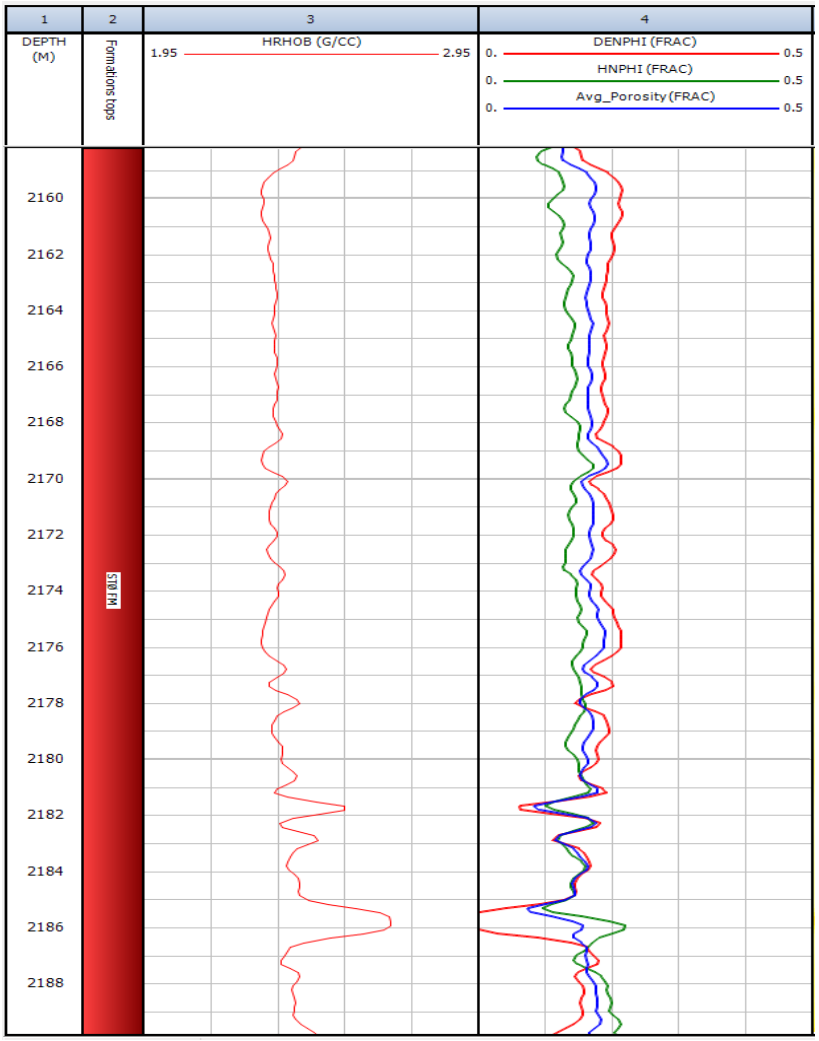

Figure 3.3: Density log and comparison between density, neutron and average porosity.

3.2.4 Fluid saturation

Before calculating saturation, we need to calculate the temperature gradient (m) which can be calculated by the following equation:

$$m = \frac{y - c}{x} \dots\dots\dots\dots\dots\dots (3.5)$$

Where y is the bottom hole temperature, c is the mean annual surface temperature taken as 4^{o}C and x is the total depth of bore hole.

Saturation of water (S_w) can be calculated by the resistivity of partly saturated rock with formation water (R_t) and the resistivity of the fully saturated rock with water (R_o).

$$S_w = (R_o/R_t)^{1/n} \dots\dots\dots\dots\dots\dots (3.6)$$

Where n is the saturation component ranges between 1.8 and 2.5.

$$\text{Since } R_o = (F.R_w/R_t)^{1/n} \dots\dots\dots\dots\dots\dots (3.7)$$

The above relation is called Arches equation (Bjørlykke, 2010).

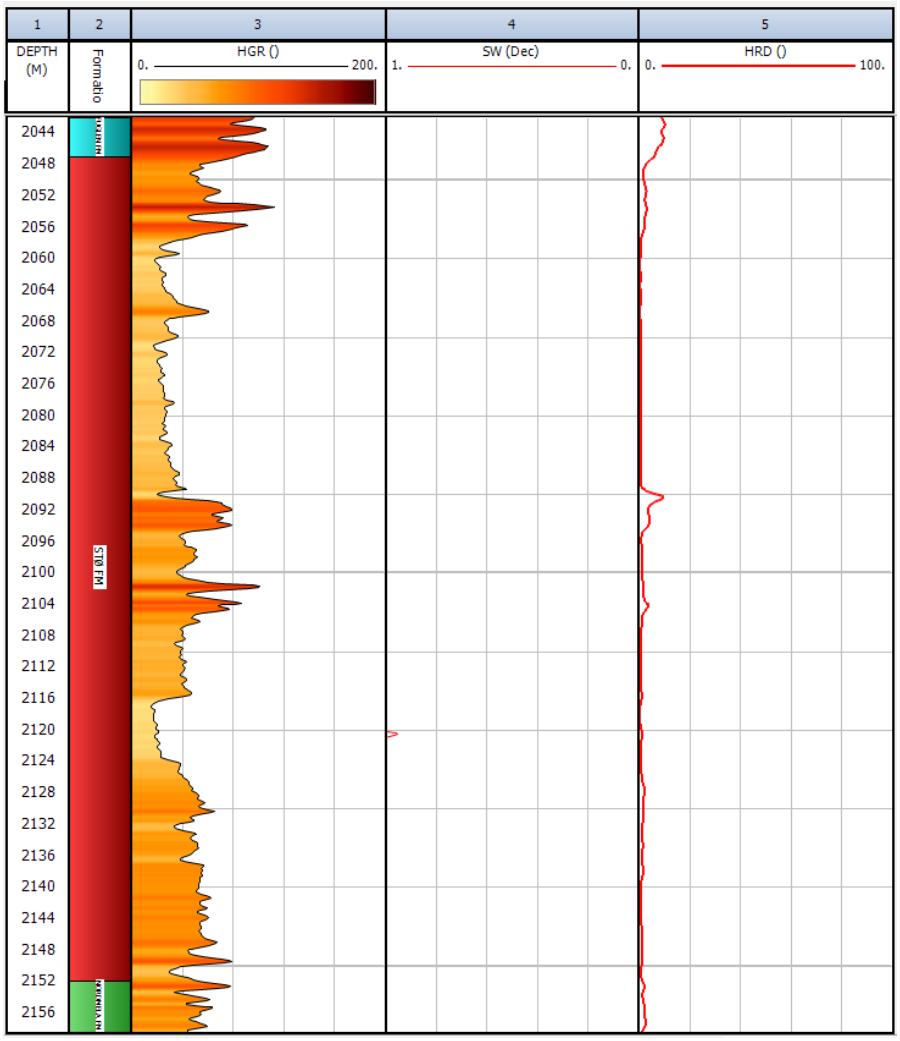

Figure 3.4: Completely water saturated Stø Formation with gamma ray and resistivity log responses.

3.3 Rock physics diagnostics

Rock physics describes a relationship between reservoir parameter such as lithology, porosity, clay content, sorting and saturation to seismic properties such as P-wave velocity, S-wave velocity, acoustic impedance and bulk density (Avseth et al., 2010). Rock physics templates (RPTs) combine the depositional and diagenetic trend models along with Gassmann fluid substitution are used for the prediction of lithology and hydrocarbons (Avseth et al., 2010). The RPTs are specific for a basin and depends on local geologic factors. Rock physics models have some geologic limitations such as lithology, mineralogy, depth of burial, pressure, and temperature. These factors have to be considered when generating RPTs for a given basin (Avseth et al., 2010).

3.3.1 Vs estimation technique

Direct shear wave velocity measurement is available in one well (7120/12-5) in the study area. For other wells, Vs is estimated employing the empirical relations of Castagna et al. (1985), Hans (1986), Krief et al. (1990), Castagna et al. (1993) and Fawad et al. (2011).

Castagna et al. (1985) derived an empirical linear relationship between P-wave and S-wave velocity, which can be written as:

$$V_s = 0.862\,V_p - 1.172\ (\mathrm{km/s}) \quad \ldots\ldots\ldots\ldots\ldots\ldots (3.8)$$

Hans (1986) introduced another relation based on ultrasonic laboratory data, which can be written as:

$$V_s = 0.794\,V_p - 0.787\ (\mathrm{km/s}) \ldots\ldots\ldots\ldots\ldots\ldots (3.9)$$

Krief et al. (1990) suggested a relationship between the squares of velocities of P-wave and S-wave, which can be expressed as:

$$Vp^2 = a\,Vs^2 + b\ (\mathrm{km/s}) \quad \ldots\ldots\ldots\ldots\ldots\ldots (3.10)$$

The regression coefficients a and b can be calculated by Krief which is summarized in the Table 3.2 (Hampson-Russell, 2004).

Table 3.2: Coefficients a and b for different lithologies used in Krief equation (Hampson-Russell, 2004).

Lithology	a	B
Sandstone (Wet)	2.213	3.857
Sandstone (Gas)	2.282	0.902
Sandstone (Shaly)	2.033	4.894
Limestone	2.872	2.755

Castagna et al. (1993) introduced another relation of least square linear fit expression as:

$$V_s = 0.804\,V_p - 0.856\ (\mathrm{km/s}) \quad \ldots\ldots\ldots\ldots\ldots\ldots (3.11)$$

Fawad et al. (2011) derived the following relation between P- and S-wave velocities expressed as:

$$V_s = 0.805\,V_p - 0.998\ (\mathrm{km/s}) \ldots\ldots\ldots\ldots\ldots\ldots (3.12)$$

The Vp-Vs relationship derived based on the available data of well 7120/12-5 that have both measured Vp and Vs. By taking the data points of Vp and Vs from this well, a regression line is generated (Fig. 3.5) which gives relation between P-wave and S-wave velocity expressed as:

$$V_s = 0.718\,V_p - 0.628\ (\mathrm{km/s}) \quad \ldots\ldots\ldots\ldots\ldots\ldots (3.13)$$

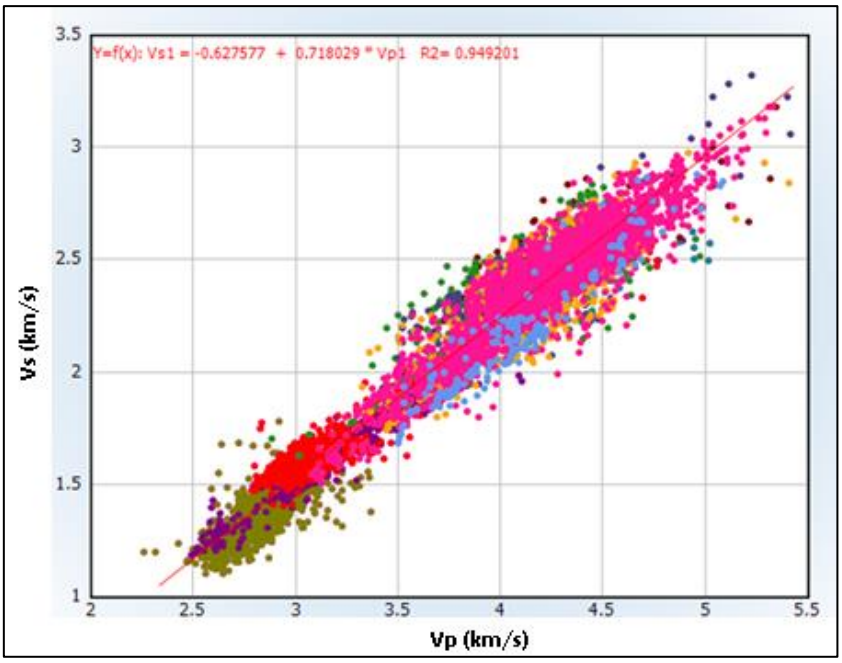

Figure 3.5: Vp-Vs plot of all data points in the well 7120/12-5 showing the empirical equation with R^2=0.949.

The comparison of Vs in Stø Formation from the well 7120/12-5 shows that Castagna (1993) equation (red) has a good correlation with measured Vs (black) than others Vs equations (Fig. 3.6)

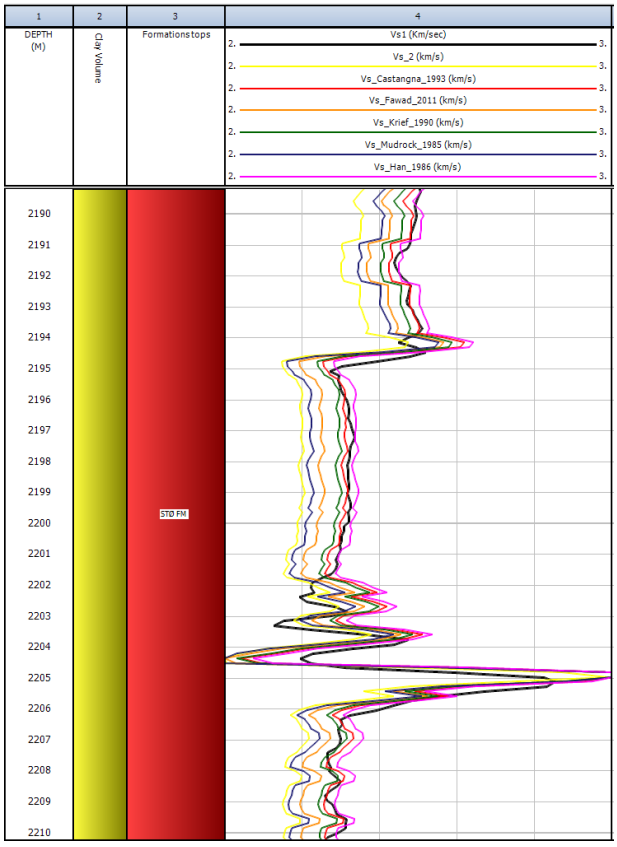

Figure 3.6: The comparison of Vs of Stø formation in the well 7120/12-5.

The bulk modulus (K) and shear modulus (μ) are calculated by the following equations:

$$K = \rho\left(V_p^2 - \frac{4}{3}V_s^2\right) \ldots\ldots\ldots\ldots\ldots\ldots (3.14)$$

$$\mu = \rho\, V_s^2 \ldots\ldots\ldots\ldots\ldots\ldots (3.15)$$

Poisson's ratio (v) is calculated by the expression:

$$v = \frac{0.5\left(\frac{V_p}{V_s}\right)^2 - 1}{\left(\frac{V_p}{V_s}\right)^2 - 1} \ldots\ldots\ldots\ldots\ldots\ldots (3.16)$$

3.3.2 Rock physics crossplots

3.3.2.1 Porosity versus velocity

Han (1986) introduced a number of empirical equations relating ultrasonic velocities to porosity and clay content. The correlation is precise if the velocities of clean sandstone can be related empirically to porosity. For water-saturated clean sandstones at 40 MPa, the equations are:

$$V_p = 6.08 + 8.06\,\emptyset \ldots\ldots\ldots\ldots\ldots\ldots (3.17)$$

$$V_s = 4.06 + 6.28\,\emptyset \ldots\ldots\ldots\ldots\ldots\ldots (3.18)$$

But for shaley sandstone, the correlation between velocity and porosity became relatively poor which became accurate if clay volume is included in the regression (Fig 3.7). For shaly sandstone at 40 MPa, the equations are:

$$V_p = 5.59 + 6.96\,\emptyset - 2.13\,C \ldots\ldots\ldots\ldots\ldots\ldots (3.19)$$

$$V_s = 3.52 + 4.91\,\emptyset - 1.89\,C \ldots\ldots\ldots\ldots\ldots\ldots (3.20)$$

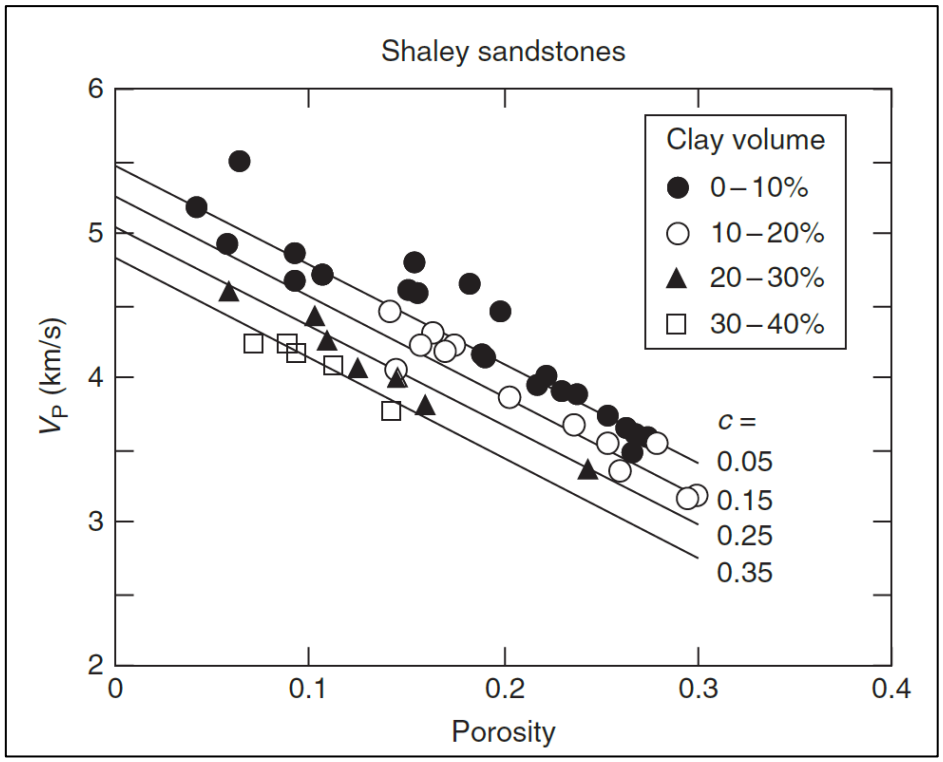

Figure 3.7: Han's water-saturated ultrasonic velocity data at 40 MPa with his empirical relations at four different clay fractions (Mavko et al., 2009).

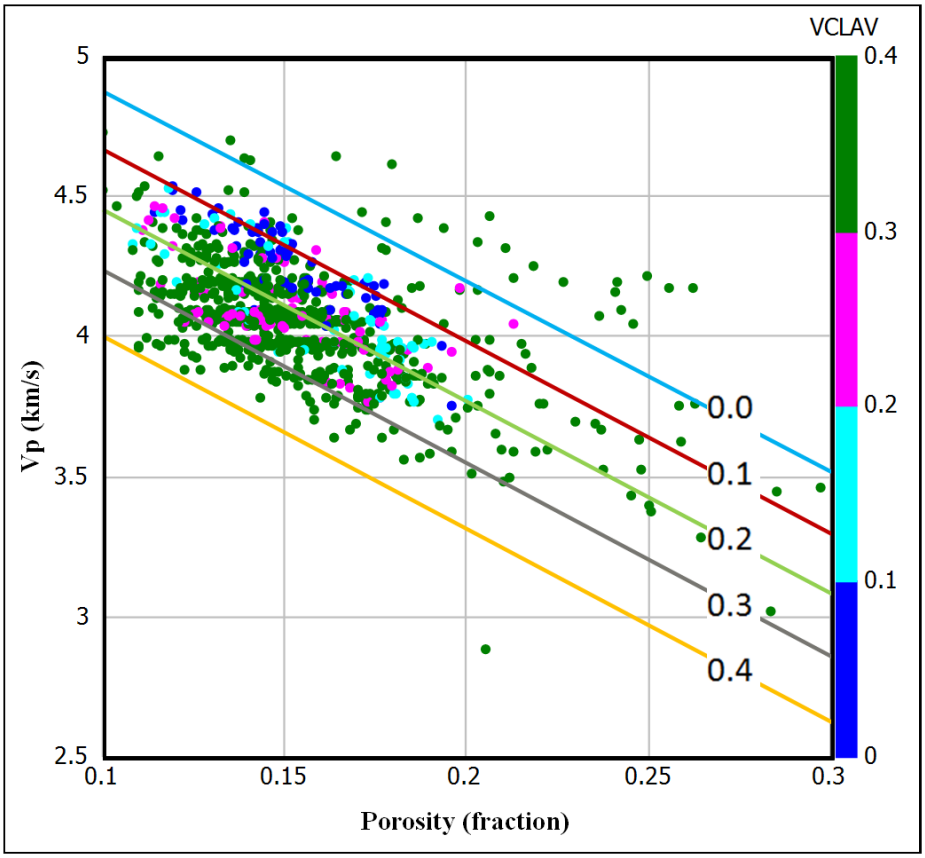

Figure 3.8: Nordmela Formation data points superimposed on Han's (1986) empirical relations at four different clay fractions in the well 7120/12-5.

Wyllie et al. (1956) relates velocity and porosity in sedimentary rocks if they have a uniform mineralogy, high effective pressure and they are fluid-saturated. The relation is also called time-average equation expressed as:

$$\frac{1}{Vp} = \frac{\emptyset}{V_{p-fl}} + \frac{1-\emptyset}{V_{p-0}} \dots\dots\dots\dots\dots\dots (3.21)$$

Where V_P is the P-wave velocity of saturated rock, $V_{P\text{-}0}$ is the velocity of the mineral matrix and $V_{P\text{-}fl}$ are the P-wave velocity of the pore fluid.

Raymer et al. (1980) proposed two relations to relate P-wave velocity to travel:

$$V = (1-\emptyset)^2 V_o + \emptyset V_{fl} \qquad \emptyset < 37\% \dots\dots\dots\dots\dots\dots (3.22)$$

$$\frac{1}{\rho V_p} = \frac{\emptyset}{\rho_{fl} V_{fl}^2} + \frac{(1-\emptyset)}{\rho_p V_o^2} \quad \emptyset > 47\% \dots\dots\dots\dots\dots\dots (3.23)$$

Figure 3.9 shows a comparison of estimations by Raymer et al. (1980), Wyllie et al. (1956), and Gardner et al. (1974) between velocity and porosity for water-saturated clay-free sandstones. The Wyllie et al. (1956) equation underestimates for the values of consolidated and cemented sandstone while Gardner et al. (1974) equation under predicts all of the measured values. Uncemented sandstone is not modeled by any of the above equations.

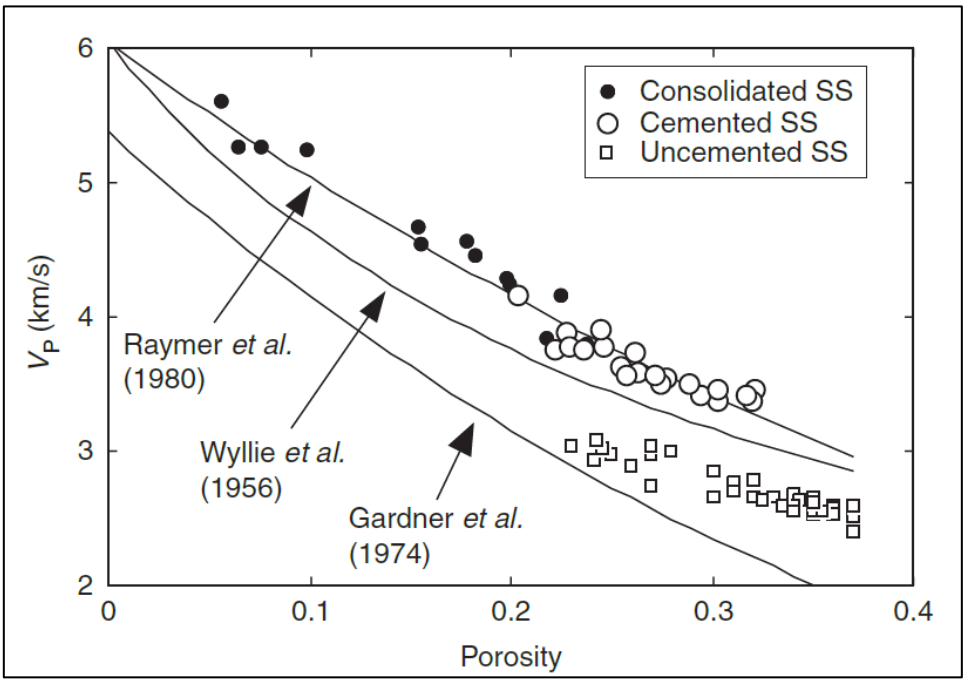

Figure 3.9: Velocity versus porosity in water-saturated clay-free sandstones (Mavko et al., 2009).

Dvorkin and Nur (1996) introduced techniques for the rock physics diagnostics to infer the microstructure of rock from the relation of velocity and porosity. There are three models for the medium to high porosity sandstones (Fig. 3.10).

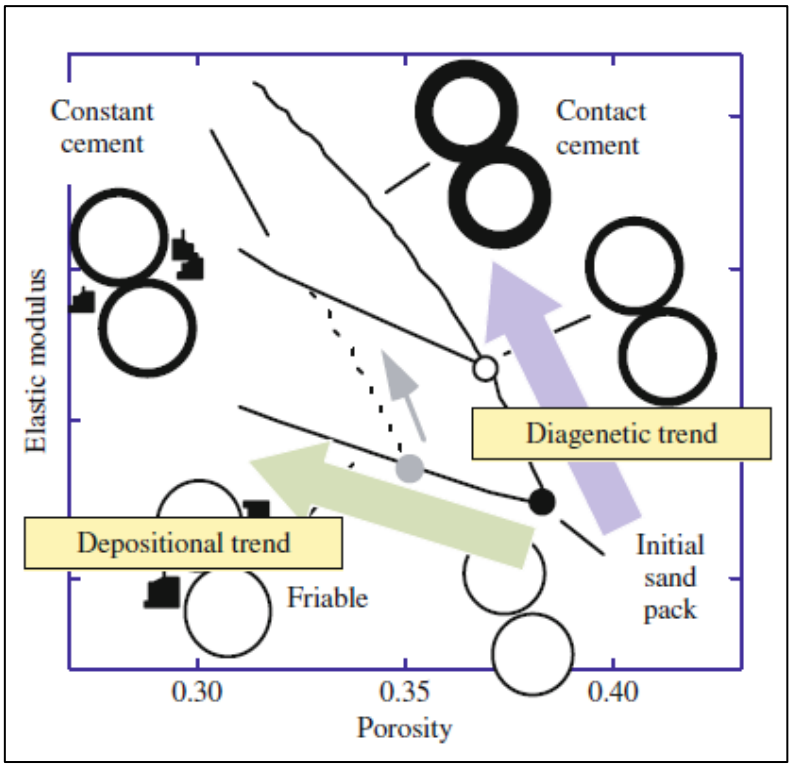

Figure 3.10: Cement models plotted with porosity versus elastic modulus (Avseth, 2010).

The friable-sand model

Dvorkin and Nur (1996) introduce the theoretical model for high-porosity sands. The friable-sand model also known as unconsolidated line explains the velocity porosity changes as the sorting deteriorates. This model corresponds to the poorly sorted sands. The smaller grains deposited in the pore space deteriorates the grain sorting, decreases the porosity with slightly increase in the stiffness of rock. The uncertainties behind the friable-sand model are related with grain contacts heterogeneities, tangential slip, and highly variable coordination number (Avseth et al., 2010).

The contact-cement model

Sandstone gets more cemented with the increase in burial depth. The cement may be quartz, calcite and albite. The assumption of contact-cement model is that porosity decreases with initial porosity of a sand pack as a result of the uniform deposition of cement layers on the surface of the grains (Avseth et al., 2010).

The constant-cement model

The constant-cement model assumes that sands of variable sorting and porosity have same quantity of contact cement. The variation of porosity is due to non-contact pore-filling material (Avseth et al., 2009).

Figure 3.11 shows three cement models which are used during the rock physics analysis. Contact and constant cement lines are taken from Avseth et al. (2010) while friable sand model is taken from Dvorkin and Nur (1996). The cement fraction is taken as 2% in the constant cement line.

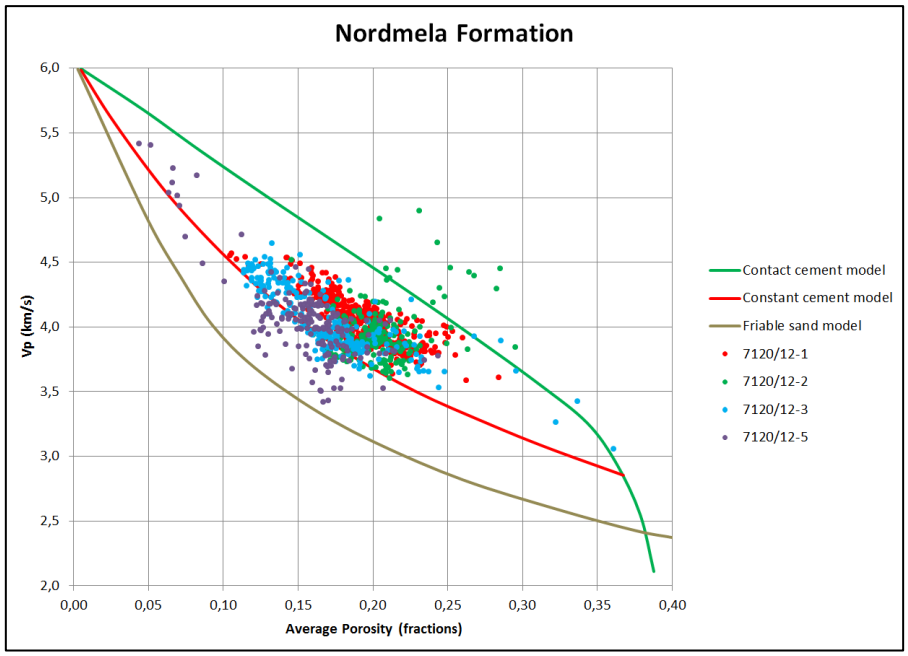

Figure 3.11: Vp-porosity crossplot of Nordmela Formation. The data plotted here are taken from four wells.

3.3.2.2 AI versus Vp/Vs

In the crossplot of AI versus Vp/Vs, the existence of diagenetic quartz cement shifted the brine-saturated sandstone zone to a region of very low Vp/Vs where saturated hydrocarbon sandstone zone could be expected (Avseth et al., 2010).

Rock physics template of AI versus Vp/Vs includes shale trend line, brine sand line and curves for increasing gas saturation. The black arrows in the Figure 3.12 illustrate several geological trends such as: 1) increasing shaliness, 2) increasing cement volume 3) increasing porosity, 4) decreasing effective stress and 5) increasing gas saturation (Avseth et al., 2005).

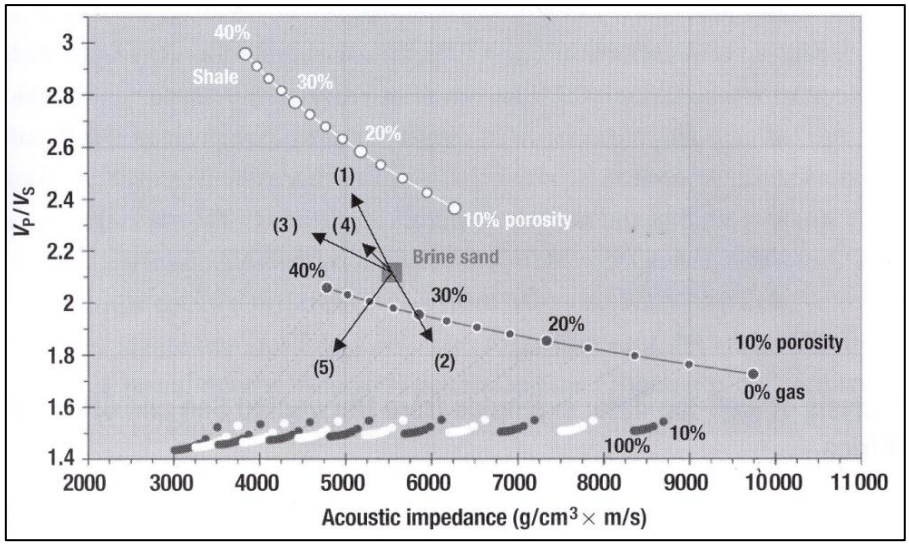

Figure 3.12: A standard rock physics template (RPT) explains relationship between Acoustic Impedance and Vp/Vs (Avseth et al., 2005) is very useful to discriminate lithology and pore fluids of siliciclastic rocks.

Figure 3.13 shows rock physics template (RPT) displaying water, oil and gas saturated models used in the study area. There are some steps involved for the construction of this template. First step is to compute the dry bulk and shear modulus at critical porosity by applying Hertz-Mindlin theory. Second step is to interpolate between the high-porosity and zero-porosity mineral point by using the modified Hashim-Shtrikman bound. Third step is to perform Gassmann fluid substitution, calculate elastic properties of clean sands and saturation of brine and hydrocarbons at all porosities (Avseth et al., 2010).

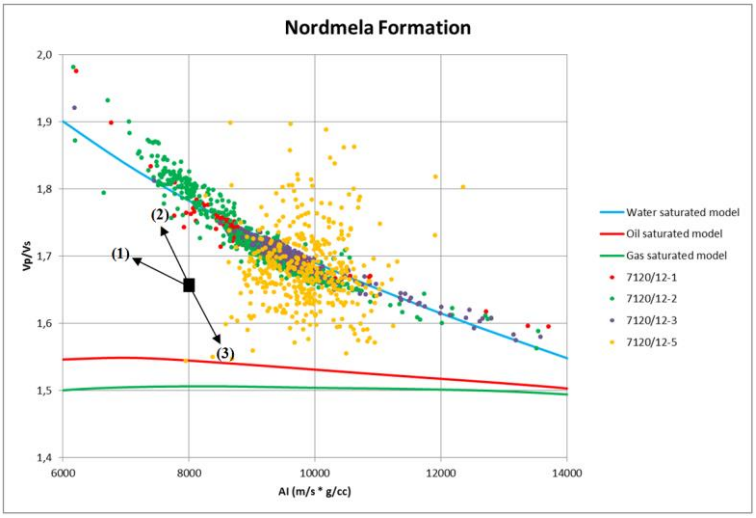

Figure 3.13: Cross plot of Acoustic Impedance versus Vp/Vs of Nordmela Formation in four wells. The first arrow (1) shows the trend of increasing porosity, the second arrow (2) shows the trend of increasing shaliness and the third arrow (3) shows the trend of increasing cement volume.

3.3.2.3 Lambda-Rho versus Mu-Rho

Cross plot of Lambda-Rho versus Mu-Rho is used to separate different lithologies along orthogonal boundaries (Fig 3.14) and gives useful information about the nature of fluids present in the rock. Areas of low incompressibility show either gas or coal but rigidity differentiate them because coal have low rigidity and gas sand has high rigidity (Gelius and Johansen, 2010). The low value of Lambda-Rho indicates increasing gas saturation. Sand exhibits a higher value of Mu-Rho because the sand matrix is mostly composed of quartz mineral which has a higher rigidity as compared to clay mineral (Young and Tatham, 2007).

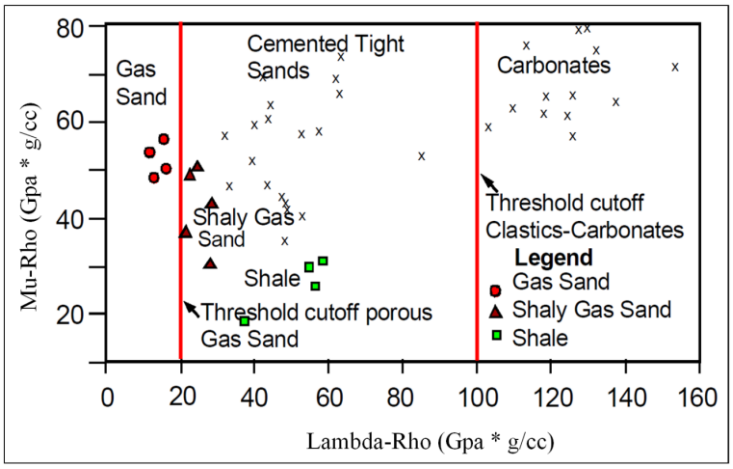

Figure 3.14: Cross plot of Lambda-Rho versus Mu-Rho (Modified after Goodway, 2001).

3.4 AVO modeling

3.4.1 Gassmann fluid substitution

Gassmann's (1951) equations are used to calculate changes in seismic velocity due to different fluid saturations in reservoirs. These equations are widely used in the analysis of direct hydrocarbon indicators (DHI), amplitude versus offset (AVO) and time-lapse reservoir monitoring (Han and Batzle, 2004).

Gassmann's (1951) relation predicts the bulk and shear modulus for rocks saturated with different fluids expressed as:

$$K_{sat} = K_{dry} + \frac{\left(1 - \frac{K_{dry}}{K_{min}}\right)^2}{\frac{\emptyset}{K_{fl}} + \frac{1-\emptyset}{K_{min}} - \frac{K_{dry}}{K_{min}^2}} \dots\dots\dots\dots\dots\dots (3.24)$$

$$\mu_{sat} = \mu_{dry} \dots\dots\dots\dots\dots\dots (3.25)$$

Where K_{sat} and μ_{sat} represents the saturated bulk and shear modulus respectively, K_{dry} and μ_{dry} represents bulk and shear modulus of frame or dry rock respectively, K_{min} is the bulk modulus of mineral or grain, K_{fl} is the bulk modulus of the fluid and $\emptyset$ is the porosity of the rock.

For porous rocks, Gassmann's relation is based on the following assumptions: (Adam et al., 2006)

- The pore pressure between pores is in equilibrium which can occur at very low frequencies, where the fluid has enough time to reach equilibrium. The relaxation time depends on viscosity and density of the fluid and permeability of the rock.
- The porous frame composed of a monomineralic material.
- All the pores are connected and are homogeneously filled with a nonviscous fluid.
- The system is assumed to be closed, undrained and the pore fluid does not affect the solid frame chemically.

3.4.2 Synthetic seismogram

The seismic trace obtainted x(t) is the convolution of source wavelet s(t) and earth reflectivity series r(t) plus the noise (Fig.3.16) expressed as:

$$X(t) = s(t) * r(t) + \text{Noise} \dots\dots\dots\dots\dots\dots (3.26)$$

In the above equation, the effects due to transmission losses, geometric spreading and frequency-dependent absorptions are ignored. A wavelet is a type of mathematical function which separate a given function into various frequency components. The study of each component with a resolution that is coherent with its scale (Mondol, 2010).

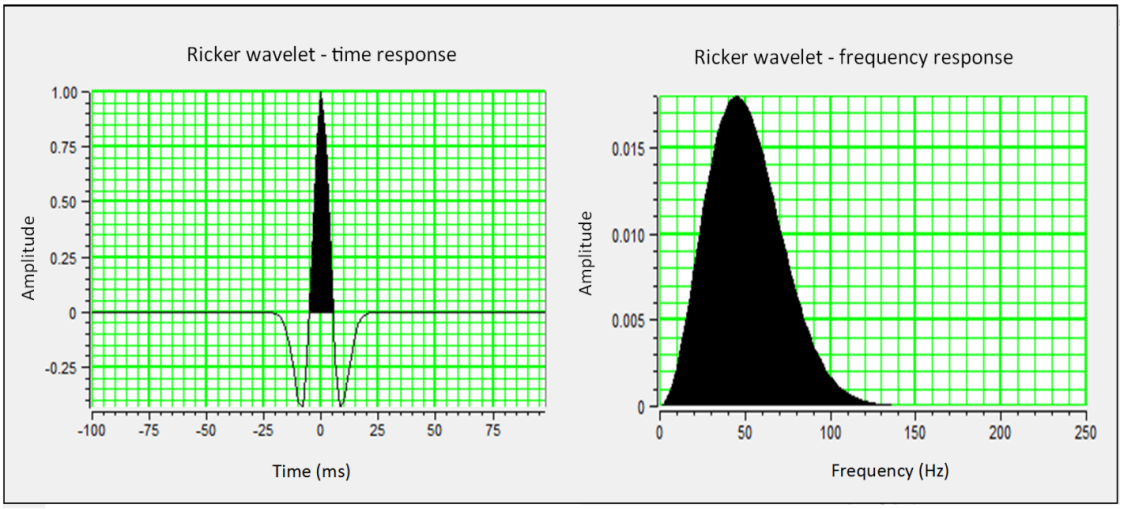

Figure 3.15: Ricker wavelet showing time and frequency response which is used for the generation of synthetic seismogram.

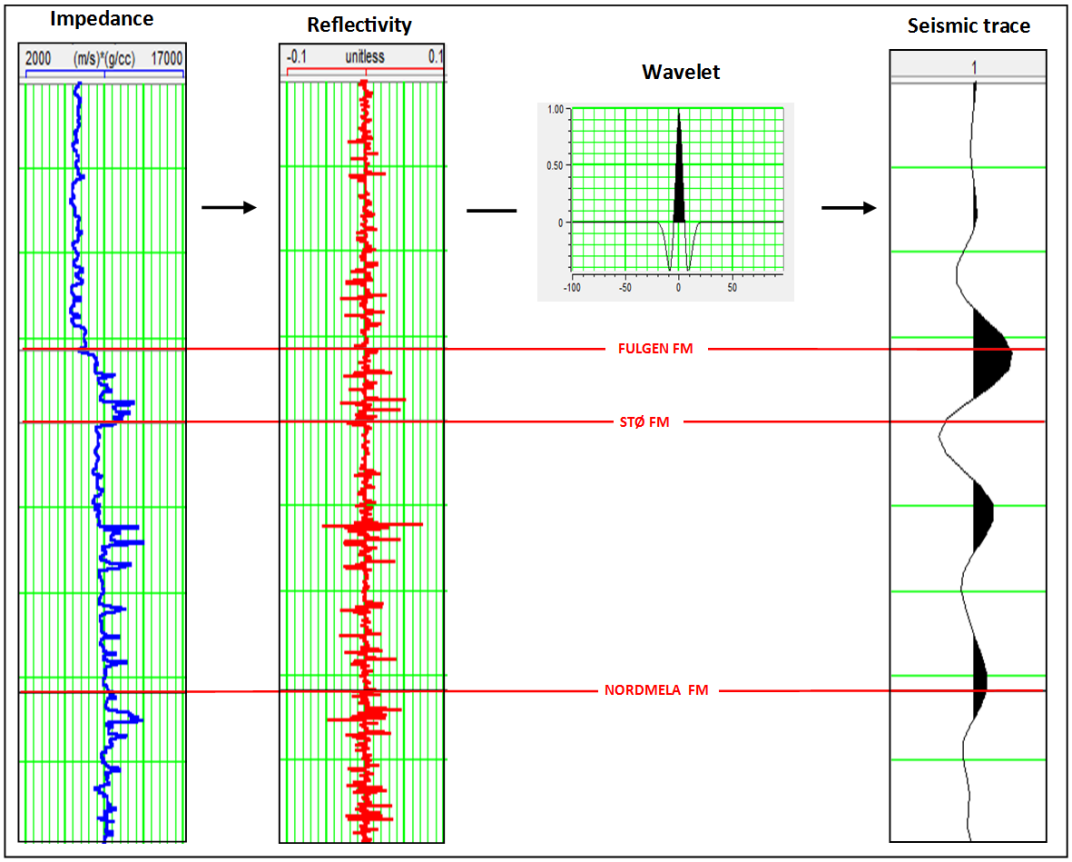

Figure 3.16: Seismic trace is obtained by convolution of wavelet and reflectivity series in the well 7120/12-3.

3.4.3 Angle dependent reflection coefficient

When a seismic wave travels into the earth and strike an interface with velocity and density contrasts, the energy of the incident wave is partitioned at each boundary. An incident P-wave is converted to transmitted P and S-wave and reflected P and S-wave (Fig. 3.17)

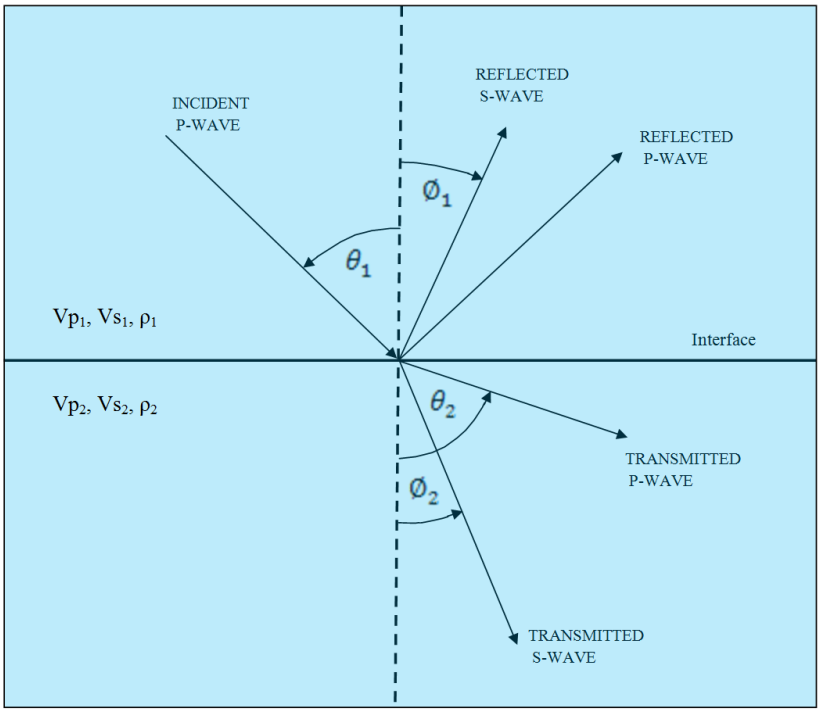

Figure 3.17: Reflection and transmission at an interface for an incident P-wave (Modified after Castagna, 1993).

According to Snell's law, the incident, transmitted and reflected waves are related by the expression:

$$p = \frac{\sin\theta_1}{V_{p1}} = \frac{\sin\theta_2}{V_{p2}} = \frac{\sin\emptyset_1}{V_{s1}} = \frac{\sin\emptyset_2}{V_{s2}} \dots\dots\dots\dots\dots\dots (3.27)$$

Where V_{p1} and Vs_1 are the P-wave and S-wave velocity in medium 1, Vp_2 and Vs_2 are the P-wave and S-wave velocity in medium 2, θ_1 and θ_2 are the incident and transmitted P-wave angle, $\emptyset_1$ and $\emptyset_2$ are reflected and transmitted S-wave angle (Castagna, 1993). At normal incidence, the P-wave reflection coefficient is given by the relations:

$$R_p = \frac{I_{p2} - I_{p1}}{I_{p2} + I_{p1}} = \frac{\rho_2 V_2 - \rho_1 V_1}{\rho_2 V_2 + \rho_1 V_1} \dots\dots\dots\dots\dots\dots (3.28)$$

3.4.4 Approximations of the Zoeppritz equations

The Zoeppritz equations help to describe the amplitudes of a reflected P wave as a function of angle, but do not give understanding of how these amplitudes relate to the various physical parameters. There are several approximations to the Zoeppritz equations.

Aki and Richards (1980) gives a linearized approximation to the Zoeppritz equations for the P-wave reflection coefficient expressed as:

$$R_{pp(\theta)} = \frac{1}{2}\left[\frac{\Delta V_p}{V_p} + \frac{\Delta\rho}{\rho}\right] - \left(\frac{V_s}{V_p}\right)^2 \left[2\,\frac{\Delta V_s}{V_s} + \frac{\Delta\rho}{\rho}\right] \mathrm{Sin}^2\,\theta + \frac{1}{2}\frac{\Delta V_p}{V_p} Tan^2\theta \dots\dots\dots\dots\dots\dots (3.29)$$

Where $\Delta V_p = V_{p2} - V_{p1}$, $\Delta V_s = V_{s2} - V_{s1}$, $V_{p2} = \frac{V_{p1}+V_{p2}}{2}$, $V_{s2} = \frac{V_{s1}+V_{s2}}{2}$

Wiggen or Gefland's (1986) approximation assumes small angles (tanθ = sinθ) and Vp/Vs=2, the equation (3.29) is simplified as:

$$R_{pp}(\theta) = R_p + GSin^2\theta \dots\dots\dots\dots\dots\dots (3.30)$$

Where $G = R_p + 2R_s$ and Rp and Rs are the zero-offset reflection coefficient for P- and S-wave calculated

$$R_p = \frac{1}{2}\left[\frac{\Delta V_p}{V_p} + \frac{\Delta\rho}{\rho}\right]$$

$$R_s = \frac{1}{2}\left[\frac{\Delta V_s}{V_s} + \frac{\Delta\rho}{\rho}\right]$$

Poisson's ratio (v) is related to Vp/Vs by the relation:

$$v = \frac{0.5\left(\frac{V_p}{V_s}\right)^2 - 1}{\left(\frac{V_p}{V_s}\right)^2 - 1} \dots\dots\dots\dots\dots\dots (3.31)$$

Differentiation of the above equation gives

$$\Delta v = \frac{\left(\frac{\mathrm{V_p}}{\mathrm{V_s}}\right)^2\left(1 - 2v\left[\frac{\Delta \mathrm{V_p}}{\mathrm{V_p}} + \frac{\Delta \mathrm{V_s}}{\mathrm{V_s}}\right]\right)}{\left[\left(\frac{V_p}{V_s}\right)^2 - 1\right]} \dots\dots\dots\dots\dots\dots (3.32)$$

By taking Vp/Vs=2 and v=1/3, the above equation become

$$\Delta v = \left(R_p + G\right).\frac{4}{9} \dots\dots\dots\dots\dots\dots (3.33)$$

The above equation is the Shuey (1985) approximation. The change in Poisson's ratio can be calculated if we know the values of Rp and G.

Smith and Gidlow (1987) gave another approximation based on Gardner's equation which relates density and velocity expressed by the following relation:

$$\rho = \alpha {V_p}^{1/4} \dots\dots\dots\dots\dots\dots (3.34)$$

The differentiation gives the following form to above equation as:

$$\frac{\Delta\rho}{\rho} = \frac{1}{4}\frac{\Delta V_p}{V_p} \dots\dots\dots\dots\dots\dots (3.35)$$

Then substituting the above equation into Aki and Richard's equation,

$$R_{pp(\theta)} = \left[\frac{5}{8} - \frac{1}{2}\left(\frac{V_s}{V_p}\right)^2 Sin^2\theta + tan^2\theta\right]\frac{\Delta V_p}{V_p} - \left[4\left(\frac{V_s}{V_p}\right)^2 Sin^2\theta\right]\frac{\Delta V_s}{V_s} \ldots\ldots\ldots\ldots\ldots\ldots (3.36)$$

The comparison of results obtained for a simple gas sand model at the top and bottom interfaces, using the full Zoeppritz calculations, and the approximations of Shuey, Gefland, and Aki-Richard's are illustrated in the Figure 3.18. All the Zoeppritz approximations are best up to 20 degree within 2% accuracy. Gelfand's approximation is best up to 35 degree while Shuey's approximation is best for full range of angles (Gelius and Johansen, 2010). In the study area, synthetic seismograms are generated by Zoeppritz equations while intercept-gradient plots are generated by using Aki and Richards Approximation.

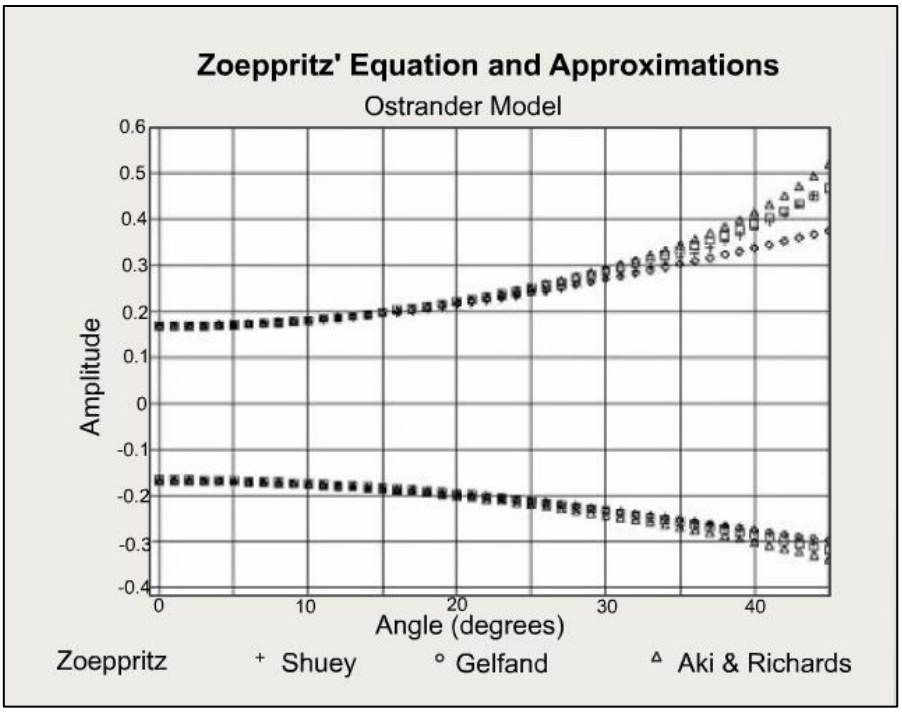

Figure 3.18: Comparison of the Zoeppritz equations and its approximations based on simple gas sand model (Gelius and Johansen, 2010).

3.4.5 Classification of gas sand

Rutherford and William (1989) classified four types of gas sands based on impedance and characteristic of AVO (Fig. 3.19).

Class 1 shows high impedance sand whose impedance is greater than the surrounding shale rock. The reflection coefficient is positive and decreases with offset/angle which may have reverse polarity on far angle offset. Class 1 shows moderate to highly compacted sands which are related to onshore area (Gelius and Johansen, 2010).

Class 2 shows sand whose impedance is identical to the surrounding rock. This class shows moderately compacted sand related to both onshore and offshore areas. The polarity changes if the zero-offset reflection coefficient is positive. Class 3 and Class 4 show low impedance sand having impedance less than the surrounding material and are related with marine environment. The reflection coefficient increases with offset in Class 3 which decreases with offset in Class 4 (Gelius and Johansen, 2010).

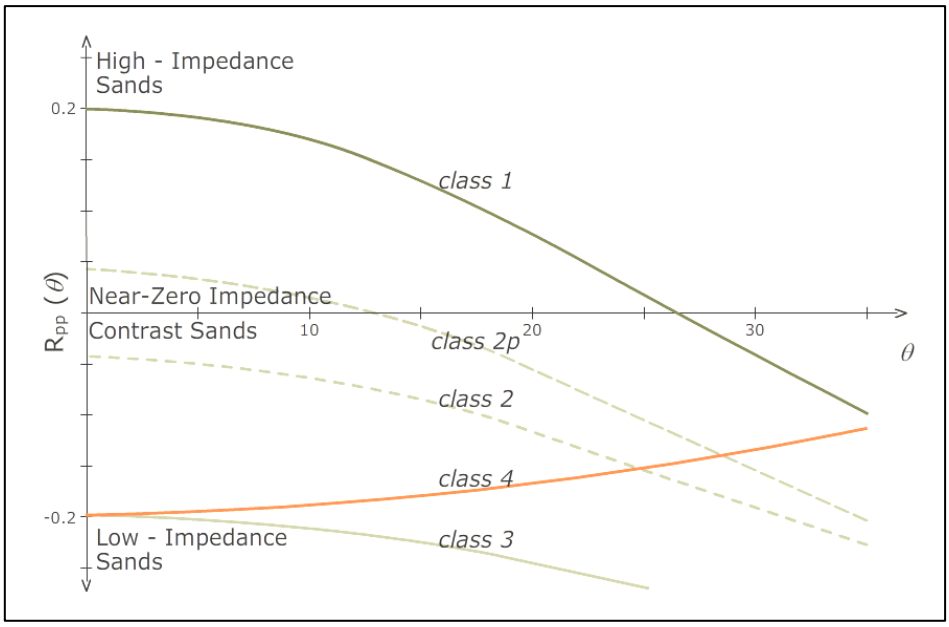

Figure 3.19: AVO Classes of gas sand (Gelius and Johansen, 2010).

AVO classes can also be represented in terms of cross plotting AVO gradient (B) against AVO intercept (A) (Fig.3.20). In the A-B plane, brine-saturated sandstones and shales follow a "background" trend also known as "mudrock line". The deviations from the background trend represent an indication of anomalous hydrocarbon zones. The reflection from top of gas-sand fall below the background trend, while the reflection from bottom of gas-sand fall above the background trend (Castagna et al., 1998).

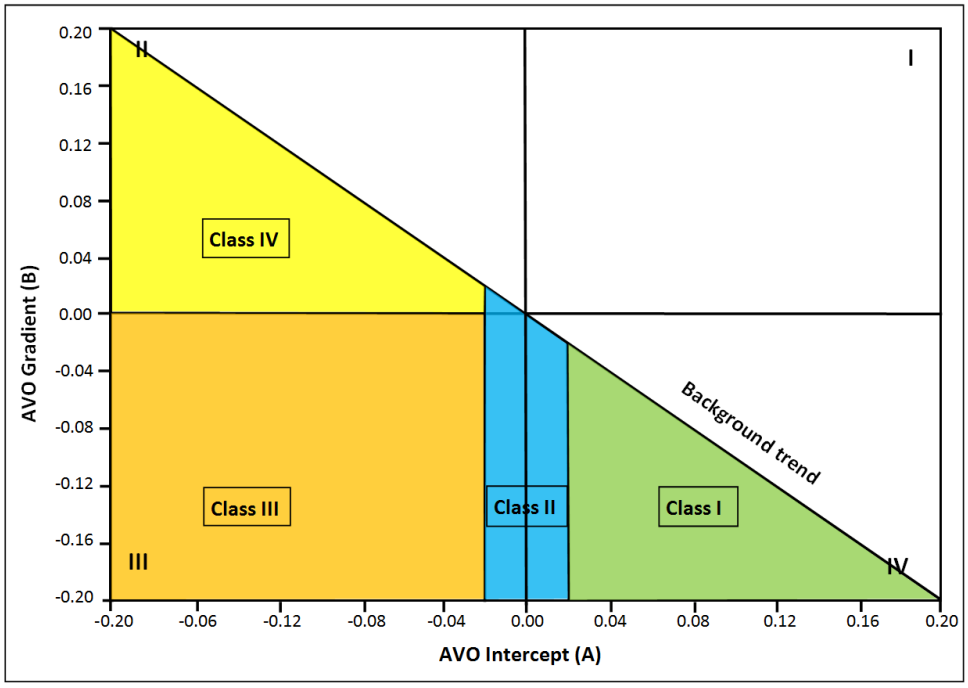

Figure 3.20: Cross plot of AVO intercept (A) versus gradient (B) (Modified after Castagna et al., 1998).

The Class III gas sands occur in quadrant III having negative AVO intercept and gradient. These sands are excellent indicator of gas as the amplitude increase with offset. High-

impedance gas sands of Class I occur in quadrant IV with positive AVO intercept and negative gradient. However, quadrant II gas sands have negative intercept and positive gradient (Castagna et al., 1998). Table 3.3 shows the AVO response for the various types of gas sand classes.

Table 3.3: Summary of top gas sand reflection coefficient for the Rutherford and William classification (Castagna et al., 1998).

Class	Relative Impedance	Quadrant	A	B	Amplitude vs. Offset
I	Higher than overlying unit	IV	+	-	Reflection coefficient decrease with increasing offset
II	About the same as the overlying unit	III or IV	+ or -	-	Reflection magnitude may increase or decrease with offset, and may have reverse polarity
III	Lower than the overlying unit	III	-	-	Reflection magnitude increases with offset
IV	Lower than the overlying unit	II	-	+	Reflection magnitude decreases with offset

Chapter 4

Petrophysical analyses of reservoir rocks

Petrophysical analyses of reservoir rocks

Petrophysical analyses involves the transformation of well logs into reservoir properties such as porosity, shale volume, net-to-gross ratio and fluid saturation. The analyses of reservoir rock properties helps for the determination of hydrocarbon zones, thickness of the reservoir zones and to distinguish between gas, oil and water bearing rocks. The well logs utilized in the petrophysical analyses are gamma ray, density, neutron, sonic and resistivity logs. The petrophysical analyses are carried out in the five studied wells (Fig. 4.1). The reservoir properties of the Kapp Toscana Group including the Stø, Nordmela, Tubåen, Fruholmen and Snadd Formations have been analyzed with great emphasis on Stø Formation.

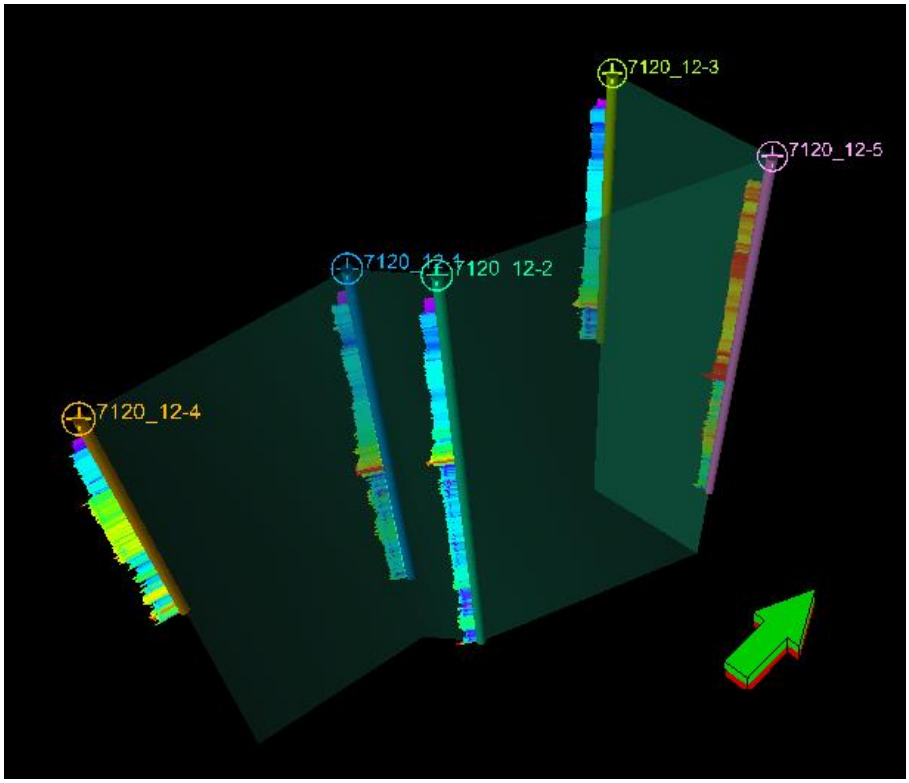

Figure 4.1: Fencing shows the location of wells penetrated in the study area.

4.1 Shale volume calculation

The first step in petrophysical analysis is the shale volume estimation which can be determined by defining the clean sand and shale base line on the gamma ray log. For shale volume calculation, cutoff is applied on the shale volume. The values of shale volume less than 0.25 considered as sand data points, between 0.25 and 0.75 considered as shaly sand and sandy shale and greater than 0.75 considered as shale data points.

Figure 4.2 showing the histogram illustrating the distribution of volume of shale in the Stø Formation encountered in the four wells (7120/12-1, 7120/12-2, 7120/12-3 and 7120/12-5). In the wells 7120/12-3 and 7120/12-5, Stø Formation has most of the data points occur in the sand range with minor quantity of shaly sand and shale. The Stø Formation in the well 7120/12-1 and 7120/12-2 also have greater occurrence of sand points with considerable amount of shaly sand.

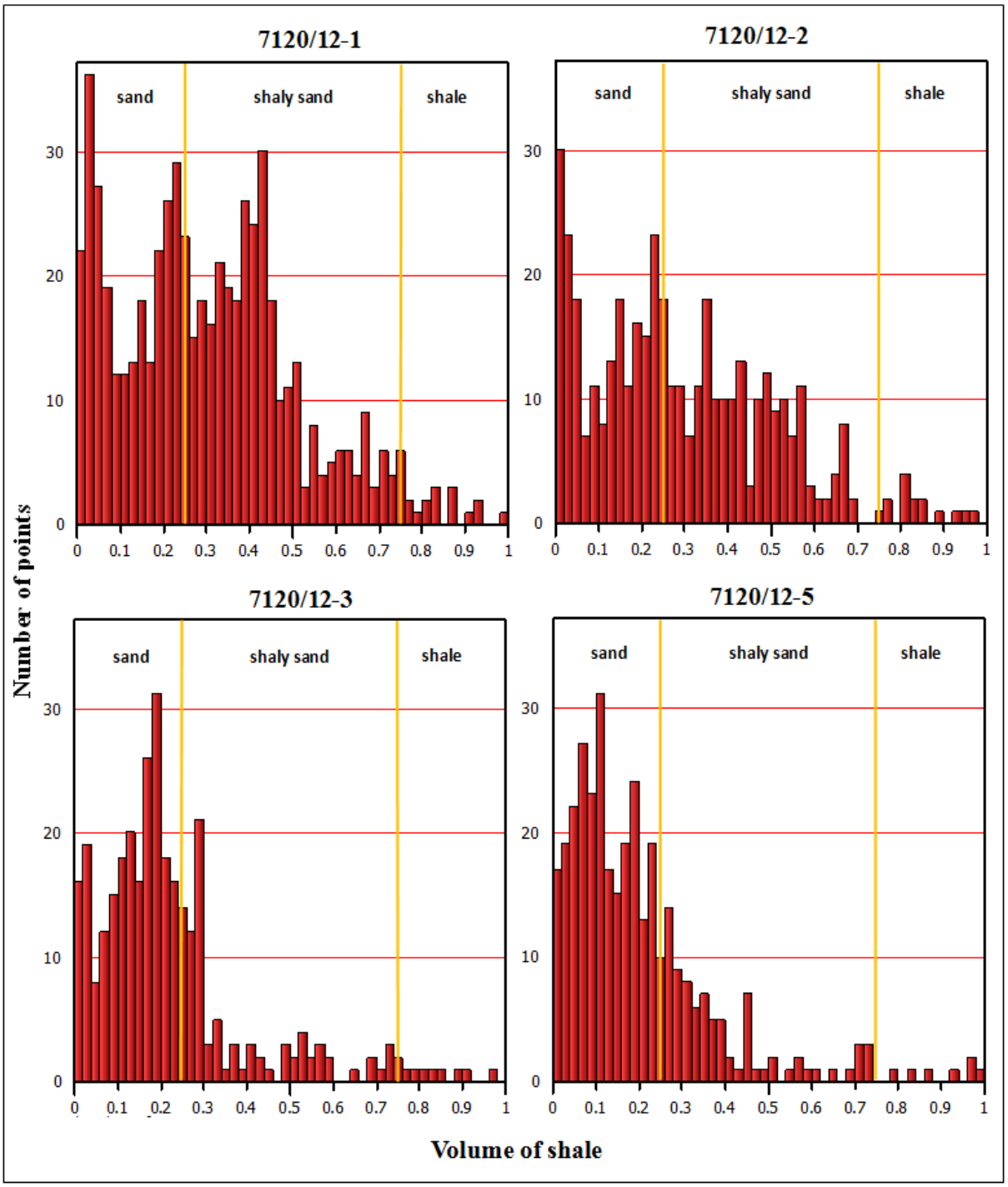

Figure 4.2: Histogram showing volume of shale in Stø Formation.

4.2Net-to-gross estimation

Net-to-gross (N/G) is the useful parameter for estimation of the heterogeneity of sandstone. It is the ratio of the fraction of clean, permeable sand to that of complete reservoir rock including the reservoir sands and impermeable shales (Avseth, 2009). The values of (N/G) range from 0 to 1.0. The net-to-gross ratio reflects the quality of the sandstone as potential reservoirs rocks. The calculated net-to-gross ratio is based on clay content, water saturation and porosity.

The Stø formation shows a good potential reservoir rocks as it has the higher values of net-gross-ratio as compared to other formations present in the Kapp Toscana group.

The Stø Formation has highest value of (N/G=0.92) in the well 7120/12-3 and lowest value (N/G=0.83) in the well 7120/12-2 which is quite good for potential reservoir sandstone. Nordmela Formation has intermediate values of (N/G) ratio ranges from 0.61 to 0.71. Tubåen Formation has highest value of (N/G=0.83) in the well 7120/12-3 while lowest value of (N/G=0.47) in the well 7120/12-2. Snadd Formation shows a moderate potential reservoir rock as it has the lowest values of net-to-gross ratio ranges from 0.27-0.44. The net-to-gross ratios of all the formations of Kapp Toscana Group present in the study area are illustrated in Table 4.1.

Table 4.1: Net-to-gross ratio of all the formations of Kapp Toscana Group in the study area.

Formations	Wells	Gross	Net	Net/Gross
Stø Formation	7120/12-1	105	88.99	**0.85**
	7120/12-2	86	71.83	**0.83**
	7120/12-3	62	56.80	**0.92**
	7120/12-4	**Absent**		
	7120/12-5	65	57.33	**0.88**
Nordmela Formation	7120/12-1	98	69.20	**0.71**
	7120/12-2	174	106.33	**0.61**
	7120/12-3	122	75.38	**0.62**
	7120/12-4	**Absent**		
	7120/12-5	135	87.60	**0.65**
Tubåen Formation	7120/12-1	87	64.44	**0.74**
	7120/12-2	82	38.57	**0.47**
	7120/12-3	53	44.10	**0.83**
	7120/12-4	**Absent**		
	7120/12-5	42	30.55	**0.73**
Fruholmen Formation	7120/12-1	198	86.74	**0.44**
	7120/12-2	120	53.70	**0.45**
	7120/12-3	128	69.49	**0.54**
	7120/12-4	**Absent**		
	7120/12-5	175	91.29	**0.52**
Snadd Formation	7120/12-1	939	293.13	**0.31**
	7120/12-2	573	154.78	**0.27**
	7120/12-3	**Not Penetrated**		
	7120/12-4	50	21.81	**0.44**
	7120/12-5	990	320	**0.32**

4.3 Porosity calculation

Density porosity is calculated from the density log which is the measure of formation bulk density. The neutron porosity logs are the measure of hydrogen concentration in the formation. As gas saturated zones have a very low density and hydrogen index as compared to water. So if the gas zone is present, the log gives an under estimated porosity values. Due to these uncertainties, average porosity is calculated by taking the square-root of average of density porosity and neutron porosity.

The average porosity of all the formations present in the Kapp Toscana Group is illustrated in the Table 4.2. The Stø Formation has maximum average porosity of 20% in the well 7120-12-2 while minimum average porosity of 15% in the well 7120/12-5. The Nordmela Formation has maximum average porosity of 22% which is same in the wells 7120/12-1 and 7120-12-2 while minimum average porosity of 15% in the well 7120/12-5.

The Tubaen Formation has maximum average porosity of 23% in the well 7120-12-2 while minimum average porosity of 15% in the well 7120/12-5. The Fruholmen Formation has maximum average porosity of 20% in the well 7120-12-2 while minimum average porosity of 15% in the well 7120/12-5. The Snadd Formation has maximum average porosity of 35% in the well 7120-12-4 while minimum average porosity of 15 % in the well 7120/12-5.

Table 4.2: Average porosity of all the formations of Kapp Toscana Group encountered in the five studied wells.

Well name	Stø Formation	Normela Formation	Tubåen Formation	Fruholmen Formation	Snadd Formation
7120/12-1	19 %	22 %	21 %	21 %	17 %
7120/12-2	20 %	22 %	23 %	22 %	20 %
7120/12-3	17 %	19 %	18 %	22 %	Not penetrated
7120/12-4	Absent				35 %
7120/12-5	15 %	15 %	15 %	15 %	11 %

4.4 Fluid saturation

Hydrocarbon saturation is estimated from water saturation which is calculated from the true resistivity, shale volume, porosity and temperature gradient. Bottom hole temperature is used to calculate the geothermal gradient in each well (Table 4.3).

Table 4.3: Geothermal gradient in the study area.

Well name	Total depth (m) RKB	Bottom hole temperature (^{o}C)	Geothermal gradient (^{o}C/km)
7120/12-1	3573	65	17.1
7120/12-2	4680	115	22.8
7120/12-3	2523	118	45.2
7120/12-4	2199	51	21.4
7120/12-5	3630	100	26.4

The combination of density and neutron logs are used for the differentiation of the various fluid types. The gas zones are interpreted from crossover of the density and neutron logs. The deep resistivity log is used to determine the extent of hydrocarbon thickness in the reservoir. The saturation has been measured for all the formations of Kapp Toscana Group present in the study area. Three prominent gas saturated zones in the Stø Formation have been identified on the basis of the resistivity and saturation.

In the well 7120/12-3, upper part of Stø Formation displays high resistivity and is gas saturated from 2158 m to 2182.5 m. The gas-water contact occurs at 2182.5 m. and the gas saturation is 80-85% (Fig. 4.3).

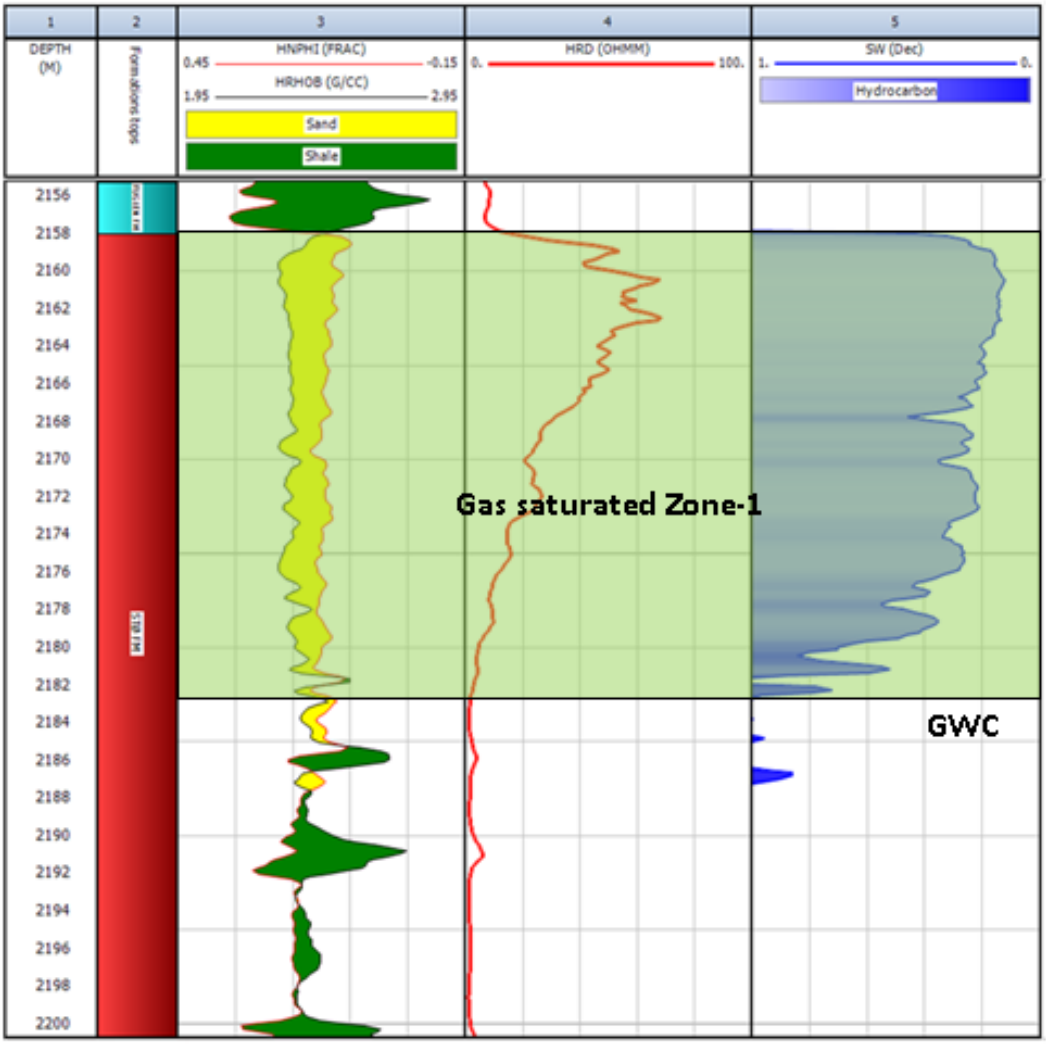

Figure 4.3: Gas saturated zone of Stø Formation in the well 7120/12-3 with neutron density crossover and deep resistivity log response.

In the well 7120/12-2, Stø formation is gas saturated from 1892 m to 1981.5 m in the well 7120/12-2 with gas water contact occurs at 1981.5 m. The gas saturation varies with depth in the formation. The Stø Formation in this well contains two main prominent zones (Fig. 4.4). Gas saturated zone-1 has saturation of 80-85% while gas saturated zone-2 has saturation of 70-90%.

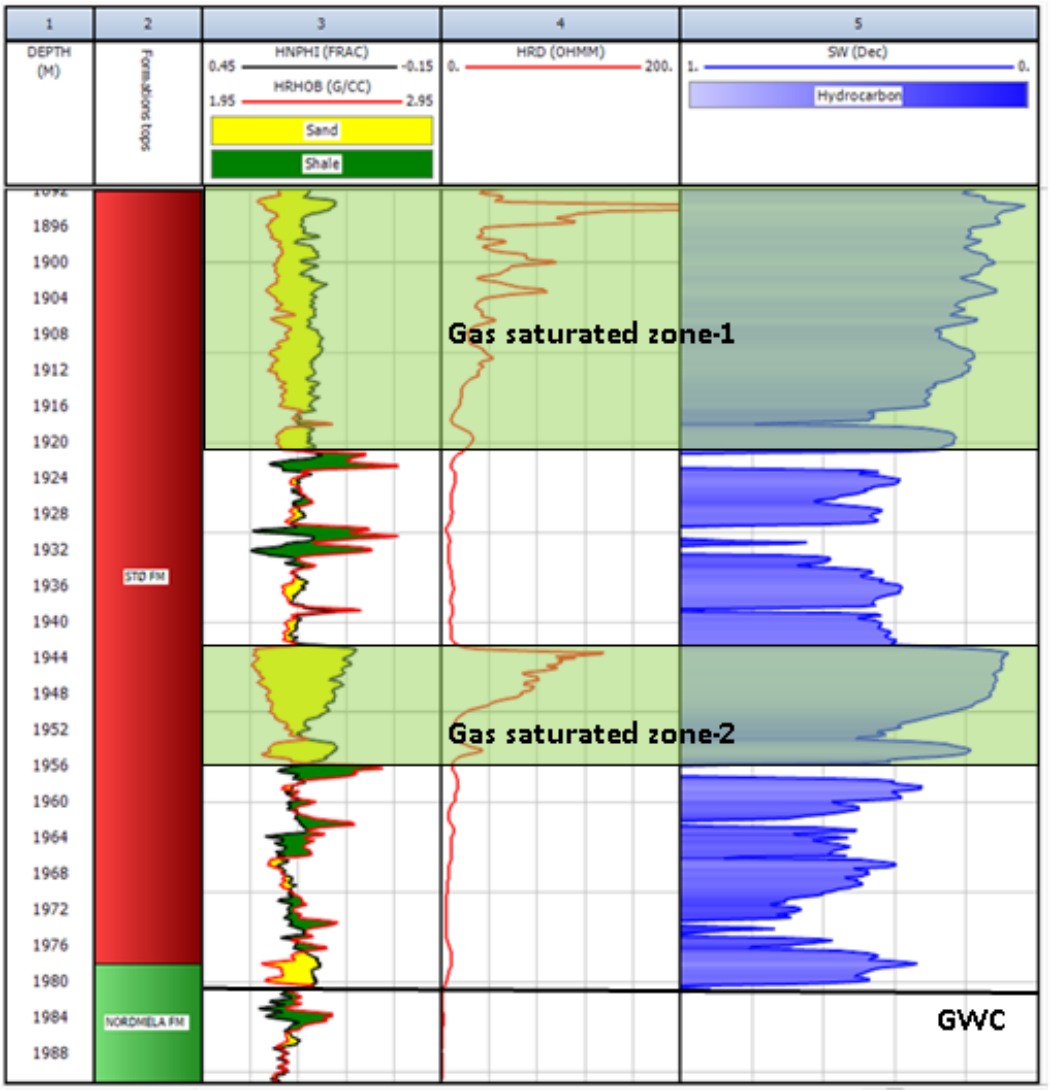

Figure 4.4: Two gas saturated zones of Stø Formation in the well 7120/12-2 with neutron density crossover and deep resistivity log response.

4.5 Discussion

Petrophysical analyses are the initial step in studying the properties of reservoir rock. Moreover, it gives primary input knowledge for characterization of subsurface formations and evaluation of reservoir zones. Wire-line logs are continuous recordings over the rock formations and provide vital information on the properties of rock (Moore et al., 2011). In petrophysical analyses, the initial step is the estimation of shale volume which can be determined by defining the clean sand and shale base line on the gamma ray log. The thickness of Stø Formation in the northern wells (7120/12-3 and 7120/12-5) are 62 and 65 meters respectively while in the southern well (7120/12-1 and 7120/12-2) the thickness increases 105 and 86 meters respectively (Fig. 4.5).

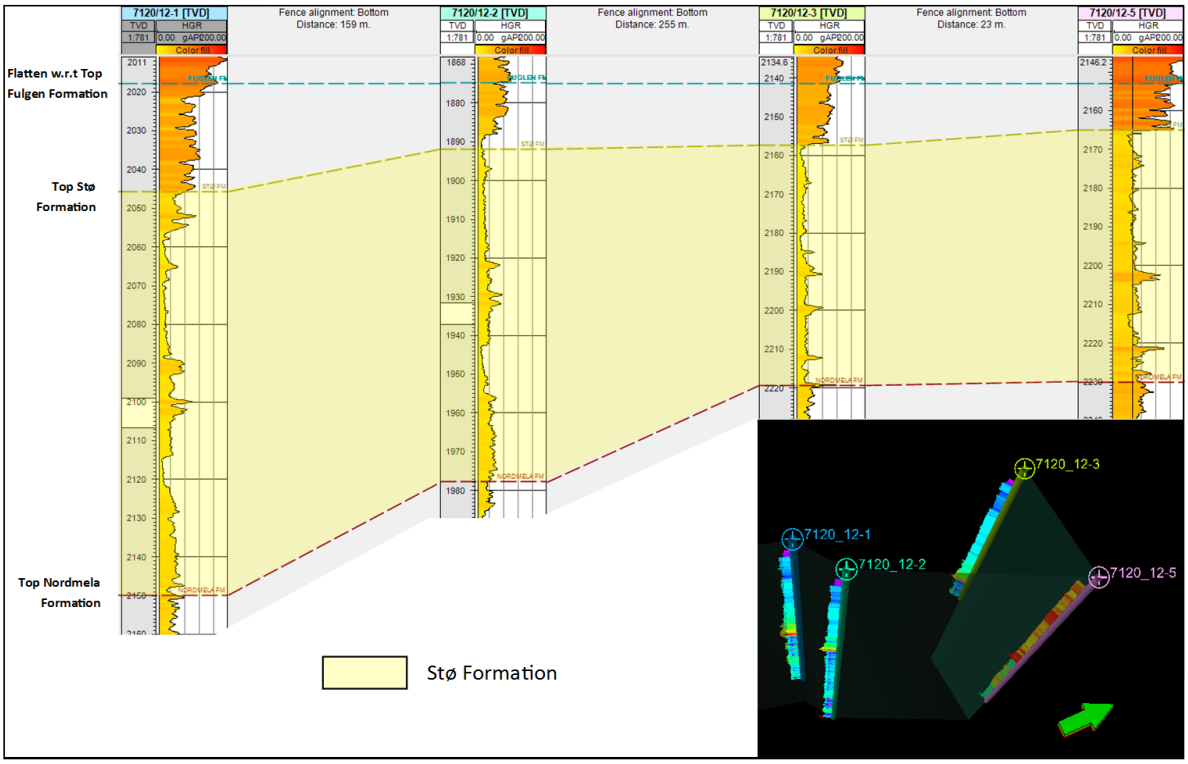

Figure 4.5: Correlation of Stø Formation in the four wells with gamma ray log response. Fencing shows the location of wells.

The results from shale volume calculation of Stø Formation show that the northern wells (7120/12-3 and 7120/12-5) have less amount of shale compared to southern wells (Fig. 4.2). Stø Formation is mostly composed of sandy portion with net-to-gross ratio greater than 0.8 (Selnes et al., 2004). The net-to-gross is the measure of quantity of clean sand in the reservoir rock which reflects the quality of the sandstone. The greater the value of net-to-gross ratio, better the quality of the sandstone (Adepelumi et al., 2011).

The N/G ratio of Stø Formation encountered in four wells of the study area ranges between 0.83 and 0.92. The net-to-gross ratio in the well 7120/12-3 has maximum value of N/G=0.92 while its closest well 7120/12-5 has slightly less N/G=0.88. Comparing the nearest wells (7120/12-1 and 7120/12-2), the Stø Formation shows that the well 7120/12-2 has more clean sandstone as compared to the well 7120/12-1. Table 4.1 shows that Stø Formation has higher net-to-gross ratio as compared to other formation of Kapp Toscana group. Nordmela, Tubaen and Fruholmen Formations have intermediate value of net-to-gross show moderate quality while Snadd Formation has the lowest value of net-to-gross depicting poor reservoir quality.

The higher value of N/G ratio shows that Stø Formation is composed of clean, medium to fine grained sandstones deposited in near shore marine environment. The thin Shale interbeds present in the Stø Formation are characteristic of transgressive marine events. The sandstones of Stø Formation are of good reservoir quality with a lateral continuity than the underlying Nordmela Formation (Stewart et al., 1995).

On the basis of neutron-density cross-over and high resistivity, the hydrocarbon zones have been identified in the Stø Formation. The upper 24.5 meter thick sequence of Stø Formation in the well 7120/12-3 represents hydrocarbon zone with gas saturation up to 85% (Fig. 4.3). In the well 7120/12-2, two gas saturated zones have been identified. Gas saturated zone 1 is

28 meter thick with low gamma ray representing clean sandstone. The deep resistivity is higher up to 200 ohm-meter with gas saturation up to 80%. Gas saturated zone 2 has less cross-over thickness of 12 meter as compared to gas saturated zone-1. Moreover, deep resistivity up to 140 ohm-meters has been observed in this zone. The middle part between the two gas saturated zones and the lower part are showing the intercalation of shales stringers. Theses intercalations reduce the reservoir quality and N/G ratio. The resistivity in these portions is lower with gas saturation up to 50% (Fig. 4.4).

Chapter 5
Rock Physics Diagnostics of reservoir rocks

Rock Physics Diagnostics of reservoir rocks

Rock physics provides a link between elastic parameters and reservoir properties. The elastic properties such as velocity, density, impedance and Vp/Vs ratio are used in reservoir imaging quality and characterization. These properties are related to the reservoir properties such as porosity, volume of shale and water saturation. Rock physics is a very important tool in efficient interpretation and provide a relationship between lithology, fluid content, and depositional environment of the reservoir rocks. Rock physics modeling can be utilized to build a template for efficient characterization of the reservoir rocks (Chi and Han, 2009). The rock physics templates (RPT's) are specific for a basin and depend on local geologic factors. Rock physics models have some geologic limitations such as lithology, mineralogy, depth of burial, pressure, and temperature. These factors have to be considered when generating RPT's for a given basin (Avseth et al., 2010).

In the study area, rock physics analysis is carried out to determine lithology and fluid discrimination by employing different rock physics templates. The Stø Formation is analyzed in four wells in the study area by utilizing different rock physics templates such as porosity versus Vp, AI versus Vp/Vs, Lambda-rho versus Mu-rho and Vp versus Vs. The Vs is present in the well 7120/12-5 so the whole Kapp Toscana Group including the Stø, Nordmela, Tubåen, Fruholmen and Snadd Formations are analyzed in that well.

5.1 Results

5.1.1 Porosity versus Vp

5.1.1.1 Han's model

The Vp versus porosity cross plot of Stø Formation from four wells is plotted on Han's model. The data points of Stø Formation with cutoff value of 0.4 are taken and then plotted on the Han's clay lines from 0 to 40%. Hans's minimum line shows clean sands and with increasing clay contents shows dirtier sands.

The Stø Formation in the well 7120/12-1 falls between 10-30% Han's lines while in the well 7120/12-2 falls between 20-40% Han's lines. Both the wells have similar porosity between 17 to 25%. The Vp is higher in the well 7120/12-1 ranges from 3.75 to 4.25 km/s which decreases to 3.25 to 3.6 km/s in the well 7120/12-2.The Stø Formation in the well 7120/12-3 falls between 10-40% Han's lines while in the well 7120/12-5 falls between 10-30% Han's lines (Fig. 5.1).

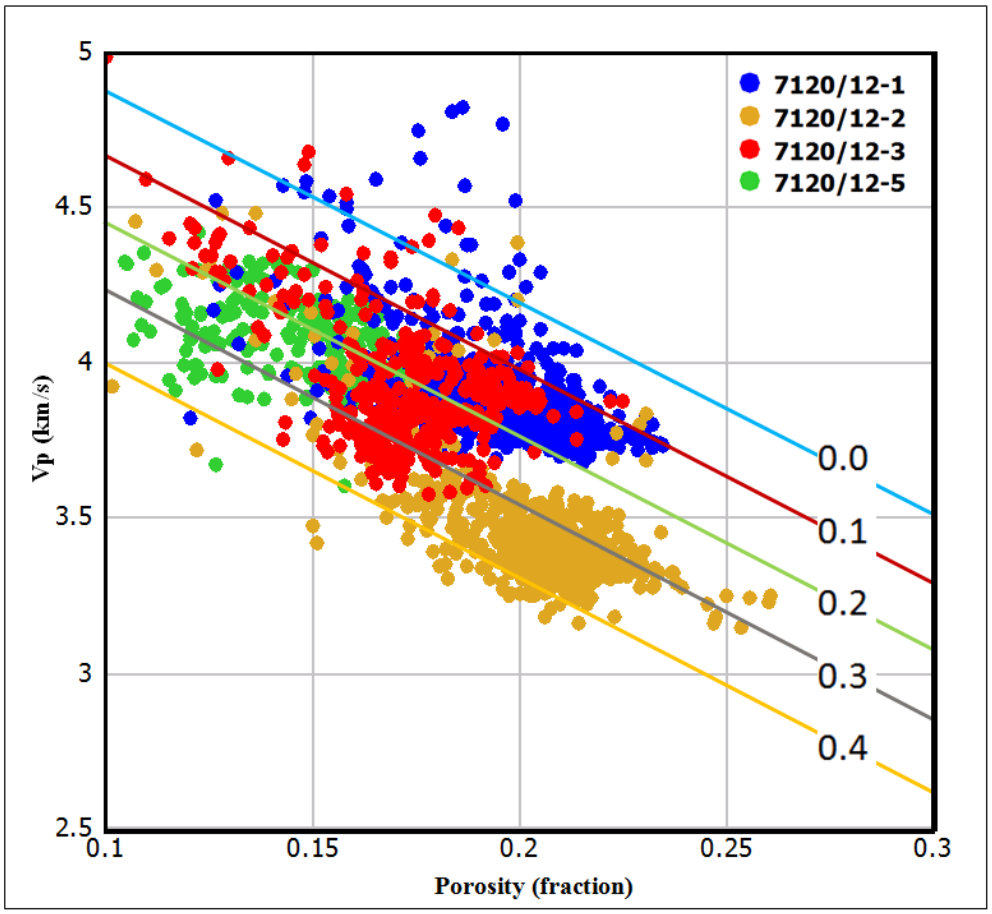

Figure 5.1: Vp versus porosity cross plot of Stø Formation in four wells compared to Han's clay fraction lines.

In the well 7120/12-1, the data points of clay volume 0-10% falls between 0-20% Han's lines. With increasing clay volume the data points from 10-20% and 20-30% falls between 10-30% Han's lines. In the well 7120/12-2, the data points of clay volume from 0-30% falls between 30-40% Han's lines. The data points from 30-40% are dispersed and occur between 10-40% Han's lines (Fig. 5.2).

In the well 7120/12-3, the data point of clay volume 0-20% falls between 10-40% Han's lines. The clay volume from 20-30% and 30-40% falls between 10-30% Han's lines. In the well 7120/12-5, the data points of clay volume 0-10% fall between 10-20% Han's lines. The clay volume 10-30% and 30-40% falls between 20-30% Han's lines while 30-40% falls between 20-40% Han's lines (Fig. 5.2).

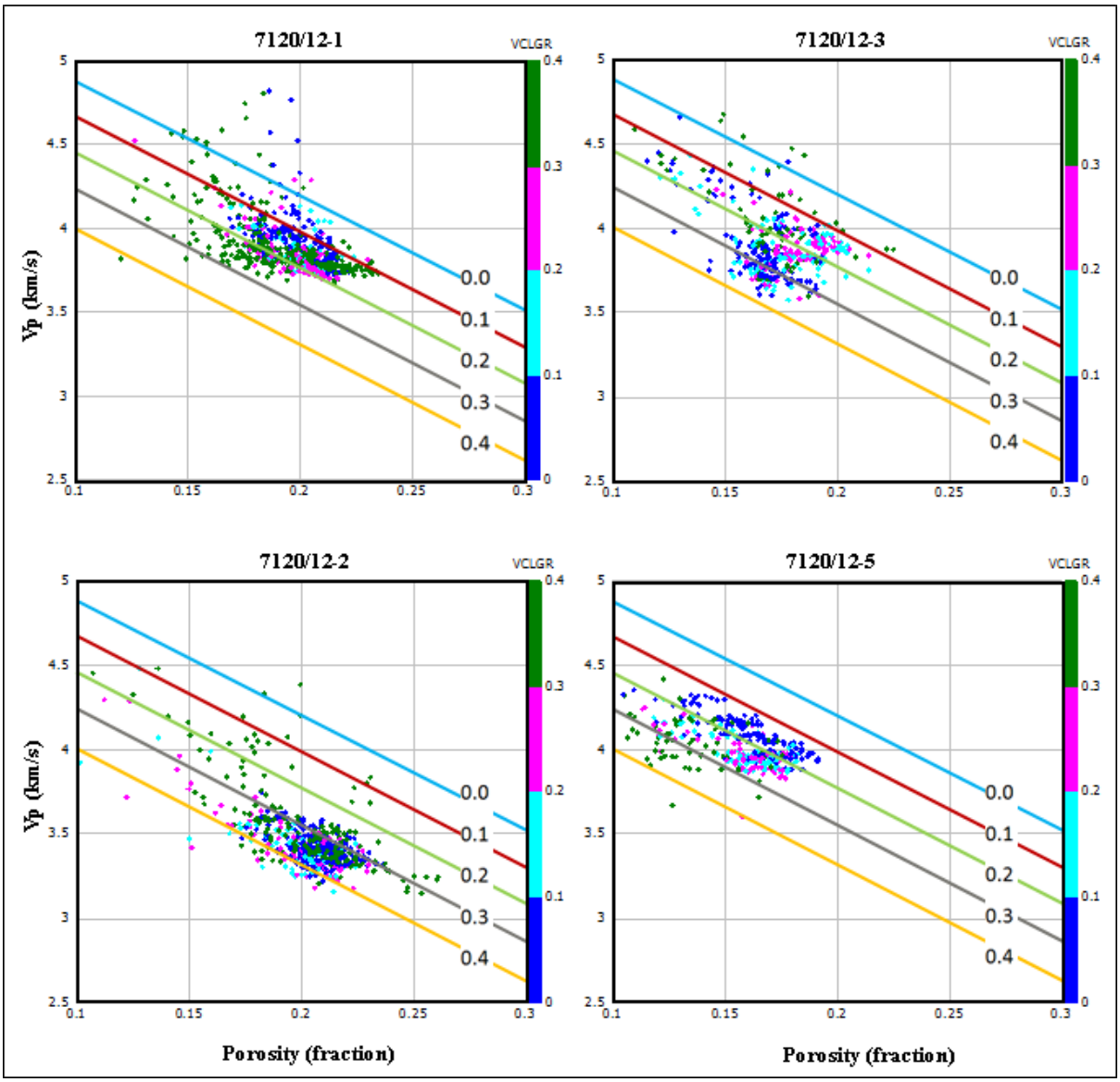

Figure 5.2: Vp versus porosity cross plot of Stø Formation in four wells compared to Han's clay fraction lines in four wells.

5.1.1.2 Cement models

Three cement models are used in the crossplot of porosity versus Vp to study the cement distribution in the studied reservoir sandstones. Contact and constant cement lines are taken from Avseth et al. (2010) while friable sand model is taken from Dvorkin and Nur (1996). The cement fraction is taken as 2% in the constant cement line.

The P-wave velocity of Stø Formation is plotted against average porosity which shows varying amount of cement distribution in different wells. The sand data points with cutoff value of 0.25 fraction of clay volume are taken to study the cement models.

In the well 7120/12-1, Stø Formation occurs between constant and contact cement lines. The porosity ranges between 17 to 22% while Vp ranges between 3.7 to 4.2 km/s. The cement volume increases with depth within the Stø Formation. In the well 7120/12-2, Stø Formation occurs between friable sand and constant cement models. The porosity ranges between 17 to 23% while Vp ranges between 3.2 to 3.7 km/s.

In the well 7120/12-3, the Stø Formation falls approximately on the constant cement line. The cement volume increases with depth. The shallow part of Stø Formation occurs between the friable sand and constant cement lines while deeper part occurs between the constant and contact cement lines. This implies an increase in cement volume with increase in the depth. In the well 7120/12-5, the Stø Formation occurs on constant cement line with increasing cement volume by depth.

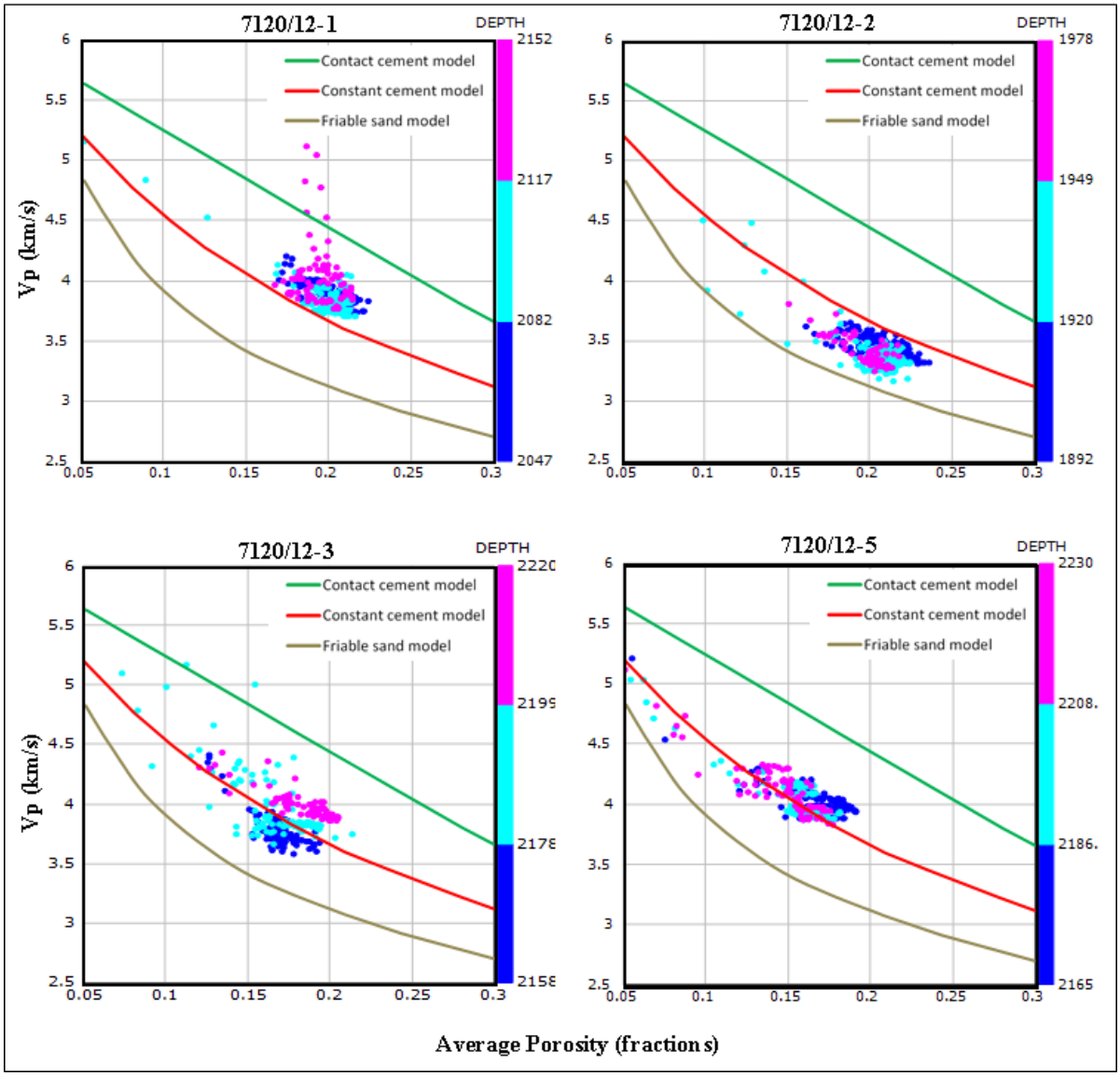

Figure 5.3: Vp versus average porosity cross plot of Stø Formation from four wells showing cement models with depth.

5.1.2 AI versus Vp/Vs

Acoustic impedance is cross plotted against Vp/Vs in Stø Formation for four wells. The Stø Formation in the well 7120/12-1 have AI mainly ranges between 8500 to 10000 m/s*g/cc while Vp/Vs ratio ranges between 1.65 and 1.75. In the well 7120/12-2, the AI has decreased and ranges between 7000 to 9000 m/s*g/cc. While Vp/Vs ratio has increased as compared to the well 7120/12-1 ranges between 1.75 and 1.87.

The cross plot also gives information about porosity, shaliness and cement volume. The arrow 1 shows the trend of increasing porosity, arrow 2 shows trend of increasing shaliness and arrow 3 shows the trend of increasing cement volume (Avseth et al., 2005) (Fig. 5.4). The well 7120/12-2 shows maximum porosity and minimum cementation while well 7120/12-5 shows minimum porosity and maximum cementation.

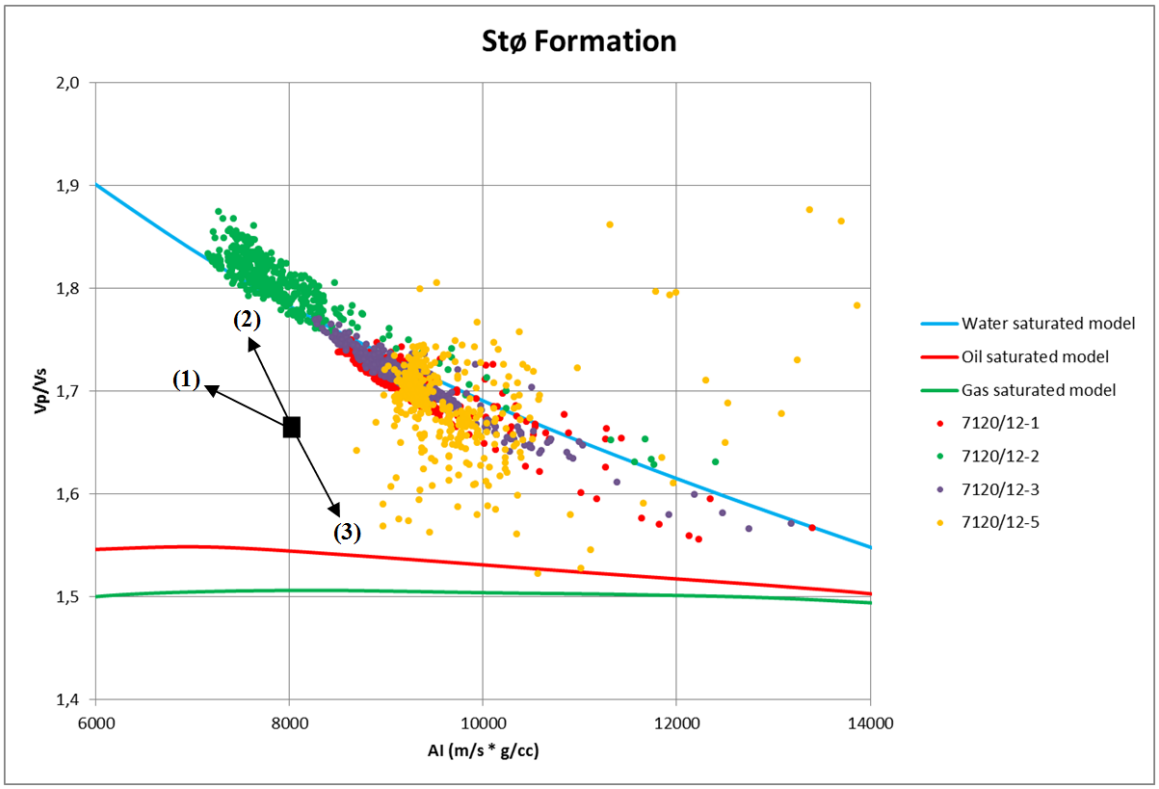

Figure 5.4: AI versus Vp/Vs of Stø Formation in four wells.

Acoustic impedance is also cross plotted against Vp/Vs with saturation in Stø Formation for four wells. The wells 7120/12-1 and 7120/12-5 show 100% water saturation. The well 7120/12-2 shows increasing gas saturation with decrease in acoustic impedance and Vp/Vs ratio. The completely water saturated part have higher acoustic impedance. The well 7120/12-3 also shows gas saturation with decrease in acoustic impedance.

The presence of gas saturation in the wells 7120/12-2 and 7120/12-3 exist on the water saturated line which is due to the absence of measured Vs. The Vs for these wells are estimated from the Castagna et al. (1993) empirical relation.

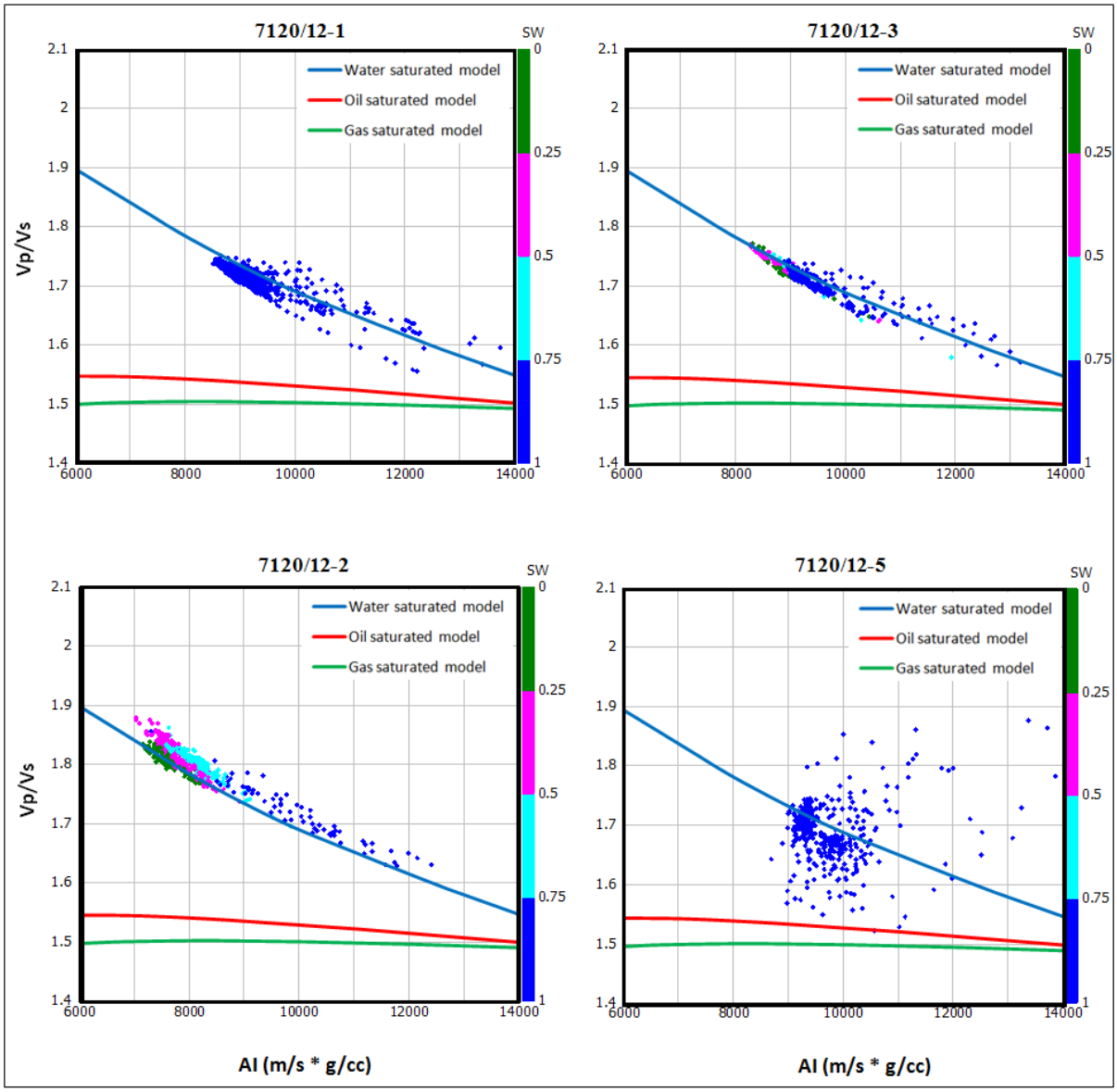

Figure 5.5: Acoustic impedance versus Vp/Vs of Stø Formation in four wells with respect to saturation.

5.1.3 Lambda-Rho versus Mu-Rho

Lambda-Rho versus Mu-Rho cross plot of Stø Formation is plotted for four wells. The data points from four wells showing that Stø formation is mainly sandstone. The response of Lambda-Rho and Mu-Rho in the well 7120/12-5 is giving the actual values because measured Vs is present in this well. The rest of the wells show a linear behavior because Vs is estimated by Castagna et al. (1993) empirical relation. The well 7120/12-2 has lower values of Lambda-Rho and Mu-Rho as compared to other wells (Fig. 5.6).

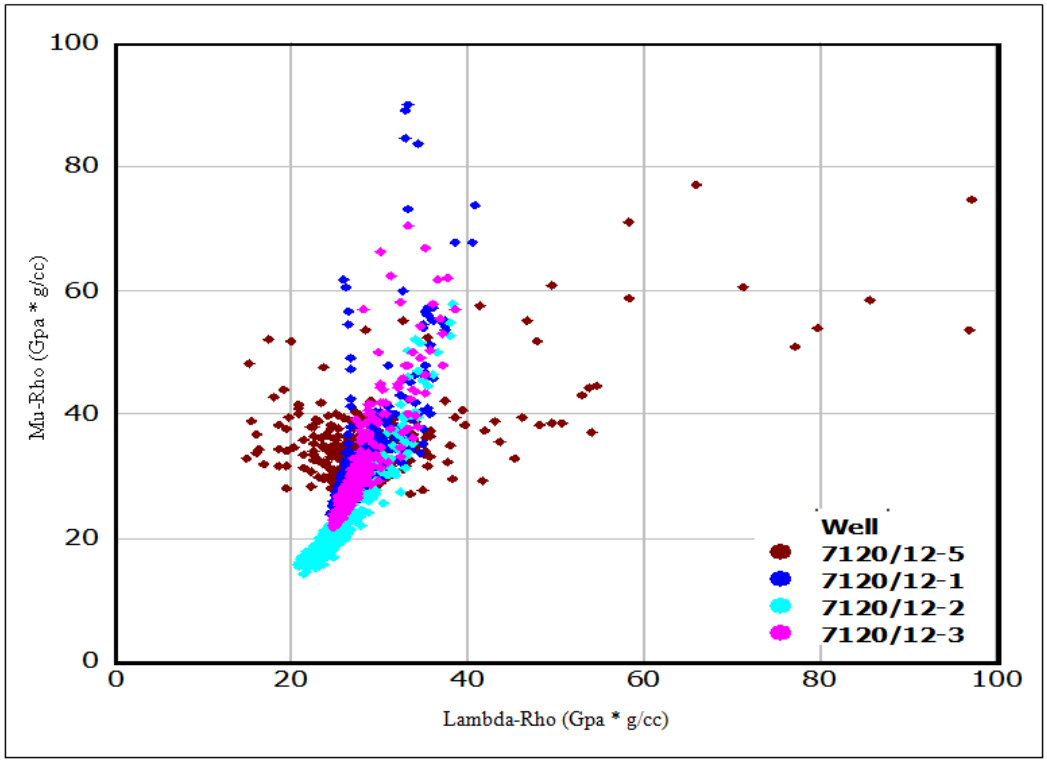

Figure 5.6: Lambda-Rho versus Mu-Rho cross plot of Stø Formation in four wells.

The wells 7120/12-2 and 7120/12-3 show a link between shale volume and the saturation of gas. The gas saturation increases with decrease in shale volume (Figs. 5.7 and 5.8). The gas saturated portion has lower Lambda-Rho and Mu-Rho as compared to the completely water saturated portion in Stø Formation which has higher Lambda-Rho and Mu-Rho.

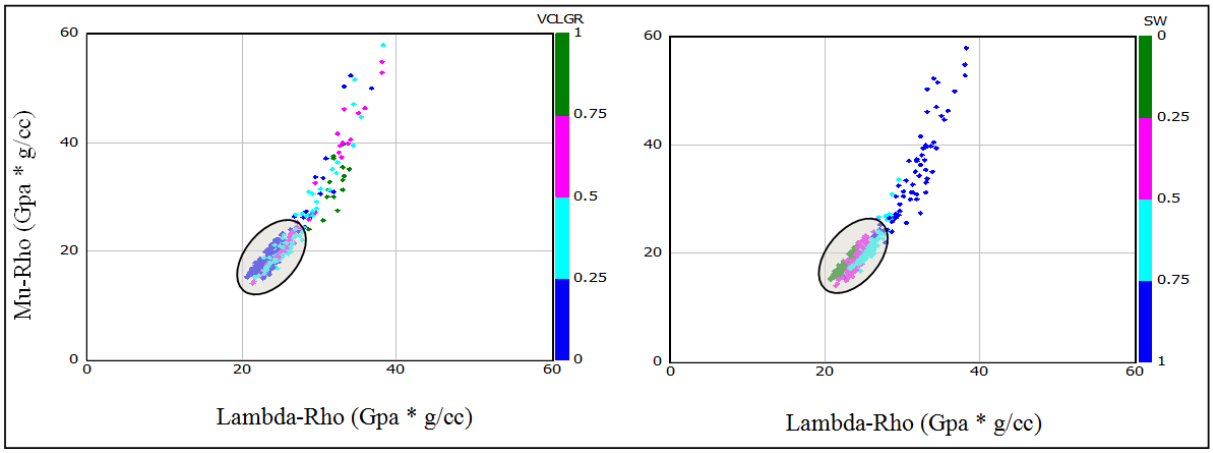

Figure 5.7: Lambda-Rho versus Mu-Rho cross plot of Stø Formation in well 7120/12-2 showing volume of shale and saturation.

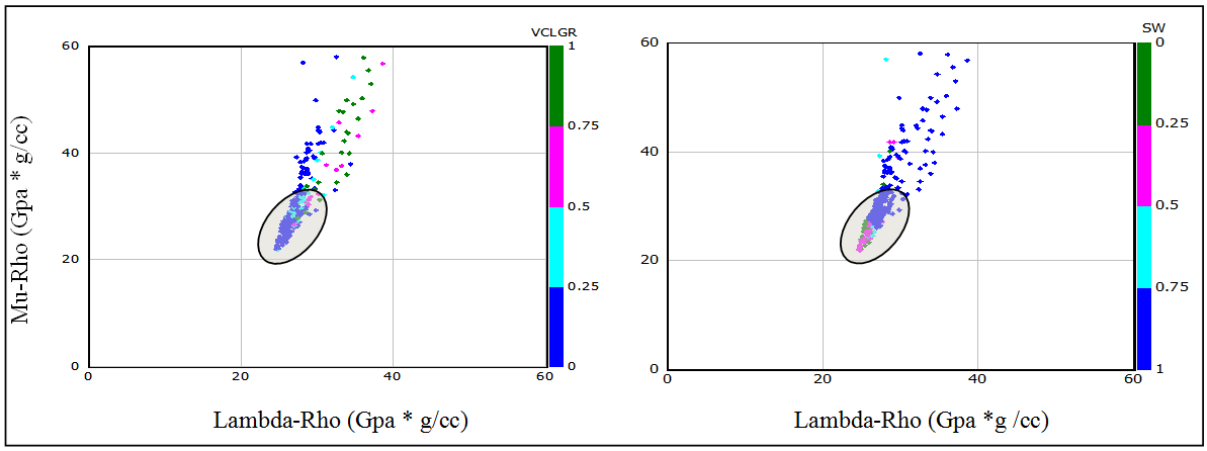

Figure 5.8: Lambda-Rho versus Mu-Rho cross plot of Stø Formation in well 7120/12-3 showing volume of shale and saturation.

5.1.4 Rock physics Diagnostics of Kapp Toscana Group

As Vs is present in the well 7120/12-5, so Kapp Toscana Group in this well is diagnosed by using the rock physics templates.

Cement models of whole Kapp Toscana Group is plotted in the Vp versus porosity cross plot (Fig.5.9). The Stø, Nordmela and Tubåen Formations occur on the constant cement model. Fruholmen Formation from shallow depth occur between constant and contact cement line with higher porosity and Vp while deeper part occurs between friable sand and constant cement model with lower porosity and Vp. The Snadd Formation occurs on the friable sand model with shallow part having higher porosity and lower Vp while the deeper part having lower porosity and higher Vp.

Fluid models are plotted in AI versus Vp/Vs crossplot color coded with shale volume for the Kapp Toscana Group (Fig. 5.10). The whole Kapp Toscana Group is water saturated. The Stø Formation is mostly composed of sand points occur below the water saturated line. The quantity of shaly sand is less and dispersed around the water saturated line. The Nordmela Formation mostly composed of both sand and shaly sand fall around the water saturated line. The quantity of shale is very less in this formation. The Fruholmen Formation is mostly composed of shaly sand occurs above the water saturated line. The Snaad Formation is mostly composed of shaly sand and shale.

Lambda-Rho versus Mu-Rho cross plot shows that Stø and Tubåen Formations are composed both of shaly sand. The quantity of shaly sand increases in Nordmela and Fruholmen Formations. The Snadd Formation is mostly composed of shaly sand with dominant amount of shale as well (Fig. 5.11)

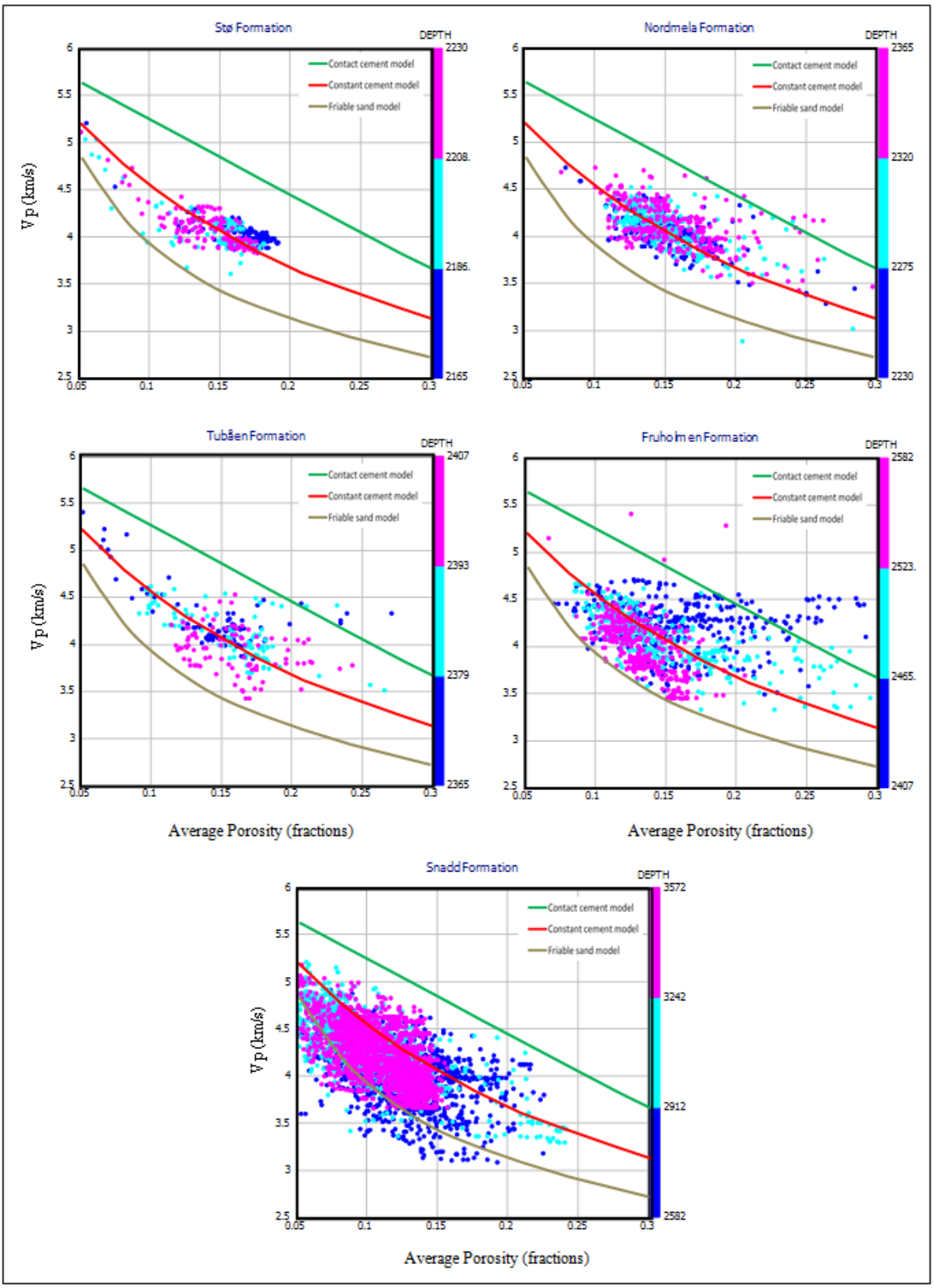

Figure 5.9: Vp versus porosity cross plot of five formations of Kapp Toscana Group in the well 7120/12-5 with respect to depth.

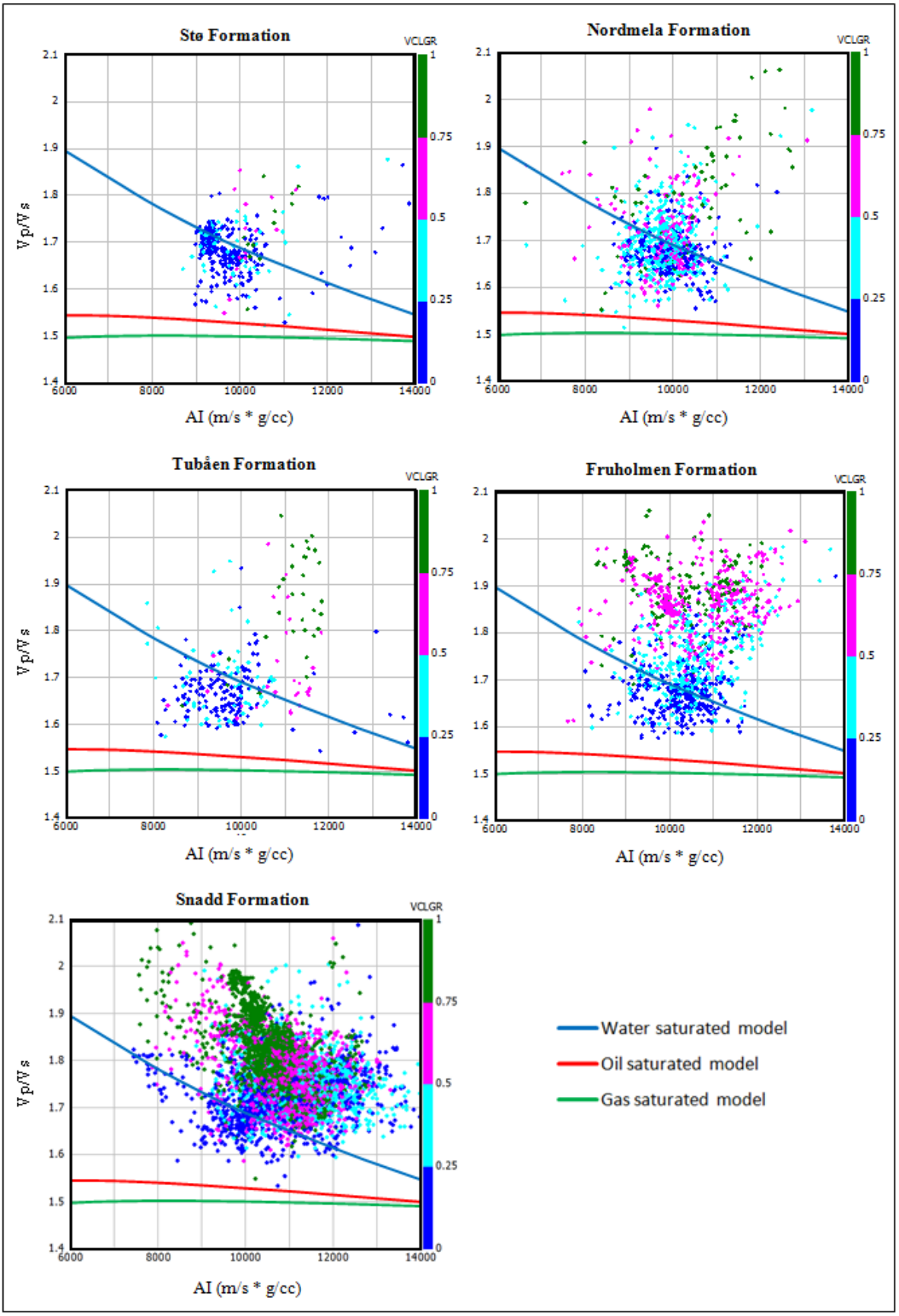

Figure 5.10: AI versus Vp/Vs cross plot of five formations of Kapp Toscana Group in the well 7120/12-5 with respect to volume of shale.

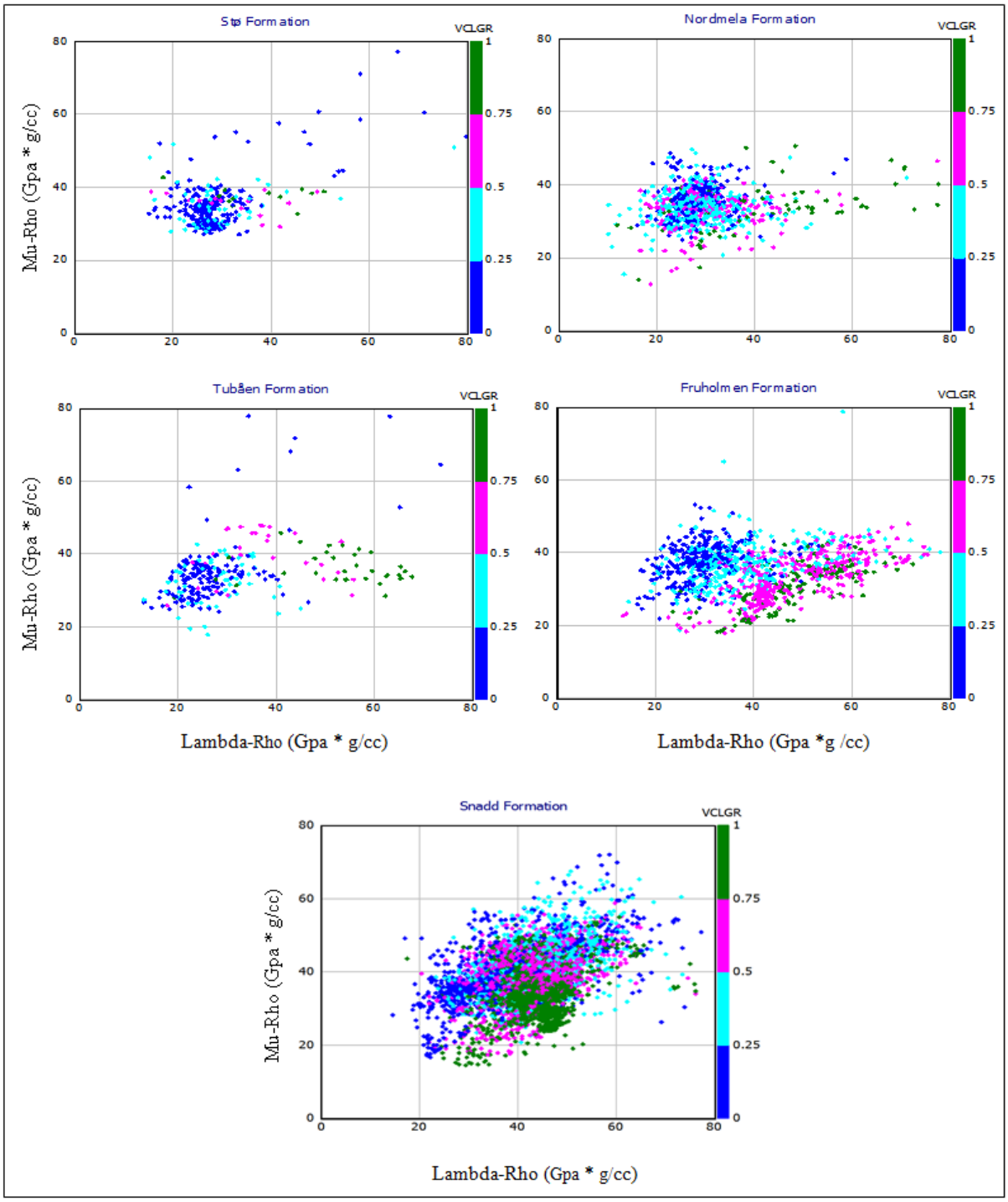

Figure 5.11: Lambda-Rho versus Mu-Rho cross plot of five formations of Kapp Toscana Group in the well 7120/12-5 with respect to volume of shale.

5.2 Discussion

5.2.1 Porosity versus Vp

The Stø Formation has different cement distribution in the four wells. The Stø Formation is compared in two closest wells (7120/12-1 and 7120/12-2) which have similar porosity but different P-wave velocity (Fig. 5.12). In the well 7120/12-1, Stø Formation is water saturated and occurs between contact and constant cement model. The Vp values are higher in this well

which ranges from 3.75 to 4.20 km/s. The Stø Formation in the well 7120/12-2 is gas saturated and occurs between friable and constant cement models. Vp is relatively low which ranges from 3.25 to 3.65 km/s.

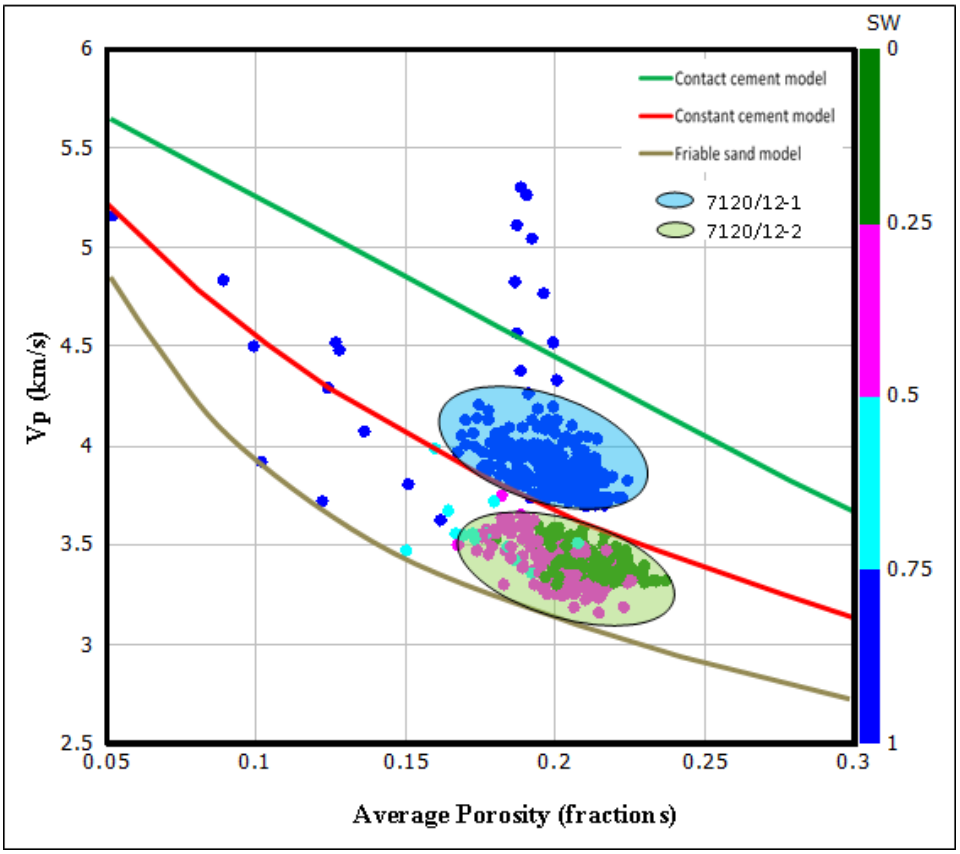

Figure 5.12: Vp versus average porosity cross plot of Stø Formation from well 7120/12-1 and 7120/12-2 showing saturation and cement models.

The Stø Formation in the well 7120/12-3 is almost at same depth level to the well 7120/12-5 showing same overburden stress. In the well 7120/12-3, Stø Formation contains both the water saturated and gas saturated parts, whereas it is completely water saturated in well 7120/12-5 (Fig. 5.13). In the well 7120/12-3, water saturated part is from upper part and occurs between friable sand and constant cement models. The Vp in the gas saturated zone is low which ranges from 3.6 to 3.8 km/s. Water saturated zone is from deeper part of the formation and occurs between the constant cement line and contact cement line. The Vp is relatively higher and ranges from 3.8 to 4.3 km/s. The water saturated well 7120/12-5 occurs on constant cement line with relatively higher velocity and ranges from 4.0 to 4.5 km/s.

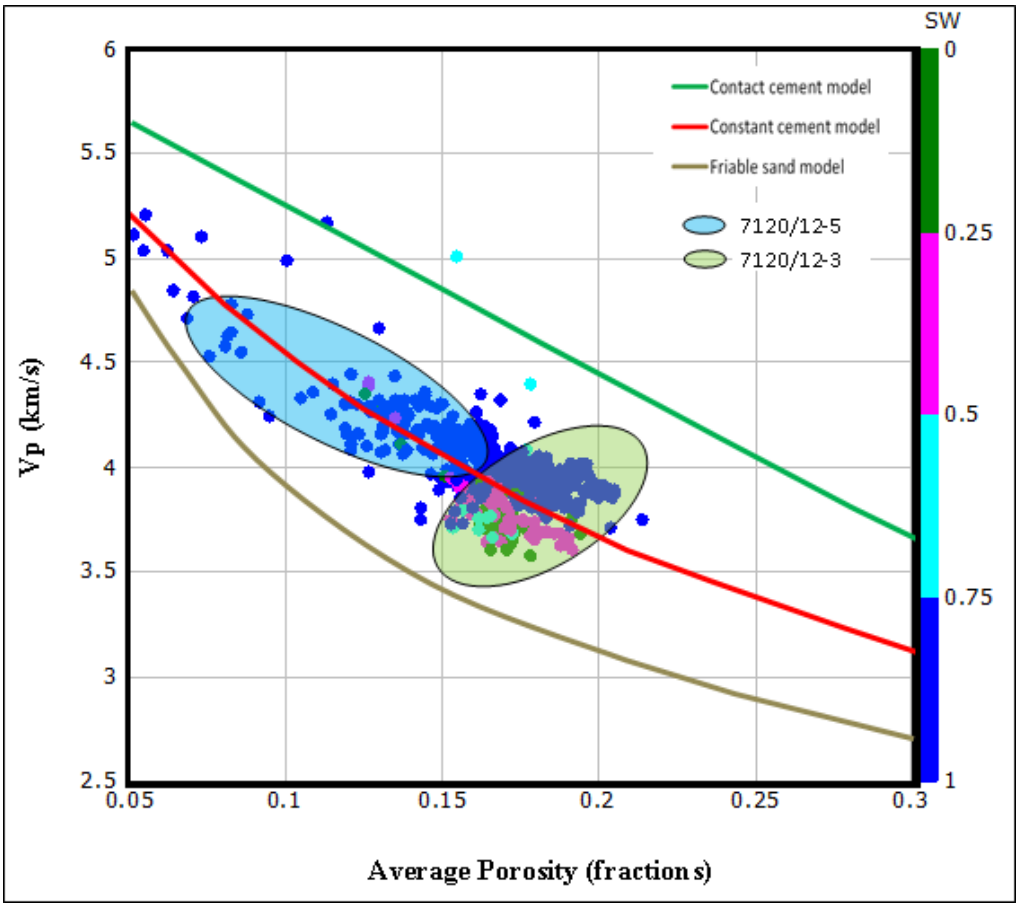

Figure 5.13: Vp versus average porosity cross plot of Stø Formation from well 7120/12-3 and 7120/12-5 showing saturation and cement models.

5.2.2 AI versus Vp/Vs

The cross plot of acoustic impedance versus Vp/Vs ratio help to differentiate different fluids and gives additional information regarding porosity, cement volume and gas saturation. Previous petrophysical analyses and porosity versus velocity cross plot shows the existence of gas saturated zone in two wells (7120/12-2 and 7120/12-3) but this cross plot shows that Stø Formation is water saturated in all wells. There is some limitation because Vs employed in this cross-plot is derived from Castagna et al. (1993) empirical relation. This cross plot shows that Stø Formation has maximum porosity in the well 7120/12-2 while the minimum porosity occurs in the well 7120/12-5 which justifies previously calculated porosity by petrophysical analysis. Regarding cementation, the Stø Formation in the wells 7120/12-5 and 7120/12-1 are more cemented as compared to other two wells 7120/12-2 and 7120/12-3 (Fig. 5.4).

5.2.3 Lambda-Rho versus Mu-Rho

The cross plot of Lambda-Rho versus Mu-Rho gives an advantage to separate sand, shale, limestone and coal. Sandstone can further be differentiated in to gas sands, shaly sand and cemented sandstone. The wells 7120/12-2 and 7120/12-3 show gas saturation with decreasing Lambda-Rho. The saturation of gas increases with decrease in volume of shale depicting less cementation and fine sandstone (Figs. 5.7 and 5.8).

5.2.4 Rock physics Diagnostics of Kapp Toscana Group

Measured Vs is present in only one well 7120/12-5 which is analyzed for all the formations of Kapp Toscana Group in this well. All the Kapp Toscana Group including Stø, Nordmela, Tubåen, Fruholmen and Snadd Formations in this well are water saturated (Fig. 5.10). The porosity in Stø, Nordmela, Tubåen Formations have similar range of porosity variation and occur on the constant cement line (Fig. 5.9). While in Fruholmen Formation, the porosity variation is more as the shallow part of the formation has greater porosity and is more cemented than the deeper part which is less cemented, poorly sorted and occur on the friable sand model. The Snadd Formation occurs on friable sand line and has minimum porosity as compared with the other formation of Kapp Toscana Group (Fig. 5.9). The reduction of porosity in Snadd Formation is due to poor sorting and the deposition of fine material in the pore spaces.

Chapter 6
AVO Modeling

AVO Modeling

AVO modeling has been done on Stø Formation in two wells (7120/12-3 and 7120/12-5). The main purpose is to observe the influence of gas saturation on the rock properties such as density, Vp, Vs and Poisson's ratio. The main input parameters for the AVO modeling are the well logs including Vp, Vs and density logs. Measured Vs is available for the well 7120/12-5 while for the second well 7120/12-3, Vs is derived from Castagna et al. (1993) empirical relation. The porosity and water saturation is calculated by using bulk density and deep resistivity logs respectively. Moreover, fluid replacement is carried out for five gas saturation scenarios. Synthetic seismograms are generated for these scenarios to analyze the difference in rock properties. Figure 6.1 shows a Gamma ray, density, Vp, Vs, deep resistivity and Poisson's ratio logs response for the cap and reservoir rocks in the well 7120/12-3.

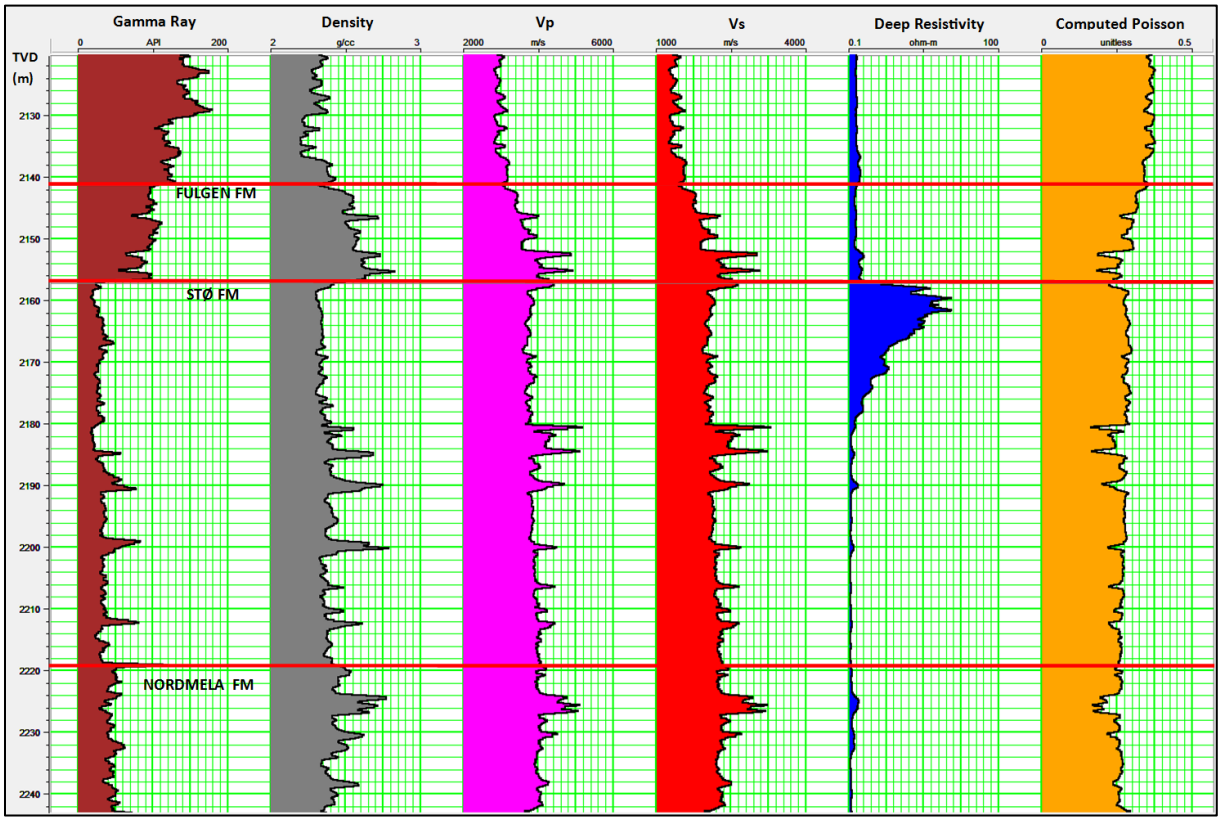

Figure 6.1: Gamma ray, density, Vp, Vs, deep resistivity and Poisson's ratio logs response in the well 7120/12-3.

6.1 Results

6.1.1 Fluid replacement modeling

The fluid replacement modeling has been carried out in Stø Formation using two wells 7120/12-3 and 7120/12-5. Both the wells have been analyzed at five different fluid replacement scenarios (i.e. 100% water, 10% gas, 50% gas, 90% gas and 100% gas) which affected the rock properties including the density, Vp, Vs and Poisson's ratio. The replacement at 90% and 100% gas saturation levels have been performed to check the minor changes in rock properties (Figs. 6.2a and 6.3a).

Table 6.1 shows the changes in rock properties from top of the reservoir at five different fluid scenarios for the well 7120/12-3. The introduction of 10% gas in the fully water saturated rocks decrease the Vp significantly from 4433 m/s to 4358 m/s. Vp increases gradually with an increase in gas saturation from 10% to 50%, 90% and 100%. The density decreases while Vs increases with increase in gas saturation. Similar behavior was observed for Poisson's ratio for different gas saturation levels. Poisson's ratio decreases from 0.242 to 0.227 with the introduction of 10% gas in fully water saturated rock. The introduction of more gas does not has any prominent effect on Poisson's ratio.

Table 6.1: Changes in rock properties from top of the reservoir at five different fluid saturations in the well 7120/12-3.

Parameters	Density (g/cc)	Vp (m/s)	Vs (m/s)	Poisson's ratio
100% Water	2.48	4433	2585	0.24241
10% Gas	2.47	4358	2589	0.22722
50% Gas	2.44	4374	2606	0.22476
90% Gas	2.41	4402	2624	0.22443
100% Gas	2.40	4410	2628	0.22439

Table 6.2 shows the changes in rock properties from the top of the reservoir at five different fluid scenarios for the well 7120/12-5. In this well, Vp also decreases significantly from 4064 m/s to 3902 m/s by introducing 10% gas in the fully water saturated rocks. Vp increases gradually with increase in gas saturation. The density decreases while Vs increases with increasing gas saturation. The change in Poisson's ratio is more prominent as it decreases from 0.242 to 0.227 with the introduction of 10% gas in fully water saturated rock.

Table 6.2: Changes in rock properties from top of the reservoir at five different fluid saturations in the well 7120/12-5.

Parameters	Density (g/cc)	Vp (m/s)	Vs (m/s)	Poisson's ratio
100% Water	2.45	4064	2309	0.26168
10% Gas	2.44	3902	2314	0.22867
50% Gas	2.40	3938	2335	0.22864
90% Gas	2.35	3975	2357	0.22864
100% Gas	2.34	3984	2363	0.22863

A Ricker wavelet of wavelength 200 ms with a sampling rate of 2 ms and linear phase with a dominant frequency of 45 Hz has been used to generate the synthetic seismogram. Furthermore, Zoeppritz equations have been used to generate synthetic seismogram up to 45 degree angle gather. They have been generated for all five fluid replacement situations for the wells 7120/12-3 and 7120/12-5 (Figs. 6.2b and 6.3b).

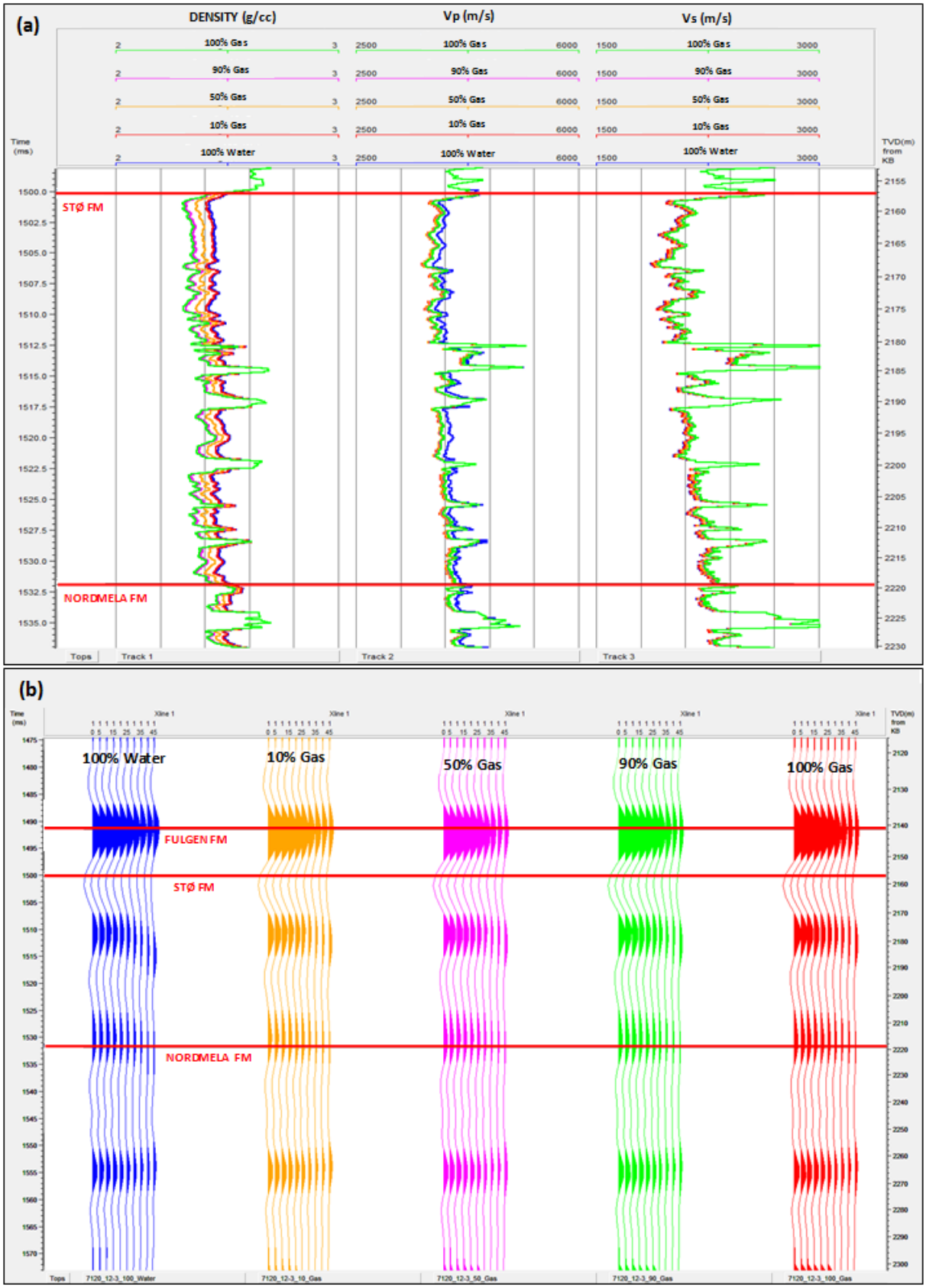

Figure 6.2: (a) Density, Vp and Vs logs response with (b) synthetic seismograms in the well 7120/12-3 at five different fluid saturations.

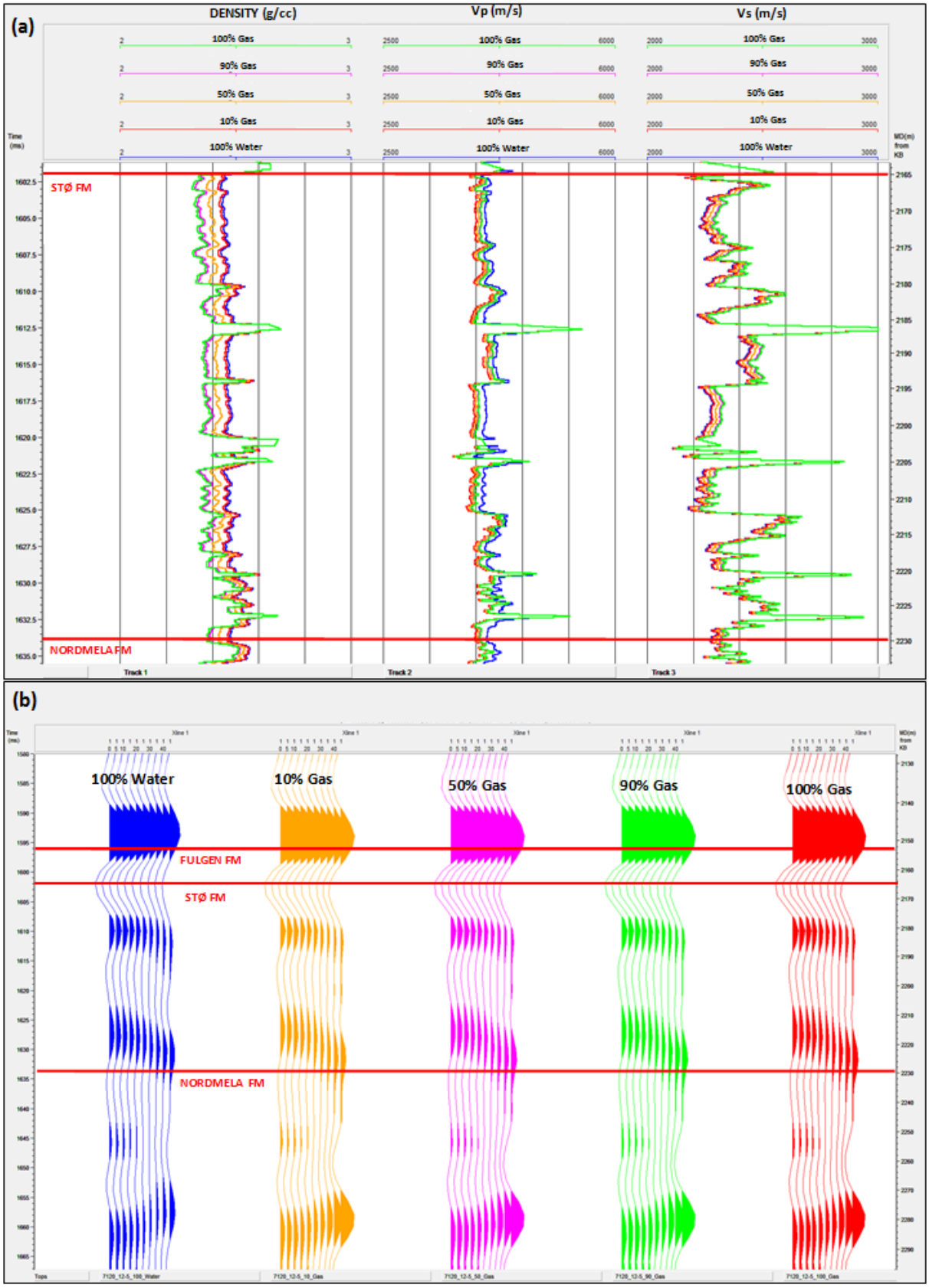

Figure 6.3: (a) Density, Vp and Vs logs response and (b) synthetic seismograms in the well 7120/12-5 at five different fluid saturations.

6.1.2 Intercept and Gradient

The top and bottom AVO response for the reservoir (Stø Formation) is determined by using the reflectivity and intercept-gradient analyses. The two-term Aki-Richards equation with robust correction is applied during the reflectivity and intercept-gradient analyses. The AVO class, intercept and gradient with different pore fluid of the two wells 7120/12-3 and 7120/12-5 are shown in the Table 6.3.

In the well 7120/12-3, top of the reservoir (Stø Formation) shows the AVO class IV with negative intercept while the gradient is positive. The intercept for in-situ gas to 100% water saturation decreases from -0.17044 to -0.13117 while the gradient decreases from 0.31022 to 0.2343. However, the bottom of the reservoir has a positive intercept and a negative gradient. The intercept for 100% gas to 100% water saturated case decreases from 0.06024 to 0.04661 while the gradient also decreases from -0.10616 to -0.08478 (Fig. 6.4)

In the well 7120/12-5, top of the reservoir (Stø Formation) shows AVO class IV with intercept for in-situ water to 100% gas increases from -0.11826 to -0.15664 while gradient increases from 0.13367 to 0.15482. However, the bottom of the reservoir, the intercept for 100% water to 100% gas slightly increases from 0.0366 to 0.03936 while the gradient decreases from -0.05052 to -0.05553 (Fig. 6.5).

Table 6.3: AVO class, Intercept (A) and Gradient (B) of top and bottom of reservoir (Stø Formation) in the wells 7120/12-3 and 7120/12-5 at different fluid saturations.

Wells	Fluid	Top of reservoir			Bottom of reservoir		
		Class	Intercept (A)	Gradient (B)	Class	Intercept (A)	Gradient (B)
7120/12-3	100% Gas	IV	-0.17044	0.31022	I	0.06024	-0.10616
	50% Gas	IV	-0.15639	0.28121	I	0.05326	-0.09482
	100% Water	IV	-0.13117	0.23437	I	0.04661	-0.08478
7120/12-5	100% Water	IV	-0.11826	0.13367	I	0.03660	-0.05052
	50% Gas	IV	-0.14806	0.14097	I	0.03769	-0.05496
	100% Gas	IV	-0.15664	0.15482	I	0.03936	-0.05553

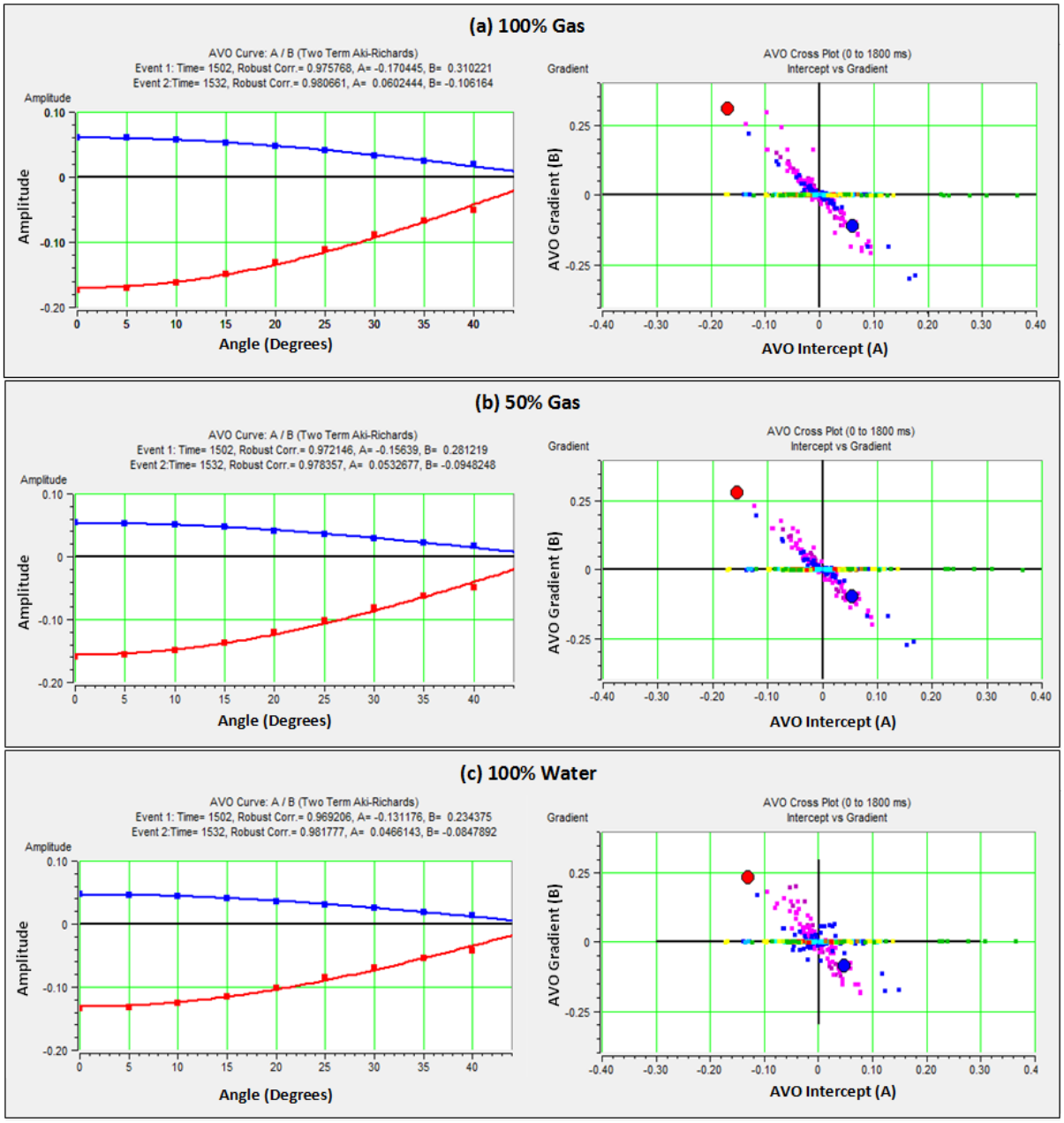

Figure 6.4: Response of angle dependent reflectivity with intercept-gradient plot in the well 7120/12-3 for three different fluid saturations (a) 100% gas (b) 50% gas (c) 100% water

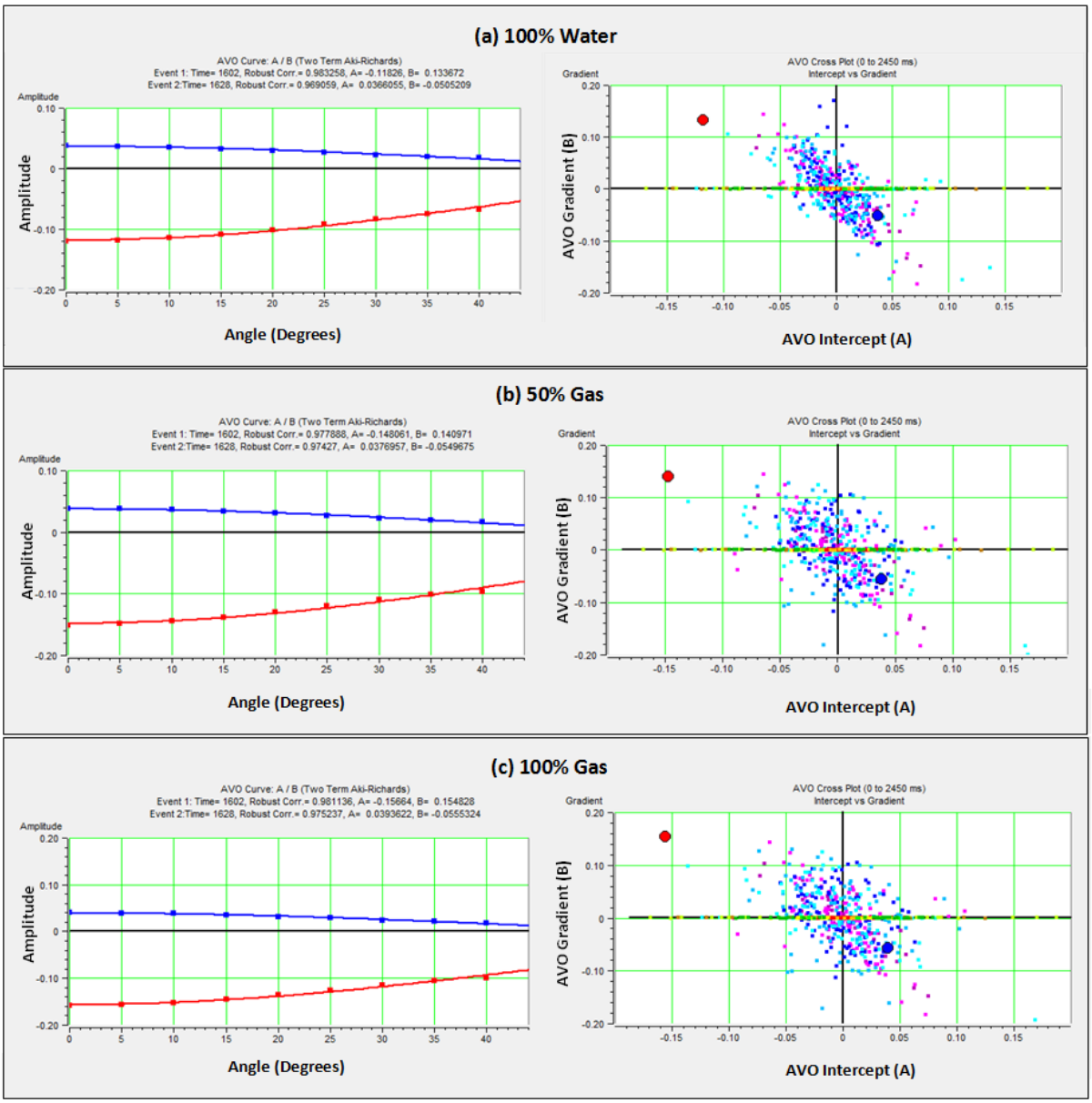

Figure 6.5: Response of angle dependent reflectivity with intercept-gradient plot in the well 7120/12-5 for three different fluid saturations (a) 100% water (b) 50% gas (c) 100% gas

6.2 Discussion

In AVO modeling, the effect related to nature of fluid present in the reservoir has been demonstrated. As expected the AVO response changes with the type of fluid in the reservoir. Moreover, it results in changing the rocks physical properties such as density, Vp, Vs and Poisson's ratio. The Stø Formation in two wells (7120/12-3 and 7120/12-5) has been analyzed by using five different gas saturation scenarios. The AVO response of reservoirs physical properties of Stø Formation is almost same for both the wells.

$$V_p = \sqrt{\frac{K + \frac{4}{3}\mu}{\rho}} \dots\dots\dots\dots\dots\dots (6.1)$$

$$V_s = \sqrt{\frac{\mu}{\rho}} \dots\dots\dots\dots\dots\dots (6.2)$$

Where K represents bulk modulus, μ represents shear modulus and ρ represents density. Equation 6.1 shows that Vp in a rock is dependent upon its bulk modulus, shear modulus and density. However, the bulk modulus and density of the rock is dependent on the nature of pore fluid. Water has a much higher density (1 g/cc) than gas. Similarly bulk modulus shows the same behavior as it decreases with increase in gas saturation. It is due to the fact that bulk modulus is the measure of incompressibility of rock. Since, gas is more compressible as compared to liquids so gas exhibits low bulk modulus. Therefore, the introduction of 10%gas into 100% water saturated rock shows a decrease in its Vp from 4433 m/s to 4258 m/s in the well 7120/12-3 (Fig. 6.6).

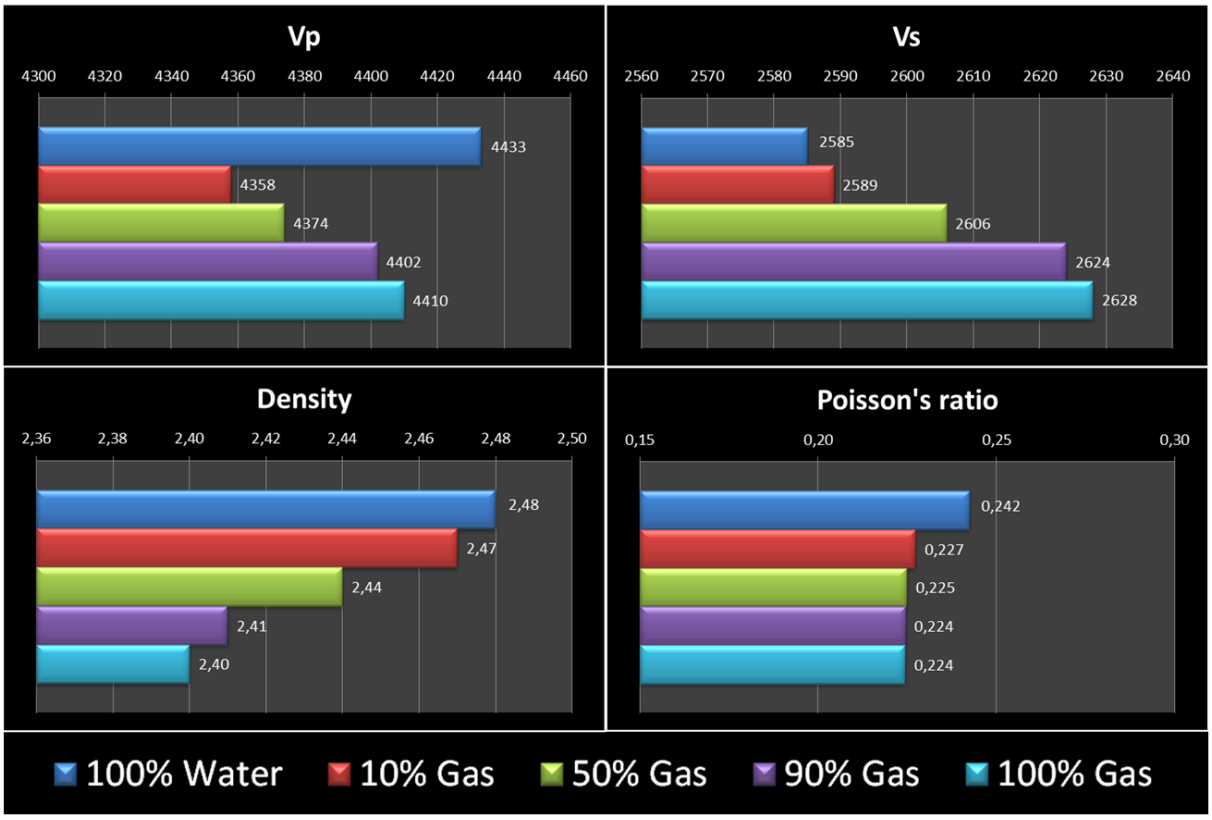

Figure 6.6: Changes in rock properties in the well 7120/12-3.

For higher gas saturations such as 50, 90 and 100%, increase in Vp is observed. The Vp increases notably from 4358 m/s at 10% gas saturation to 4410m/s at 100% gas saturation. This increase in Vp is due to decrease in bulk modulus and density as the gas saturation increases. However the rate of decrease in density is more than the decrease in bulk modulus. This results in slightly higher Vp values for increasing gas saturation.

Equation 6.2 shows that Vs depends on shear modulus and density of the rocks. Vs is independent of the type of fluid present in the reservoir as shear modulus is zero for the liquids. However, the density does affect the Vs. In case of 100% water saturation, density is 2.48 g/cc in the well 7120/12-3. But a significant decrease in density is observed for a gas saturation of 100%. It results in slightly higher Vs in the reservoir by increasing gas content. It rises from 2589 m/s at 10% gas saturation to 2628 m/s at 100% gas saturation (Fig. 6.6).

The reservoir (Stø Formation) in the wells 7120/12-3 and 7120/12-5 expresses similar trend in Vp, density and Vs. Therefore, gas replacement for reservoir in well 7120/12-3 (Fig. 6.6) shows similar results as the reservoir in the well 7120/12-5 (Fig. 6.7).

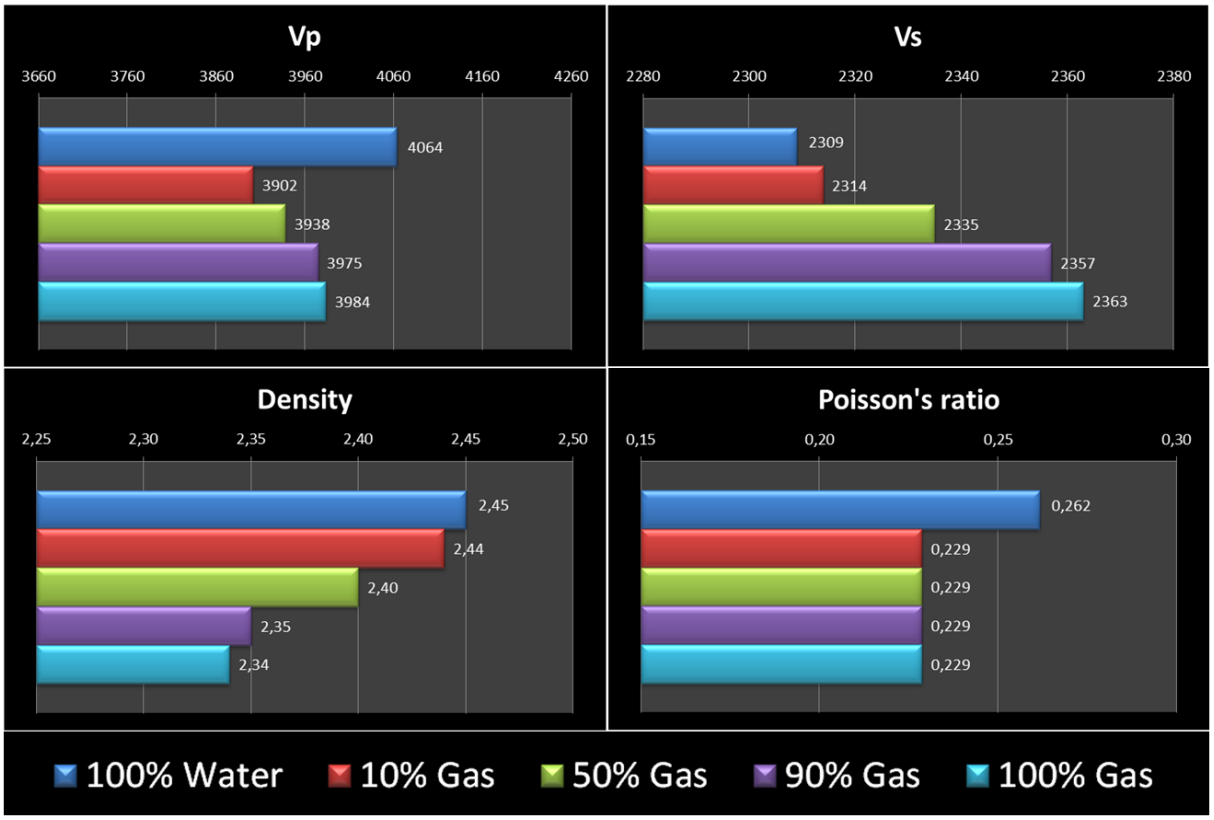

Figure 6.7: Changes in rock properties in the well 7120/12-5.

The AVO response for the sand reservoir in well 7120/12-3 can be classified as class IV based on Rutherford and William (1989) gas sand classification. In the Figure 6.4, three cases are shown i.e. 100% gas, 50% gas and 100% water saturation. The density and Vp in rocks decrease with increase in gas saturation. Therefore, AI contrast exists between cap-rock and reservoir rock. In this case it is negative because presence of 100% gas in reservoir results in higher AI in cap rock than reservoir. It is shown by higher AI values at zero-offset for 100% gas saturated reservoir. However, increase in water saturation results in decrease in AI contrast because of higher density of water and higher Vp for water saturated reservoir. So a decrease in zero offset reflection coefficient can be seen from -0.17044 at 100% gas to -0.13117 at 100% water saturation. Figure 6.4 also shows that AVO response from angles 0 to 45 degrees follows nearly the same trend for different gas saturations. The AVO response can also be presented in terms of AVO intercept versus Gradient as shown in the Figure 6.4. These crossplots also indicate an AVO class IV in the well 7120/12-3. Similar case can be observed with the reservoir in the well 7120/12-5 (Fig. 6.5) which also shows an AVO class IV and its behavior is similar as in case of reservoir in the well 7120/12-3.

Chapter 7

Summary and Conclusions

7.1 Summary and Conclusions

The Barents Sea is an active exploration area for the past 30 years. So far ninty six exploration wells have been drilled in the Western Barents Sea where most of the wells are located in the Hammerfest Basin. The Alka discovery is located in the southern part of the Hammerfest Basin, SW Barents Sea. The study area contains 5 exploration wells (7120/12-1, 7120/12-2, 7120/12-3, 7120/12-4 and 7120/5). The gas/condensate was discovered in 1981 with reservoir intervals occur in Stø Formation and Snadd Formation in the well 7120/12-2. Later in 1983, another gas discovery was made in the upper part of the Stø Formation in the well 7120/12-3. The other three wells (7120/12-1, 7120/12-4 and 7120/12-5) were dry. The main source rock in the study area is Hekkingen Formation of the Upper Jurassic age which also acts as a cap rock along with Fuglen Formation of the Upper Jurassic age. The reservoir quality of five possible reservoir horizons (Stø, Nordmela, Tubåen, Fruholmen and Snadd) is investigated by integrated techniques of petrophysical analyses, rock physics diagnostics and AVO modeling.

Petrophysical analyses are the initial step to calculate and to investigate reservoir rock properties such as shale volume, net-to-gross, porosity and saturation. The petrophysical analyses are considered to calculated reservoir properties of the whole Kapp Toscana Group using the five studied wells. Emphasis has been given to the Stø Formation as it has better reservoir quality than the other formations of Kapp Toscana Group. After petrophysical analysis, three main Rock physics templates including the porosity versus Vp, AI versus Vp/Vs and Lambda-Rho versus Mu-Rho have been used to investigate lithology, cement distribution and fluid saturation. In the end AVO modeling is performed to check the rock properties in response of changing fluid saturation.

Bases on the integrated techniques of petrophysical analyses, rock physics diagnostics and AVO modeling, the following conclusions have been deduced:

- The shale volume in Stø Formation is greater in the southern wells (7120/12-1 and 7120/12-2) which decrease towards the northern wells (7120/12-3 and 7120/12-5).

- The net-to-gross of Stø Formation is greater in the northern wells (7120/12-3 and 7120/12-5) than the southern wells (7120/12-1 and 7120/12-2). Stø Formation has higher net-to-gross ratio compared to the other formations of Kapp Toscana Group. Nordmela, Tubåen and Fruholmen Formations have intermediate value of net-to-gross showing moderate reservoir quality while Snadd Formation has the lowest value of net-to-gross depicting low quality reservoir .

- The amount of shale volume is higher in Fruholmen and Snadd Formations in the well 7120/12-5. Moreover, these formations are poorly sorted and have low porosity due to cementation of finer materials in the pore spaces.

- On the basis of neutron-density cross-over and high value of deep resistivity log, gas saturated zones have been identified in the Stø Formation in two wells (7120/12-2 and 7120/12-3).

- Cement distribution varies within the Stø Formation. Velocity is lower in the gas saturated zone in the wells 7120/12-2 and 7120/12-3. Gas saturated zone in the well 7120/12-3 is in the upper part having less cement and low velocity than its underlying part which has

higher velocity and is more cemented. Stø Formation in the well 7120/12-5 is poorly sorted and is more cemented.

- Cross plot of AI versus Vp/Vs fails to explain the gas saturated zone in wells 7120/12-2 and 7120/12-3 because it occurs on the water saturated line. The calculated Vs from different empirical relation could not help to explain this RPT.

- Cross plot of Lambda-Rho versus Mu-Rho shows that the gas saturated zones identified earlier in the wells 7120/12-2 and 7120/12-3 have low Lambda-Rho and Mu-Rho as compared to the fully water saturated part in the Stø Formation which has higher Lambda-Rho and Mu-Rho.

- AVO modeling shows that changes in rock properties are more prominent by introducing 10% gas saturation than at 50%, 90% and 100% in both the investigated wells 7120/12-3 and 7120/12-5. The change in synthetic seismogram is also more pronounced with 10% increase in gas saturation than at other fluid replacements.

- Top of reservoir (Stø Formation) shows an AVO Class IV in both wells 7120/12-3 and 7120/12-5.

References

- ADAM, L., BATZLE, M. & BREVIK, I. 2006. Gassmann's fluid substitution and shear modulus variability in carbonates at laboratory seismic and ultrasonic frequencies. Geophysics, 71, F173-F183.

- ADEPELUMI, A. A., ALAO, O. A. & KUTEMI, T. F. 2011. Reservoir characterization and evaluation of depositional trend of the Gombe sandstone, southern. Journal of Petroleum and Gas Engineering Vol, 2**,** 118-131.

- AKI, K. & RICHARDS, P. G. 1980. Quantitative seismology, Freeman San Francisco.

- ASQUITH, G. B., KRYGOWSKI, D. & GIBSON, C. R. 2004. Basic well log analysis, American Association of Petroleum Geologists.

- AVSETH, P. 2010. Exploration rock physics-The link between geological processes and geophysical observables. In: Bjørlykke, K. 2010. Petroleum Geoscience: from Sedimentary Environments to Rock Physics, Berlin, Heidelberg, Springer-Verlag Berlin Heidelberg, 403–426.

- AVSETH, P., JØRSTAD, A., VAN WIJNGAARDEN, A.-J. & MAVKO, G. 2009. Rock physics estimation of cement volume, sorting, and net-to-gross in North Sea sandstones. The Leading Edge, 28**,** 98-108.

- AVSETH, P., MUKERJI, T. & MAVKO, G. 2005. Quantitative seismic interpretation: Applying rock physics tools to reduce interpretation risk: Cambridge.

- AVSETH, P., MUKERJI, T., MAVKO, G. & DVORKIN, J. 2010. Rock-physics diagnostics of depositional texture, diagenetic alterations, and reservoir heterogeneity in high-porosity siliciclastic sediments and rocks—A review of selected models and suggested work flows. Geophysics, 75**,** 75A31-75A47.

- BJØRLYKKE, K. 2010. Production Geology. In: Bjørlykke, K. 2010, Petroleum Geoscience: from Sedimentary Environments to Rock Physics, Berlin, Heidelberg, Springer-Verlag Berlin Heidelberg, 445-458.

- BJØRLYKKE, K. 2010. Well Logs: A Brief Introduction. In: Bjørlykke, K. 2010, Petroleum Geoscience: from Sedimentary Environments to Rock Physics, Berlin, Heidelberg, Springer-Verlag Berlin Heidelberg, 361-373.

- CASTAGNA, J. P. 1993. Offset-dependent reflectivity: Theory and practice of AVO analysis, SEG Books.

- CASTAGNA, J. P., BATZLE, M. L. & EASTWOOD, R. L. 1985. Relationships between compressional-wave and shear-wave velocities in clastic silicate rocks. Geophysics, 50**,** 571-581.

- CASTAGNA, J. P., SWAN, H. W. & FOSTER, D. J. 1998. Framework for AVO gradient and intercept interpretation. Geophysics, 63, 948-956.

- CHI, X.-G. & HAN, D.-H. 2009. Lithology and fluid differentiation using a rock physics template. The Leading Edge, 28**,** 60-65.

- DALLAND, A., WORSLEY, D. & OFSTAD, K. 1988. A Lithostratigraphic Scheme for the Mesozoic and Cenozoic and Succession Offshore Mid-and Northern Norway, Oljedirektoratet.

- DORE, A. 1995. Barents Sea geology, petroleum resources and commercial potential. Arctic**,** 207-221.

- DVORKIN, J. & NUR, A. 1996. Elasticity of high-porosity sandstones: Theory for two North Sea data sets. Geophysics, 61**,** 1363-1370.

- FALEIDE J. F., BJØRLYKKE K. AND GABRIELSEN R. H. 2010. In: Bjørlykke, K. 2010. Geology of the Norwegian Continental Shelf. In Bjorlykke K. 2010. Petroleum Geoscience: from Sedimentary Environments to Rock Physics, Berlin, Heidelberg, Springer-Verlag Berlin Heidelberg, 467–499.

- FALEIDE, J. I., GUDLAUGSSON, S. T. & JACQUART, G. 1984. Evolution of the western Barents Sea. Marine and Petroleum Geology, 1**,** 123-150.

- FALEIDE, J. I., TSIKALAS, F., BREIVIK, A. J., MJELDE, R., RITZMANN, O., ENGEN, O., WILSON, J. & ELDHOLM, O. 2008. Structure and evolution of the continental margin off Norway and the Barents Sea. Episodes, 31**,** 82.

- FALEIDE, J. I., VÅGNES, E. & GUDLAUGSSON, S. T. 1993. Late Mesozoic-Cenozoic evolution of the south-western Barents Sea in a regional rift-shear tectonic setting. Marine and Petroleum Geology, 10**,** 186-214.

- FAWAD, M., MONDOL, N. H., JAHREN, J. & BJØRLYKKE, K. 2011. Mechanical compaction and ultrasonic velocity of sands with different texture and mineralogical composition. Geophysical Prospecting, 59**,** 697-720.

- GABRIELSEN, R. 1984. Long-lived fault zones and their influence on the tectonic development of the southwestern Barents Sea. Journal of the Geological Society, 141**,** 651-662.

- GARDNER, G., GARDNER, L. & GREGORY, A. 1974. Formation velocity and density-the diagnostic basics for stratigraphic traps. Geophysics, 39, 770-780.

- GELIUS, L. J. & JOHANSEN, T., A. 2010. Petroleum Geophysics, Unigeo.

- GLØRSTAD-CLARK, E., FALEIDE, J. I., LUNDSCHIEN, B. A. & NYSTUEN, J. P. 2010. Triassic seismic sequence stratigraphy and paleogeography of the western Barents Sea area. Marine and Petroleum Geology, 27**,** 1448-1475.

- GOODWAY, B. 2001. AVO and Lamé constants for rock parameterization and fluid detection. Recorder, 26, 39-60.

- HAMPSON-RUSSELL SOFTWARE SERVICES LTD. 2004. AVO Theory.

- HAN, D.-H. & BATZLE, M. L. 2004. Gassmann's equation and fluid-saturation effects on seismic velocities. Geophysics, 69, 398-405.

- HAN, D.-H., NUR, A. & MORGAN, D. 1986. Effects of porosity and clay content on wave velocities in sandstones. Geophysics, 51**,** 2093-2107.

- HENRIKSEN, E., RYSETH, A., LARSSEN, G., HEIDE, T., RØNNING, K., SOLLID, K. & STOUPAKOVA, A. 2011. Tectonostratigraphy of the greater Barents Sea: implications for petroleum systems. Geological Society, London, Memoirs, 35**,** 163-195.

- LARSEN, R., FJAERAN, T. & SKARPNES, O. 1993. Hydrocarbon potential of the Norwegian Barents Sea based on recent well results. Arctic geology and petroleum potential**,** 321-331.

- LARSSEN, G., ELVEBAKK, G., HENRIKSEN, L. B., KRISTENSEN, S., NILSSON, I., SAMUELSBERG, T., SVÅNÅ, T., STEMMERIK, L. & WORSLEY, D. 2002. Upper Palaeozoic lithostratigraphy of the Southern Norwegian Barents Sea. Norwegian Petroleum Directorate Bulletin, 9**,** 76.

- MAGOON, L. B. & DOW, W. G. 1994. The petroleum system, American Association of Petroleum Geologists.

- MAVKO G., MUKERJI T. AND DVORKIN J. (2009). The rock physics handbook: Tools for seismic analysis of porous media. Cambridge University Press, New York.

- MONDOL N. H. 2010. Seismic exploration. In: Bjørlykke, K. 2010. Petroleum Geoscience: from Sedimentary Environments to Rock Physics, Berlin, Heidelberg, Springer-Verlag Berlin Heidelberg, 375 – 402.

- MOORE, W. R., MA, Y. Z., URDEA, J. & BRATTON, T. 2011. Uncertainty analysis in well-log and petrophysical interpretations.

- MØRK, A., EMBRY, A. F. & WEITSCHAT, W. 1989. Triassic transgressive-regressive cycles in the Sverdrup Basin, Svalbard and the Barents Shelf. Correlation in hydrocarbon exploration. Springer.

- NORWEGIAN PETROLEUM DIRECTORATE (NPD) Factpages and Factmaps (www.npd.no). Last accessed: 20th May, 2013.

- OHM, S. E., KARLSEN, D. A. & AUSTIN, T. 2008. Geochemically driven exploration models in uplifted areas: Examples from the Norwegian Barents Sea. AAPG bulletin, 92**,** 1191-1223.

- OSTANIN, I., ANKA, Z., DI PRIMIO, R. & BERNAL, A. 2012. Identification of a large Upper Cretaceous polygonal fault network in the Hammerfest basin: Implications on the reactivation of regional faulting and gas leakage dynamics, SW Barents Sea. Marine Geology.

- Øvrebø O. & Talleraaes E. 1977. The structural geology of the Troms area. Geo journal, 1, 47-54.

- RAYMER, L., HUNT, E. & GARDNER, J. 1980. An improved sonic transit time-to-porosity transform. SPWLA Trans., 21st Ann. Log. Symp., Paper P.

- RIDER, M. & KENNEDY, M. 2011. The Geological Interpretation of Well Logs. Rider-French Consulting Limited.

- RUTHERFORD, S. R. & WILLIAMS, R. H. 1989. Amplitude-versus-offset variations in gas sands. Geophysics, 54**,** 680-688.

- SELDAL, J. Lower Cretaceous: the next target for oil exploration in the Barents Sea? Geological Society, London, Petroleum Geology Conference series, 2005. Geological Society of London, 231-240.

- SELNES A., DVORKIN J., CARR M., HOFFMANN J. AND HUBERT L. 2004. Rock physics diagnostics, effective medium models and analysis of the Stø Formation, Hammerfest Basin, Norway. EAGE 66th Conference & Exhibition-Paris, France.

- SHUEY, R. 1985. A simplification of the Zoeppritz equations. Geophysics, 50**,** 609-614.

- SMITH, G. & GIDLOW, P. 1987. Weighted Stacking for Rock Property Estimation and Detection of GAS*. Geophysical Prospecting, 35**,** 993-1014.

- STEWART, D., BERGE, K. & BOWLIN, B. 1995. Exploration trends in the southern Barents Sea. Norwegian Petroleum Society Special Publications, 4**,** 253-276.

- SUND, T., SKARPNES, O., JENSEN, L. N. & LARSEN, R. 1986. Tectonic development and hydrocarbon potential offshore Troms, northern Norway.

- WORSLEY, D. 2008. The post-Caledonian development of Svalbard and the western Barents Sea. Polar Research, 27**,** 298-317.

- WYLLIE, M. R. J., GREGORY, A. R. & GARDNER, L. W. 1956. Elastic wave velocities in heterogeneous and porous media. Geophysics, 21**,** 41-70.

- YOUNG, K. T. & TATHAM, R. H. Lambda-mu-rho inversion as a fluid and lithology discriminator in the Columbus Basin, offshore Trinidad. 2007 SEG Annual Meeting, 2007.